HD-KIP-01-03

Search for Odderon Induced Contributions to Exclusive π^0 Photoproduction at HERA

This diploma thesis has been carried out by Tobias Golling at the
University of Heidelberg
Kirchhoff-Institut für Physik
Faculty of Physics and Astronomy

Dedicated to Simone

Zusammenfassung

Gegenstand dieser Diplomarbeit ist das Odderon, das als der $C = P = -1$ Partner des Pomerons angesehen werden kann. Damit sind seine Kopplungen an ein Teilchen und dessen Antiteilchen verschieden, was in pp und $p\bar{p}$ Streuung sichtbar sein müßte.

In dieser Arbeit wird nach Beiträgen der Odderon-Photon-Fusion zur exklusiven Produktion des pseudoskalaren Mesons π^0 im Prozeß $ep \to e\pi^0 N^*$ in der Photoproduktionsregion gesucht. Die untersuchten Daten wurden mit dem Detektor H1 bei der Speicherringanlage HERA am DESY in Hamburg bei einer mittleren Photon-Proton Schwerpunktsenergie von 211 GeV und Photon-Virtualitäten von $Q^2 < 0.01$ GeV^2 im Jahr 1999 aufgezeichnet und ergaben eine integrierte Luminosität von 11.06 pb^{-1}. Das hochenergetische Pion wird über den Zerfall in zwei Photonen nachgewiesen. Desweiteren werden das in Vorwärtsrichtung gestreute Neutron aus dem Zerfall des angeregten Protons und das gestreute Elektron detektiert.

Ein Hinweis auf die Anwesenheit von Odderon-Beiträgen kann nicht gefunden werden. Als Ergebis kann ein oberes Limit für den Wirkungsquerschnitt des vorliegenden Prozesses bestimmt werden, das sich auf einem Konfidenz Niveau von 95% zu $\sigma(\gamma p \to \pi^0 N^*) < 74.3$ nb und auf einem Konfidenz Niveau von 99% zu $\sigma(\gamma p \to \pi^0 N^*) < 100$ nb ergibt.

Abstract

This diploma thesis is about the Odderon which is the $C = P = -1$ partner of the Pomeron. Thus, its couplings to a particle and its antiparticle are not equal, which in principle should be measurable in pp and $p\bar{p}$ scattering.

A search for contributions of Odderon-photon-fusion to the exclusive production of the pseudoscalar π^0 in the process $ep \to e\pi^0 N^*$ in the photoproduction regime is subject of this thesis. The investigated data with an integrated luminosity of 11.06 pb^{-1} were recorded in 1999 with the H1 detector at the storage ring HERA at DESY in Hamburg. The measurement was carried out at an average photon-proton centre-of-mass energy of 211 GeV and for photon virtualities of $Q^2 < 0.01$ GeV^2. The high-energetic π^0 is reconstructed through its decay into two photons. Furthermore, the measurement proceeds via the detection of the leading neutron from the N^* decay and the detection of the scattered electron.

No indication for the presence of Odderon contributions can be found. As a result an upper limit of the cross section is derived to $\sigma(\gamma p \to \pi^0 N^*) < 74.3$ nb with a confidence level of 95% and $\sigma(\gamma p \to \pi^0 N^*) < 100$ nb with a confidence level of 99%.

Contents

List of Tables

List of Figures

Introduction

Since its very beginning, physics has pondered the question of what the fundamental building blocks of matter might be. For a long time it was a question of belief whether for example matter is made up of indivisible particles, atoms, as the Greek philosopher Democrit postulated, or if it is continuous in structure which was Aristotle's view. Nowadays, measurements can be taken to verify or falsify a theoretical model. With the discovery of the electron more than 100 years ago the image of the structure of matter has developed crucially. A considerable contribution to this insight has been won from experiments with colliding particles. A "zoo" of particles has been found and at the end of the seventies enough experimental results were accumulated in this new area of physics to construct a description of the physical world, which is called the Standard Model of particle physics. According to this model there are two types of particles, fermions and gauge bosons. The former, which themselves can be divided into two groups - leptons and quarks, are the elementary and apparently pointlike particles of solid matter, whereas the gauge bosons are the carriers of the four basic forces: the electromagnetic, the weak, the strong and the gravitational force which are mediated by the photons, the $W^{\pm}$ and Z bosons, the gluons and the gravitons, respectively.

This diploma thesis deals with processes which are induced by the fusion of a photon and the Odderon. In terms of QCD[1], the theory describing strong interactions, the latter can be modelled as a particle which consists of three gluons. Within the framework of the so-called vector meson dominance model a strong interacting character is assigned to the photon so that an interaction with gluons is possible via the strong coupling. At the storage ring HERA at DESY in Hamburg, protons and electrons collide head-on where the electrons serve as a source of virtual photons. The Odderon-photon-fusion produces a high-energetic π^0 and the incoming proton is excited (quasi-) diffractively to an N^*. All particles in the final state of the studied reaction $ep \to e\pi^0 N^*$ are detected by the components of the H1 detector: the scattered electron under small scattering angles, the neutron from the decayed N^* and the two decay photons from the pion.

The content of the present analysis is divided into six parts: The first chapter gives an insight in the theoretical framework of the concepts required. It starts with the kinematics of the electron-proton scattering at HERA, Regge phenomenology is introduced and at the end some properties of the pion decay are summarized. The second chapter presents the storage ring HERA and the H1 detector with emphasis on the components used. A description of the VLQ calorimeter follows. The fourth chapter is about the simulation of the studied reaction and possible background processes. The Monte-Carlo particle generators used and the simulation of the H1 detector are illustrated. Finally, the steps of the analysis are presented

[1] Quantum Chromo Dynamics

including the selection criteria, the description of the efficiencies and the acceptances. As a result an upper limit on the cross section of the process under study is derived, and a conclusion is given in the last chapter.

Chapter 1

Theoretical Framework

1.1 Electron-Proton Scattering at HERA

In HERA, electrons at an energy of 27.56 GeV collide head-on with protons at an energy of 920 GeV in the centre of the H1 detector. In the most general case, the lepton-nucleon interaction proceeds via the exchange of a virtual vector boson. Figure 1.1 shows a "Feynman-like" diagram of the electron-proton scattering process:

$$ep \to \ell X, \tag{1.1}$$

where ℓ is the scattered lepton in the final state according to conservation of lepton number, while the proton may fragment into a hadronic final state X. In principle there are four different gauge vector bosons responsible for the interaction. In the case of the exchange of either a W^- or a W^+, ℓ represents a neutrino or an antineutrino, respectively, and one speaks of *charged current* events. In contrast, when a Z^0 boson or a virtual photon γ^*[1] is exchanged, the interaction is called a *neutral current* event.

The subject of this analysis focuses on the photon exchange only with a scattered electron in the final state. Contributions from the W- and Z^0-bosons can be neglected for the considered momentum transfers Q^2 (see equation (1.3)).

1.1.1 Kinematics of Electron-Proton Scattering

Lorentz invariant quantities are used to describe the kinematics of the *ep* scattering reaction. According to the law of energy and momentum conservation, the four-momenta obey the equation:

$$k + P = k' + X, \tag{1.2}$$

where k and k' denote the four-momenta of the initial and final state electron and P and X the four-momenta of the incoming proton and the outgoing hadronic system, respectively. Using these momenta, Lorentz invariant quantities for the *ep* scattering process can be defined:

[1] The asterisk $*$ denotes that it is a virtual photon (a photon which is off-shell).

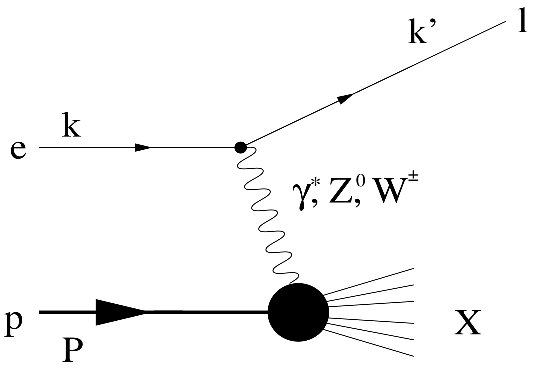

Figure 1.1: Schematic view of the electron-proton scattering.

- **The four-momentum transfer squared** at the electron-photon-vertex:

$$Q^2 = -q^2 = -(k - k')^2 > 0 \text{ GeV}^2, \tag{1.3}$$

  This quantity, also called *virtuality of the photon*, indicates the violation of the mass shell relation for real photons $q^2 = m_\gamma^2 = 0$. Q^2 is also a measure for the resolving power of the photon:

$$\Delta \sim \frac{\hbar c}{\sqrt{Q^2}} = \frac{0.197\text{GeV fm}}{\sqrt{Q^2}}, \tag{1.4}$$

  with Δ denoting the spatial resolution of the proton's structure.

- The dimensionless **Bjorken scaling variable** x is defined by:

$$x = \frac{Q^2}{2qP}. \tag{1.5}$$

  The physical meaning of this variable is most easily realized by going to the so-called infinite momentum frame in which masses and transverse momenta can be neglected compared to the absolute momentum of the proton. In this frame the variable x is the fraction of the proton momentum carried by the massless parton which absorbs the exchanged photon.

- The dimensionless **inelasticity**:

$$y = \frac{qP}{kP}. \tag{1.6}$$

  In the rest frame of the proton, y denotes the fractional energy transfer from the electron on the proton.

Both x and y are confined to the range from 0 to 1.

- **The squared centre of mass energy** of the electron proton system:

$$s = (k + P)^2. \tag{1.7}$$

At HERA $\sqrt{s}$ equals 318.5 GeV.

- **The squared four-momentum transfer** at the proton-vertex:

$$t = (P - X)^2. \tag{1.8}$$

Along with u, s and t comprise the so-called "Mandelstam-variables".

- **The squared invariant mass** of the hadronic final state which is equivalent to the squared centre of mass energy of the photon proton system:

$$W^2 = s_{\gamma p} = X^2 = (q + P)^2 = q^2 + 2qP + M^2, \tag{1.9}$$

with M being the mass of the proton.

The kinematical variables s, x, y and Q^2 are not independent of each other but related by:

$$Q^2 = xys. \tag{1.10}$$

Thus, for a given centre of mass energy, there are only two kinematical degrees of freedom. Two conveniently chosen independent variables, already completely determining the process, are the energy of the outgoing electron E' and the scattering angle θ. Their dependence on other variables is illustrated (figure 1.2) in the so-called kinematical plane, spanned by x and Q^2. In this picture, regions with constant y are given by straight lines parallel to the diagonal ($y = 1$) which limits the kinematically accessible domain.

- For the description of the final state another kinematical quantity often used is the **rapidity** of a particle which is defined by:

$$\begin{aligned} Y &= \frac{1}{2}\ln\left(\frac{E+p_z}{E-p_z}\right) && (1.11)\\ &= \tanh^{-1}\left(\frac{p_z}{E}\right), && (1.12)\end{aligned}$$

where z defines the direction of the protons. A characteristic of Y is the invariance of the shape of the rapidity distribution under longitudinal Lorentz transformations. For example, under a boost in z-direction with velocity β, Y transforms as $Y \rightarrow Y - tanh^{-1}(\beta)$.

For $p \gg m$, the rapidity Y can be approximated by the **pseudo-rapidity**:

$$\eta = -\ln\tan\frac{\theta}{2}, \tag{1.13}$$

with $\theta = arccos(p_z/p)$. The pseudo-rapidity varies from $\eta \approx -\infty$ for $\theta \approx 180°$ to $\eta \approx \infty$ for $\theta \approx 0°$ where $\eta \approx 0$ represents particles with $\theta \approx 90°$.

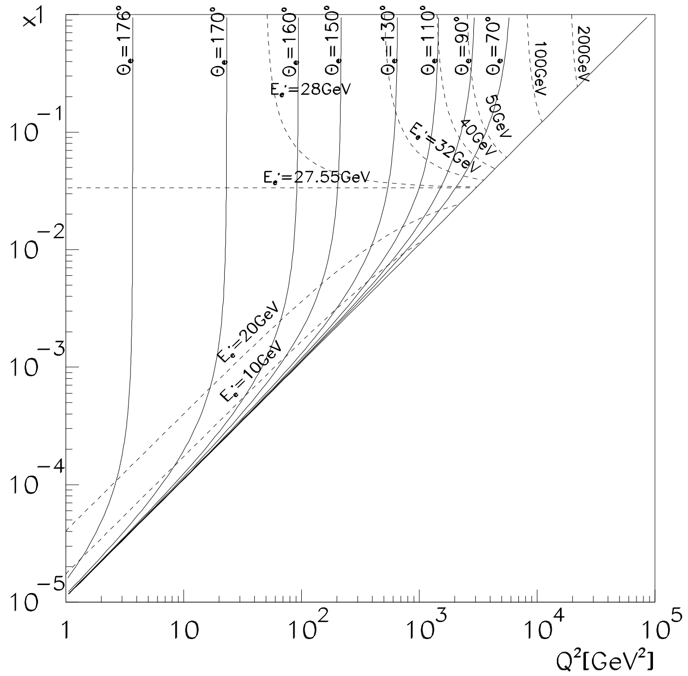

Figure 1.2: The figure depicts lines of constant energies (dashed line) and scattering angles (solid line) of the outgoing electron in the kinematical plane. The horizontal dashed line represents the kinematic peak electrons arising from the elastic scattering of an electron with a parton of the proton of the same energy. The accessible part of the plane is limited by the diagonal $y = 1$.

1.1.2 Kinematical Regions in Electron-Proton Scattering

Figure 1.3 gives an overview over the kinematical regions at HERA. They can be characterized by the two variables p_t, the transverse momentum, and Q^2, the four-momentum transfer squared. The transverse momentum separates the reactions in so-called hard processes for $p_t \geq 1$ GeV$/c$ and soft processes for $p_t \leq 1$ GeV$/c$. Another partition is given by Q^2: The region where Q^2 is larger than 1 GeV^2 represents DIS (**D**eep **I**nelastic **S**cattering), whereas the region covered by $Q^2 \ll 1$ GeV^2 is called photoproduction. In this analysis the photoproduction regime is given by:

$$y_{min} = 0.3 \leq y \leq 0.7 = y_{max} \quad \text{and} \quad 0 < Q^2 < 0.01 \text{ GeV}^2. \tag{1.14}$$

In the collinear approximation, where the photon is emitted parallel to the electron,

$$y = 1 - E'/E \tag{1.15}$$

(see the dashed lines for $E' = 10$ and 20 GeV in figure 1.2).

Deep Inelastic Scattering (DIS)

For $Q^2 \geq 1$ GeV^2 it is possible to resolve (equation (1.4)) the structure of the proton which consists of a system of charged and neutral partons. The charged constituents can be

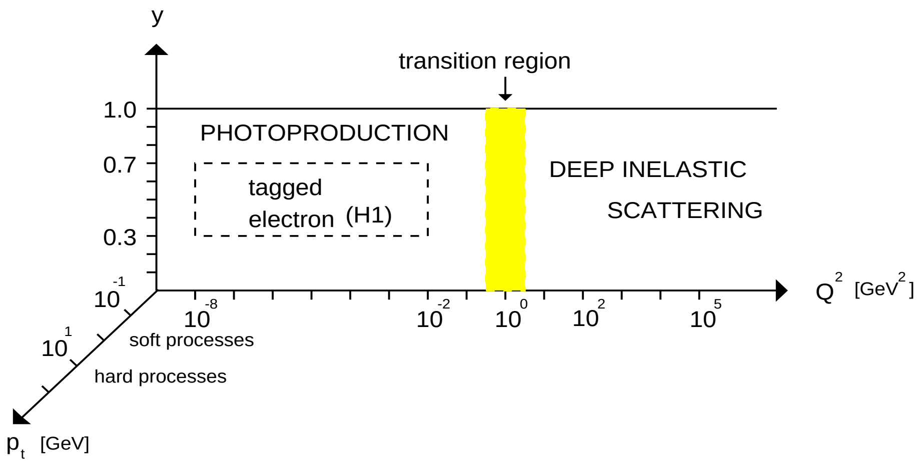

Figure 1.3: *Kinematic partition of the ep-scattering in photoproduction and deep inelastic scattering by the variable* Q^2 *as well as the partition in hard and soft processes by the variable* p_t*. The photoproduction region with an electron tagged (see section 2.8) can be defined at HERA by the variables* y *and* Q^2*:* $y_{min} = 0.3 \leq y \leq 0.7 = y_{max}$ *and* $0 \lesssim Q^2 < 0.01 GeV^2$*, illustrated by the dashed rectangle.*

identified by the *quarks* and the neutral by the *gluons* (the exchange bosons of the strong interaction). In the parton model, a structure function $F_2(x) = x\sum_q e_q^2\,(q(x) + \bar{q}(x))$ can be introduced by summing over all quark and antiquark densities $q(x)$ and $\bar{q}(x)$ weighted by their electric charges squared e_q^2. Measurements of the structure function at HERA can be found for example in [AHM95, AID95, BRU96].

For large momentum transfers it is very likely that the proton breaks up. But according to *confinement* of quarks, only colourless free particles are allowed to exist which leads to hadronisation.

For $Q^2 \geq 10000$ GeV^2 the exchange of the Z^0 boson starts to contribute significantly. For $Q^2 < 100$ GeV^2 only photon exchange needs to be considered. The double-differential *ep* cross section for DIS can be expressed in terms of the total cross section for virtual transverse (T) and longitudinal (L) photons, chosen in the Hand convention [HAN63]:

$$\frac{d^2\sigma(ep \to eX)}{dydQ^2} = f^T_{\gamma/e}(y,Q^2)\sigma_T(y,Q^2) + f^L_{\gamma/e}(y,Q^2)\sigma_L(y,Q^2), \tag{1.16}$$

with the fluxes

$$f^T_{\gamma/e}(y,Q^2) = \frac{\alpha}{2\pi}\left(\frac{1+(1-y)^2}{y}\frac{1}{Q^2} - \frac{2m_e^2 y}{Q^4}\right), \tag{1.17}$$

$$f^L_{\gamma/e}(y,Q^2) = \frac{\alpha}{2\pi}\frac{2(1-y)}{y}\frac{1}{Q^2}. \tag{1.18}$$

Photoproduction

In the region covered by $Q^2 \ll 1$ GeV^2, due to its wavelength, the photon is not able to resolve the proton's inner structure, however the structure of the photon becomes apparent. To a first approximation, it is a point-like particle, although quantum mechanically, the photon may fluctuate into a (charged) fermion-antifermion pair: $\gamma \leftrightarrow f\bar{f}$. The hadronic

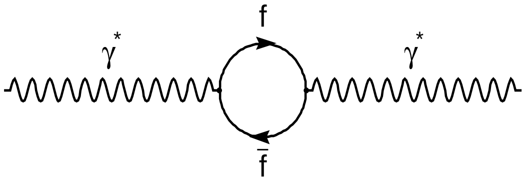

Figure 1.4: *A virtual photon fluctuates into a virtual fermion-antifermion loop which annihilates again to a photon.*

spectrum of fluctuations is split into a part of high-virtuality, pertubatively calculable, and a part of low-virtuality, not pertubatively calculable. The latter can be approximated by a sum over low-mass vector-meson states called the VMD (**V**ector **M**eson **D**ominance) ansatz.

In total, the photon wave function can be written as [FRI00]:

$$|\gamma\rangle = c_{bare}|\gamma_{bare}\rangle + \sum_{V=\rho^0,\omega,\phi,J/\Psi} c_V|V\rangle + \sum_{q=u,d,s,c,b} c_q|q\bar{q}\rangle + \sum_{\ell=e,\mu,\tau} c_\ell|\ell^+\ell^-\rangle, \tag{1.19}$$

neglecting the small contribution from the Υ. Whilst c_V can be determined from data, the other coefficients c_i depend on the scale the photon is probed, obeying unitarity.

Neglecting the last term of equation (1.19), the photon wave function can be subdivided into three main event classes [SCH93, SCH93a], see figure 1.5:

1. The direct process (first term in equation (1.19)), where a bare photon interacts with a parton from the proton.

2. The VMD process (second term in equation (1.19)), where the photon turns into a vector meson before the interaction. Therefore, all processes allowed in hadronic physics may occur (see figure 1.6).

3. The anomalous process (third term in equation (1.19)), where the photon fluctuates into a $q\bar{q}$ pair, and one of these interacts with a parton from the proton. These processes are calculable in perturbation theory due to the higher virtuality.

With all three event classes, conservation laws have to be fulfilled, in particular the fluctuations must have the same quantum numbers as the photon:

$$J^{PC} = 1^{--} \quad \text{and} \quad Q = B = S = 0. \tag{1.20}$$

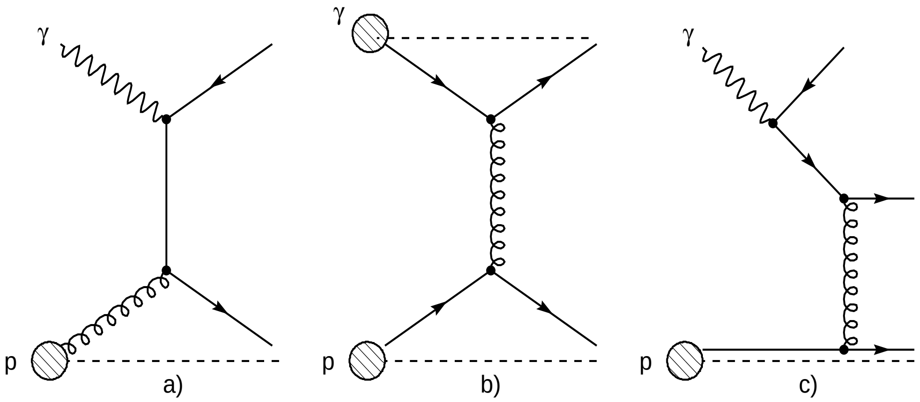

Figure 1.5: *The different classes of photoproduction: a) the direct process, b) the VMD process and c) the anomalous process (according to [SCH93]).*

According to the three different event classes, the total photoproduction cross section can be written as

$$\sigma_{tot}^{\gamma p} = \sigma_{VMD}^{\gamma p} + \sigma_{direct}^{\gamma p} + \sigma_{anomalous}^{\gamma p}. \tag{1.21}$$

Within Regge theory (see section 1.2.2) the behaviour of the total cross section can be parameterized by the form

$$\sigma_{tot}^{AB}(s) = X^{AB} s^{\epsilon} + Y^{AB} s^{-\eta} \tag{1.22}$$

for $A + B \to X$ and ϵ and η from equation (1.48). In the diagonal VMD model the vector meson-proton (Vp) cross sections are related to the photon-proton cross section by [HAN63]:

$$\sigma_{VMD}^{\gamma p}(s) = \sum_{V=\rho^0,\omega,\phi,J/\Psi} c_V^2 \sigma_{tot}^{Vp}(s). \tag{1.23}$$

The vector meson-proton cross sections can be parameterized, assuming the additive quark model, as [SCH93, SCH93a]

$$\begin{aligned} \sigma_{tot}^{\rho^0 p}(s) &\approx \sigma_{tot}^{\omega p}(s) \approx \frac{1}{2}\left(\sigma_{tot}^{\pi^+ p} + \sigma_{tot}^{\pi^- p}\right) \approx 13.63 s^{\epsilon} + 31.79 s^{-\eta} \quad [\mathrm{mb}] \\ \sigma_{tot}^{\phi p}(s) &\approx \sigma_{tot}^{K^+ p} + \sigma_{tot}^{K^- p} - \sigma_{tot}^{\pi^- p} \approx 10.01 s^{\epsilon} - 1.52 s^{-\eta} \quad [\mathrm{mb}] \\ \sigma_{tot}^{J/\Psi p}(s) &\approx \frac{m_\phi^2}{m_{J/\Psi}^2} \sigma_{tot}^{\phi p} \approx \frac{1}{10} \sigma_{tot}^{\phi p}(s), \end{aligned} \tag{1.24}$$

with s in GeV^2. The total VMD contribution to the photon-proton cross section can be obtained by adding all the vector meson contributions:

$$\sigma_{VMD}^{\gamma p}(s) \approx 53.4 s^{\epsilon} + 115 s^{-\eta} \quad [\mu\mathrm{b}]. \tag{1.25}$$

Comparing this cross section $\sigma_{VMD}^{\gamma p}(s)$ with the parameterization found for the γp cross section (see equation (1.50)) gives [DON92]:

$$\sigma_{tot}^{\gamma p}(s) = X^{\gamma p}s^{\epsilon} + Y^{\gamma p}s^{-\eta} = 67.7s^{\epsilon} + 129s^{-\eta} \quad [\mu\text{b}]. \tag{1.26}$$

The VMD part contributes approximately 80% of the total γp cross section at HERA energies. The remaining 20% are shared between the direct and anomalous event classes.

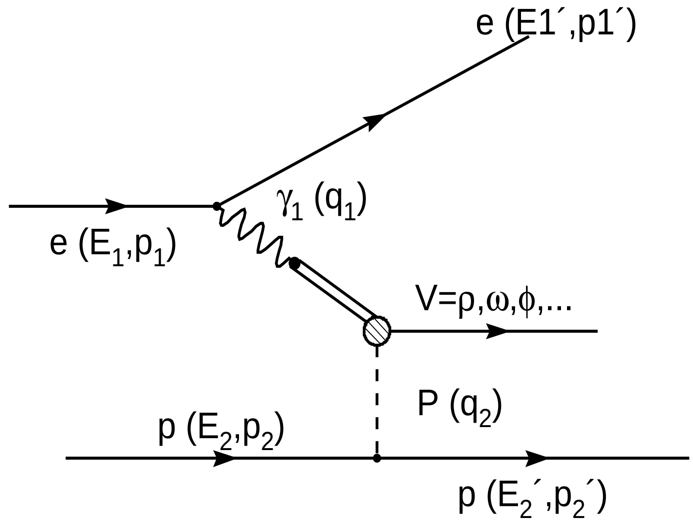

Figure 1.6: *A special case of a photoproduction event at HERA: The electron emits a photon which fluctuates into a virtual vector meson V and interacts with a Pomeron from the proton vertex. This is a typical background event to the signal (section 1.3).*

1.1.3 The Connection between Photon-Proton and Lepton-Proton Scattering

The electron can be considered as a source of virtual photons, interacting with the proton. Weizsäcker and Williams showed 1934 that at sufficiently small values for Q^2, only the transversely polarized photons $\sigma_T(x, Q^2)$ contribute (equation (1.16)), so that the ep cross section $\sigma^{ep\to eX}$ factorizes into the γp cross section $\sigma^{\gamma p\to X}$ and the probability that the electron radiates a photon:

$$\frac{d^2\sigma^{ep\to eX}}{dydQ^2} = \Phi(y, Q^2)\sigma^{\gamma p\to X}, \tag{1.27}$$

with the photon flux Φ in the Weizsäcker-Williams-approximation:

$$\Phi(y, Q^2) = \frac{\alpha}{2\pi Q^2}\left[\frac{1+(1-y)^2}{y}\right]. \tag{1.28}$$

In the special case of elastic vector meson photoproduction, an improved calculation of the photon flux is described in [FRI93, GRO97] and yields:

$$\Phi(y, Q^2) = \frac{\alpha}{2\pi Q^2}\left[\frac{1+(1-y)^2}{y} - \frac{2(1-y)}{y}\left(\frac{Q^2_{min}}{Q^2} - \frac{Q^2}{m_V^2}\right)\right]\left(1+\frac{Q^2}{m_V^2}\right)^{-2}, \tag{1.29}$$

with a hadronic scale m_V which is typically the ρ mass for convenience.

Consequently, the γp cross section can be calculated by measuring the ep cross section and dividing it by c_{EPA}, the photon flux Φ integrated over the Q^2 and y ranges covered by the measurement. This method is also called the *equivalent photon approximation* (EPA).

1.2 Regge Phenomenology and Diffraction

1.2.1 Diffractive Scattering

In DIS reactions, a colour field is stretched between the struck quark and the proton remnant. Due to fragmentation processes this leads to activity that can be over all phase space regions. In contrast, the characteristic signature of a diffractive process is the occurrence of a gap in the final state where no particles are produced and is often referred to as the rapidity gap (see equation (1.11)).

In the particle picture, every interaction is associated with a particle exchange. In diffraction this colourless particle is called the Pomeron (section 1.2.3).

Another approach comes from the similarity of diffraction and wave optics. The intensity of a ray of light, in the path of which a black disc is put, shows a diffractive pattern with minima and maxima on a plane perpendicular to the direction of the incoming light. High energy scattering can be understood as diffraction of one particle, representing the light, from another particle, representing the black disc. And in analogy to the behaviour of the intensity, the differential cross section $d\sigma/d|t|$ has one observable minimum, as shown in figure 1.7.

The following diffractive processes can be distinguished (see figure 1.8):

- **elastic processes**, as shown in figure 1.8 a), in which both scattering partners stay intact:

$$A + B \to A + B, \tag{1.30}$$

- **dissociative processes**, where at least one of the incoming particles dissociates into a higher mass state, depicted in figure 1.8 b), c) – single dissociation – and d) – double dissociation:

$$\underbrace{A + B \;\to\; X_1 + B}_{b)} \quad \text{or} \quad \underbrace{A + B \to A + X_2}_{c)} \quad \text{or} \quad \underbrace{A + B \to X_1 + X_2}_{d)}, \tag{1.31}$$

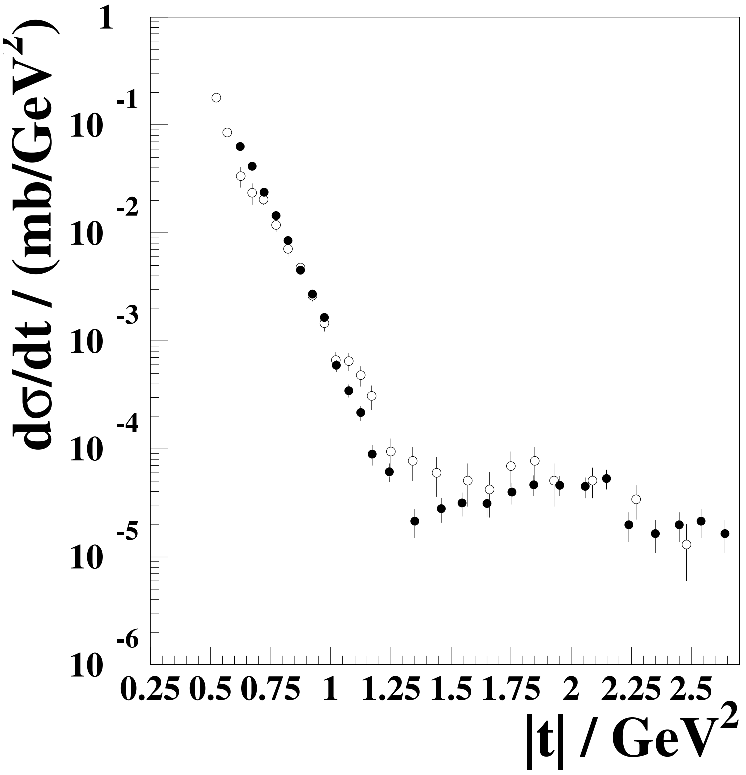

Figure 1.7: *Differential cross section $d\sigma/d|t|$ of elastic proton-proton scattering (filled circles) and $d\sigma/d|t|$ of proton-antiproton scattering (open circles) at $\sqrt{s} = 53$ GeV. The dip can be explained in analogy to wave optics as a diffraction pattern (see text). The minimum is more pronounced in case of proton-proton scattering. The data is taken from [BRE85].*

- and **non-diffractive processes** representing the remaining part of the reactions as figure 1.8 e) shows:

$$A + B \rightarrow X. \tag{1.32}$$

The process investigated in this analysis (chapter 1.3.2) is of the single diffraction type, where the proton is excited to an N^* ([PDG00]) with a mass $m_{N^*} \geq m_p$. The dependence of the cross section follows approximately a $1/m_{N^*}^2$ behaviour [DOS00]. Moreover, the diffractive state preserves the intrinsic quantum numbers of the initial proton: The total angular momentum and the isospin are preserved, but the internal motion may be affected and the spin and parity may be changed.

1.2.2 Regge Theory

The continuation of the scattering amplitude into the complex angular momentum plane leads to Regge theory. The scattering amplitude has poles in the complex angular momentum plane, and for physical values of the angular momentum ℓ these poles, called *Regge poles*, coincide with bound states and resonances.

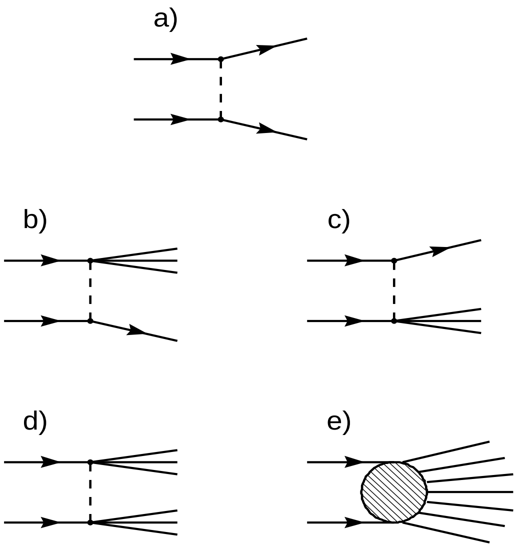

Figure 1.8: *Classification of the possible diffractive processes: elastic diffraction a), single (photon) dissociative diffraction b), single (proton) dissociative diffraction c), double dissociative diffraction d) and non-diffractive processes e). The dashed line in the pictures a)-d) represents the exchanged Pomeron.*

Soft hadron-hadron interactions are well described by Regge phenomenology [COL77]. It can be interpreted as a generalization of Yukawa's one pion exchange. Indeed, Regge theory does not only allow for one particle exchange, but the interaction is viewed as due to exchanges of collective states called Regge trajectories. The Regge trajectories can be classified into different families according to the quantum numbers B, S, I, G (Baryon number, Strangeness, Isospin, G-Parity) of the Regge poles lying on it. These trajectories are described by a function $\alpha(t)$. The connection with the mass m_R and the spin J_R of a Regge pole R is given by

$$\mathrm{Re}\,\alpha(t)|_{t=m_R^2} = J_R. \tag{1.33}$$

Figure 1.9 shows some of the well established mesons in a so-called Chew-Frautschi-diagram, where the spin J is plotted versus the square of the mass m^2 of a particle. The real part of the trajectory can be approximated by a linear behaviour:

$$\alpha(t) = \alpha_0 + \alpha' t, \tag{1.34}$$

where α_0 is the intercept and α' is the slope of the trajectory.

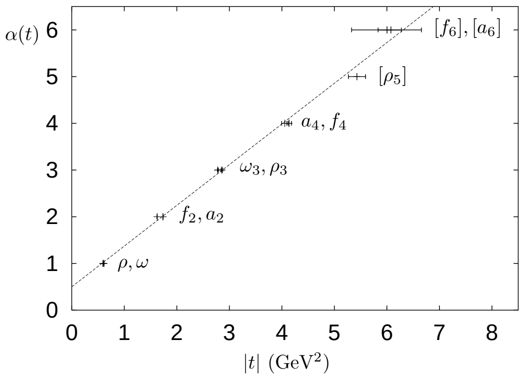

Figure 1.9: *In a Chew-Frautschi-diagram the spin of a particle is plotted versus the square of its mass. Here four degenerate Regge trajectories and the respective mesons are depicted [DON92].*

Cross Sections

Starting from a partial-wave decomposition of the scattering amplitude:

$$A(s,t) = \sum_{\ell=0}^{\infty} (2\ell+1) A_\ell(t) P_\ell(\cos\theta), \tag{1.35}$$

where $P_\ell(\cos\theta)$ are the Legendre polynomials of the first kind, θ is the scattering angle, and ℓ is the angular momentum, inserting equation (1.34) yields for the coefficients $A_\ell(t)$:

$$A_\ell(t) = \frac{\beta(t)}{\ell - \alpha(t)}. \tag{1.36}$$

At $\ell = \alpha(t)$ a Regge pole occurs with a residuum described by $\beta(t)$.

In the limit of high energies ($s \to \infty$), equation (1.35) becomes:

$$A(s,t) = \beta(t) \left(\frac{s}{s_0}\right)^{\alpha(t)}, \tag{1.37}$$

where $\beta(t)$ includes the part of the amplitude not depending on s. Hence, at high energies the s dependence of the s-channel scattering amplitude is a simple power behaviour.

The total cross section is linked to the imaginary part of the scattering amplitude by the optical theorem via [COL77]:

$$\sigma_{tot}(s) = \frac{1}{s} \mathrm{Im}\left(A(t=0)\right). \tag{1.38}$$

Inserting the scattering amplitude from equation (1.37) yields:

$$\sigma_{tot}(s) \sim \left(\frac{s}{s_0}\right)^{\alpha(0)-1}. \tag{1.39}$$

The differential elastic cross section is given by [GRO97]:

$$\frac{d\sigma_{el}}{d|t|} = \frac{|A|^2}{16\pi s^2} \sim |\beta(t)|^2 \left(\frac{s}{s_0}\right)^{2\alpha(t)-2}. \tag{1.40}$$

For fixed values of s and $s \gg |t|$ the behaviour of $|\beta(t)|^2$ is well described by an exponential dependence of the form $e^{b_0 t}$. Making use of the linear approximation of the Regge trajectory (1.34), equation (1.40) can be written as:

$$\frac{d\sigma_{el}}{d|t|} \approx N \cdot \mathrm{e}^{(2\alpha_0-2+\alpha' t)\ln(s/s_0)+b_0 t} \tag{1.41}$$

$$= \left.\frac{\mathrm{d}\sigma_{el}}{\mathrm{d}|t|}\right|_{t=0} \cdot \mathrm{e}^{-b|t|} \tag{1.42}$$

with

$$b := b_0 + 2\alpha' \ln(s/s_0). \tag{1.43}$$

1.2.3 The Pomeron

For hadron-hadron scattering the Froissart-Martin bound, derived in axiomatic field theory, limits the rise of the total cross section with the centre of mass energy to a maximum rise of the form:

$$\sigma_{tot} \leq C \left(\ln \frac{\sqrt{s}}{\sqrt{s_0}}\right)^2, \tag{1.44}$$

with an a priori unknown scaling factor s_0.

Figure 1.10 shows the total cross sections for $pp(\bar{p})$,$\pi^{\pm}p$,$K^{\pm}p$ and γp depending on $\sqrt{s}$. For small energies the cross section falls which is compatible with the trajectories of the well known mesons (figure 1.9). Even the highest lying trajectory (ρ^0,ω,f_2,etc.), parameterized by [DON84]

$$\alpha_{\rho^0,\omega,\ldots}(t) = 0.44 + 0.93 GeV^{-2} \cdot t, \tag{1.45}$$

has an intercept $\alpha_0 = 0.44 < 1$ and thus, inserting α_0 in equation (1.39), σ_{tot} falls.

However, with increasing energy the cross section is observed to rise. In order to explain this behaviour a further trajectory was introduced, called the Pomeron trajectory[2]:

$$\alpha_{I\!P} = 1 + \delta + \alpha'_{I\!P} \cdot t, \tag{1.46}$$

with $\delta > 0$. In analogy to the other trajectories, the possibility of bound states lying on the Pomeron trajectory arises; "glueballs" are supposed to be candidates for such resonances [ABA94] (see figure 1.11). Another approach, motivated by [DON89, CUD90], describes the Pomeron as a colourless system of two gluons (see figure 1.12) that interact with the partons of the scattered particles. The Pomeron has the quantum numbers of the vacuum

[2]named after the Russian physicist Isaak Jakowlewitsch Pomeranchuk (1913 - 1966)

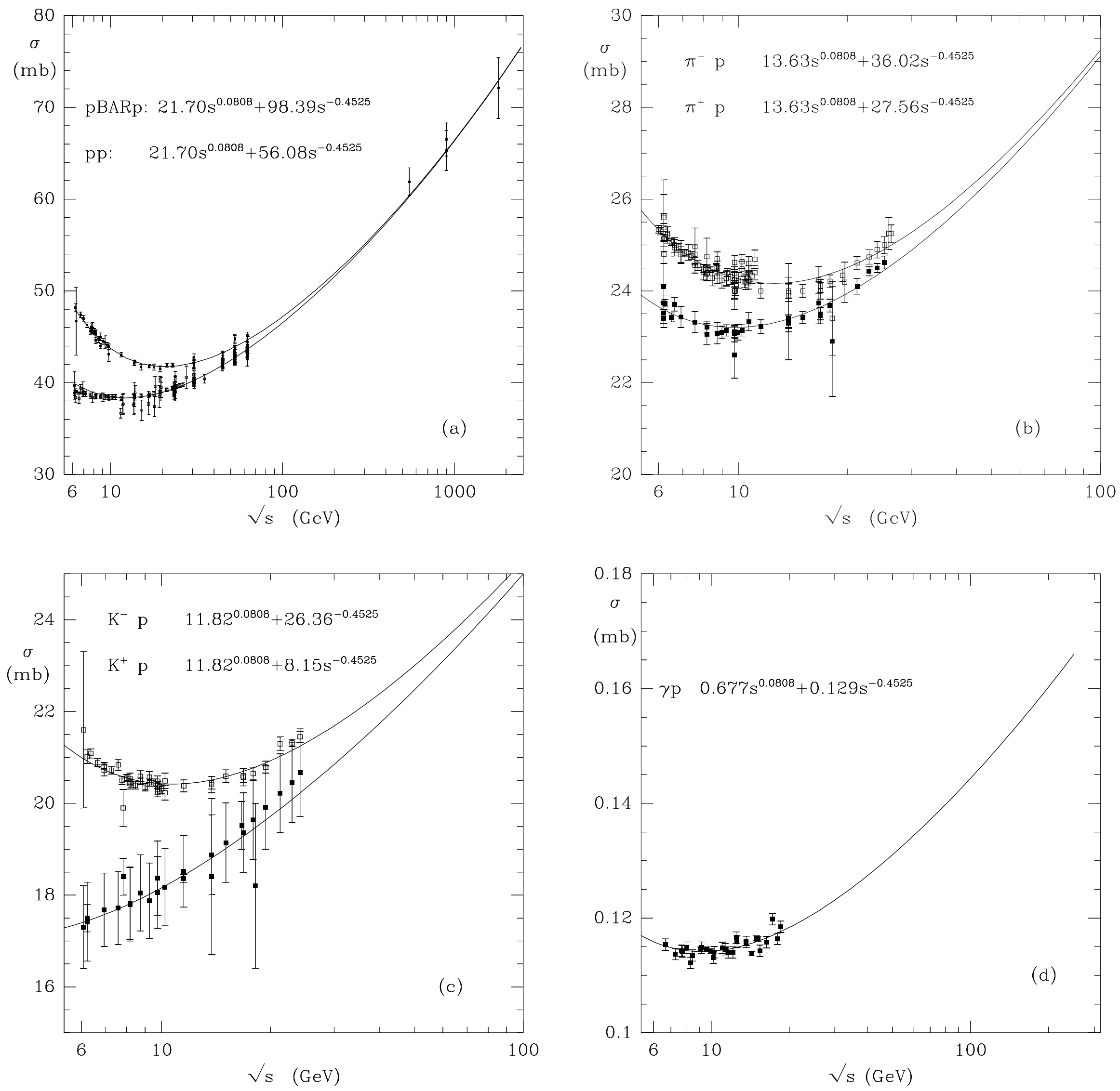

Figure 1.10: *Total cross sections for pp, $\bar{p}p$-, $\pi^{\pm}p$-, $K^{\pm}p$- and γp-scattering depending on the centre of mass energy are depicted. Fits of the form of equation (1.47) are plotted, whereby ϵ and η are obtained from the proton-(anti-)proton data, and X is required to be the same for $\sigma(AB)$ and $\sigma(\bar{A}B)$. Values for X^{AB} and Y^{AB} are given [DON92].*

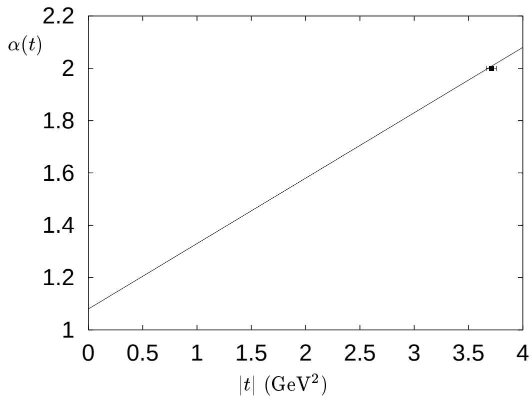

Figure 1.11: *The Pomeron trajectory with the line $\alpha(t) = 1.0808 + 0.25t$ is depicted including a 2^{++} glueball candidate [ABA94].*

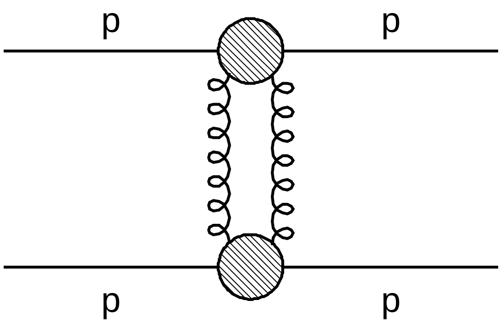

Figure 1.12: *The picture shows the Pomeron as a colourless system of two gluons and their coupling to two hadrons.*

(i.e. $B = Q = S = I = 0$, $P = C = G = +1$), so its couplings to a particle A and its antiparticle $\bar{A}$ are equal. Donnachie and Landshoff [DON92] made a simultaneous fit to the pp and $p\bar{p}$ data (figure 1.10) of the form:

$$\sigma_{tot}^{AB} = X^{AB} s^{\epsilon} + Y^{AB} s^{-\eta}. \tag{1.47}$$

The first term in equation (1.47) describes the Pomeron exchange and the second the effective Reggeon[3] exchange, showed in figure 1.9. Since the cross sections for Pomeron exchange should be equal for both particles and antiparticles, $X^{AB} = X^{\bar{A}B}$, in addition the same coefficients for the values ϵ and η are required. For the exponents the fit yielded:

$$\epsilon = 0.0808 \quad \text{and} \quad \eta = 0.4525. \tag{1.48}$$

For all other fits in figure 1.10 the same values of these two parameters are used.

[3]Abbreviation for Regge trajectory

For the maximum accessible centre of mass energies of $\sqrt{s} = 1800$ GeV, data are well described by the Pomeron ansatz as in (1.47), although at some energy this parametrisation will violate the Froissart-Martin bound (equation 1.44). This indicates that the asymptotic region has not yet been reached.

The slope $\alpha'_{I\!P}$ of the Pomeron trajectory (1.46) was fitted in [DON84]:

$$\alpha'_{I\!P} = 0.25\ \mathrm{GeV}^{-2}, \tag{1.49}$$

which is smaller compared to the meson trajectories (1.45). In figure 1.11 the determined Pomeron trajectory is plotted.

For photoproduction (section 1.1.2) the fitted coefficients are compatible with the measurements by H1 [AHM93] and ZEUS [DER92]:

$$X^{\gamma p} = 0.0677 \quad ; \quad Y^{\gamma p} = 0.129. \tag{1.50}$$

1.2.4 The Odderon

Like the Pomeron, the Odderon is a postulated Regge trajectory. The intercept is supposed to be $\alpha_{\mathbb{O}} \approx 1$ and the slope $\alpha'_{\mathbb{O}}$ between 0 and 1 GeV^{-2}. The Pomeron carries vacuum quantum numbers $C = P = +1$. The phenomenological (non-perturbative) Odderon is introduced as the $C = P = -1$ partner of the Pomeron, which is done in [LUK73], and therefore, the Odderon has the same quantum numbers as an exchanged photon. The name Odderon is an abbreviation for ***Odd****-under-crossing-Pom****eron***. In a partonic picture [DON91] the Odderon is most easily modelled, in analogy to the Pomeron, by three gluons. This corresponds to the model shown in figure 1.12 with an additional gluon.

If the amplitude T for $pp \to pp$ scattering contains a part *odd under crossing*, it changes its sign in the crossed reaction: $p\bar{p} \to p\bar{p}$. Decomposing the scattering amplitude in contributions of even (T_+) and odd (T_-) C-parity, one can write:

$$T_{pp} = T_+ + T_- \quad \text{and} \quad T_{p\bar{p}} = T_+ - T_-. \tag{1.51}$$

Pomeranchuk's theorem states that the ratio of the cross sections for particle-antiparticle and particle-particle asymptotically goes to unity:

$$\frac{\sigma(T\bar{T})}{\sigma(TT)} \to 1 \quad \text{for} \quad s \to \infty, \tag{1.52}$$

which does not imply that the difference $\Delta\sigma$ goes to 0. Indeed the existence of an Odderon would produce a difference between pp and $p\bar{p}$ scattering at high energies and small momentum transfers,

$$\Delta\sigma = \sigma_{tot}(p\bar{p}) - \sigma_{tot}(pp) \neq 0, \tag{1.53}$$

due to the different amplitudes $T_{pp} = T_+ + T_- \neq T_{p\bar{p}} = T_+ - T_-$ and

$$T_+ \to T_{I\!P} \quad \text{and} \quad T_- \to T_{\mathbb{O}} \quad \text{for} \quad s \to \infty, \tag{1.54}$$

with $T_{I\!P}$ representing Pomeron and $T_{\mathbb{O}}$ Odderon exchange.

Figure 1.10 (a) shows the measured cross sections for pp and $p\bar{p}$ scattering as a function of the centre of mass energy $\sqrt{s}$. A more sensitive test is provided by the measurement of the real and imaginary part of the scattering amplitudes by introducing the parameter

$$\rho := \mathrm{Re}T/\mathrm{Im}T, \tag{1.55}$$

which is shown in figure 1.13. Both pictures are consistent with the absence of Odderon exchange. There are two possible explanations for the apparent absence of the Odderon:

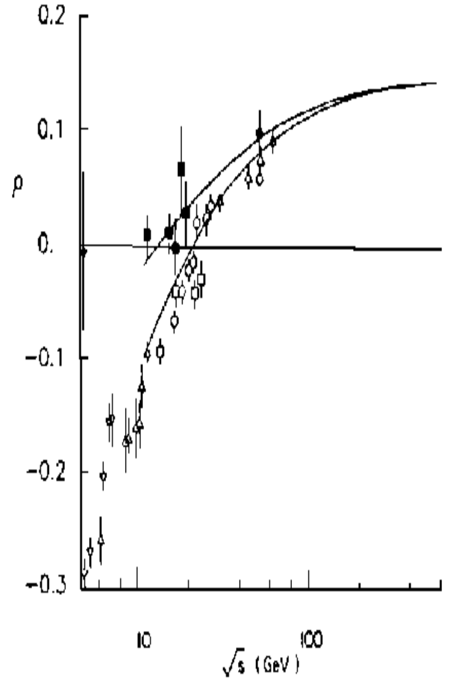

Figure 1.13: *The behaviour of the parameters ρ_{pp} and $\rho_{p\bar{p}}$ (defined in (1.55)) with $\sqrt{s}$ is shown. No evidence for the existence of the Odderon can be found. The open (filled) symbols are related to the elastic pp ($p\bar{p}$) scattering. The curves are the results of the model of Donnachie and Landshoff ([DON84] and figure 1.10).*

1. the non-perturbative Odderon does not exist.
2. the non-perturbative Odderon does exist, but its coupling to the nucleon in elastic scattering at small t is extremely small, so it evaded detection in previous experiments.

Since QCD-based models of the phenomenological Pomeron can easily be extended to describe a phenomenological Odderon, the first item seems implausible. In the next section 1.3 a model is presented that on parton level holds Odderon and Pomeron contributions of the same order of magnitude, but at the same time provides a mechanism that suppresses these Odderon contributions in the elastic scattering.

1.3 Odderon-Photon Fusion at HERA

1.3.1 Model of the Stochastic Vacuum (MSV)

A remarkably good description of high-energy diffractive scattering involving Pomeron exchange [DOS94, BER99b] is based on functional integral techniques [LAN87, NAC91] and the usage of the Model of the Stochastic Vacuum (MSV) [DOS87].

In [BER99] this model is extended to the exchange of a $C = P = -1$ object, the Odderon. Calculating the pp scattering amplitude for protons in the quark-diquark-picture, the Odderon contributions cancel when evaluating the integrals over all angles: The quark-diquark-density in the proton is symmetric under parity transformation while the $C = P = -1$ contributions change sign. Within the MSV the cross section depends crucially on the diquark size d. For $d < 0.3$ fm, the Odderon coupling is sufficiently suppressed in order to be able to describe the measurements of the hadron-hadron-scattering amplitudes at high energies and small momentum transfer.

This treatment of the Odderon, as a simple Regge pole near $J = 1$, is the simplest model in agreement with data. However, including double and triple poles would reduce the suppression of Odderon exchange in pp and $p\bar{p}$ scattering.

1.3.2 Phenomenology of the Process

In order to study the Odderon, it is advantageous to find a reaction that permits Odderon exchange but excludes Pomeron exchange. Exclusive production of neutral pseudoscalar mesons (PS) in ep scattering at HERA energies is such a process. The Pomeron can not contribute since the PS has positive C parity. First, the elastic case is discussed and afterwards the situation, in which the proton is transformed into an excited state.

The Elastic Case

The MSV In this model, diquark clustering in the proton explains the suppression of the Odderon coupling. In [RUE98] the differential and total cross sections for $\gamma p \to \pi^0 p$ are calculated. Figure 1.14 shows that the results have a strong dependence on the diquark size d.

The Model of Nachtmann et al. For comparison another model is explained briefly covering only the non-dissociative case. The elastic cross section has been calculated in [KIL97], using a simple ansatz for the Odderon. The cross section due to Odderon exchange (figure 1.15) is of the same order of magnitude as the cross section due to photon-photon fusion. However the interference $\gamma\gamma/\gamma\mathbb{O}$ in the p_t distribution could allow for a determination of the strength of the proton-Odderon coupling.

Single Proton Dissociation in the MSV

Things change for single proton dissociation [BER99a], where suppression due to diquark clustering is absent, even for a point-like diquark, since the overlap of the wave functions of

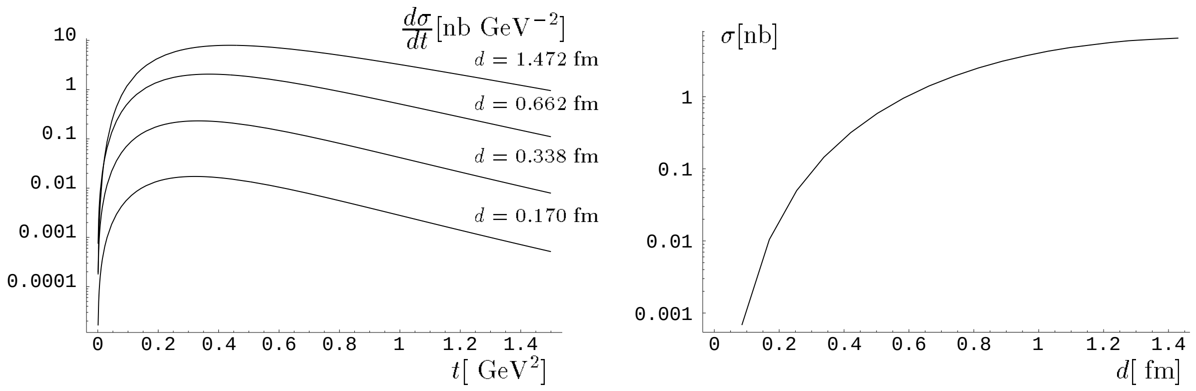

Figure 1.14: *The differential and total cross sections for $\gamma p \to \pi^0 p$ for $Q^2 = 0$. The differential cross section is given for different diquark sizes. The total cross section shows a strong d dependence. A diquark size $d < 0.3$ fm is in agreement with the upper limit allowed by the measurement of the forward real part of the pp and $p\bar{p}$ scattering amplitudes [RUE98].*

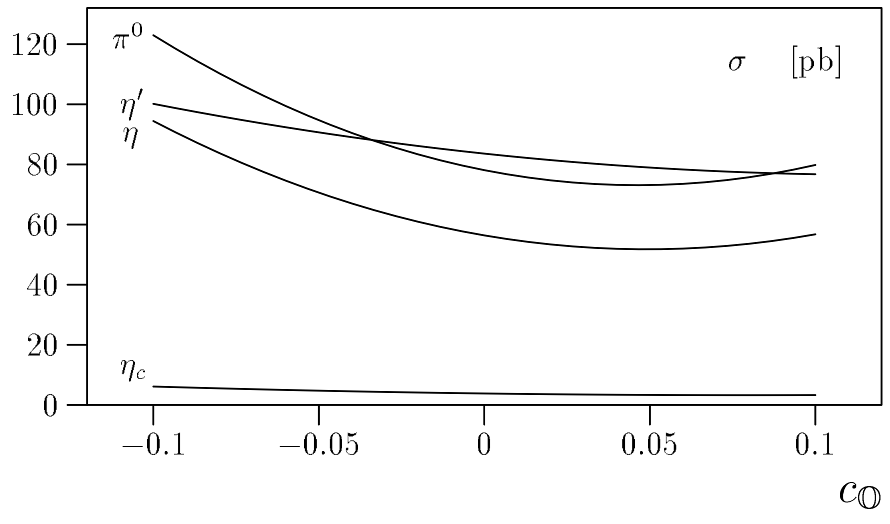

Figure 1.15: *Total γp cross section for elastic pseudoscalar meson production in the photoproduction regime in an alternative model of Nachtmann as a function of the variable $c_{\mathbb{O}}$ which can be interpreted as the Odderon coupling in terms of the Pomeron coupling [KIL97].*

the incoming proton and the outgoing (quasi-) diffractively excited nucleon is antisymmetric. Furthermore the leading contribution for single dissociation is of the order $\mathcal{O}(d^0)$ and therefore, in contrast to the strong d^4 dependence for the elastic case (figure 1.14), the cross sections for proton excitation are rather independent of d. Figure 1.16 depicts the total cross sections, showing that the cross section with nucleon fragmentation is orders of magnitude higher.

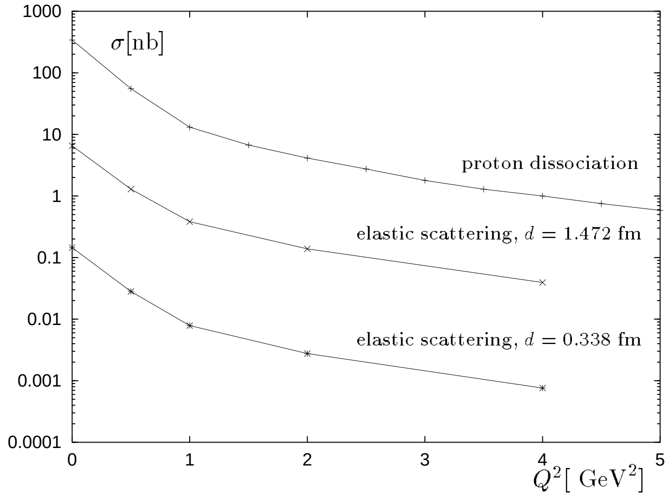

Figure 1.16: *The total γp cross section for π^0 production in single proton dissociation as a function of Q^2 is compared to the elastic case with a diquark size d of 1.472 fm and 0.338 fm respectively. The extrapolated cross section in single dissociation to the photoproduction region $Q^2 < 0.01 GeV^2$ is 341 nb [RUE98].*

The reaction considered can be written as:

$$e^{\pm}(p_1) + p(p) \rightarrow e^{\pm}(p_1') + PS(k) + X(p_X). \tag{1.56}$$

Figure 1.17 (a) illustrates the reaction in a Feynman diagram and explains the notation used.

The breakup of the proton with $J^P = \frac{1}{2}^+$ through Odderon exchange leads to resonances in the final state of the nucleon with negative parity. In [BER99a], the differential and total γp cross section in the photoproduction regime (figure 1.3, equation (1.14)) for the Odderon induced production of a π^0 pseudoscalar are determined. Only the two nucleon resonances $N^*(1520)$ and $N^*(1535)$ with lowest mass, which have negative parity ($[J^P] = \frac{3}{2}^-$ and $[J^P] = \frac{1}{2}^-$, respectively) are considered. The corresponding electron proton cross section is calculated via the equivalent photon approximation (1.1.3).

1.3.3 The Calculation

Two extreme approaches to the calculation exist: Either any structure in the proton's final state is ignored and it is represented by a free quark-diquark pair, or the excited proton is dominated by a small number of resonances, which is discussed here.

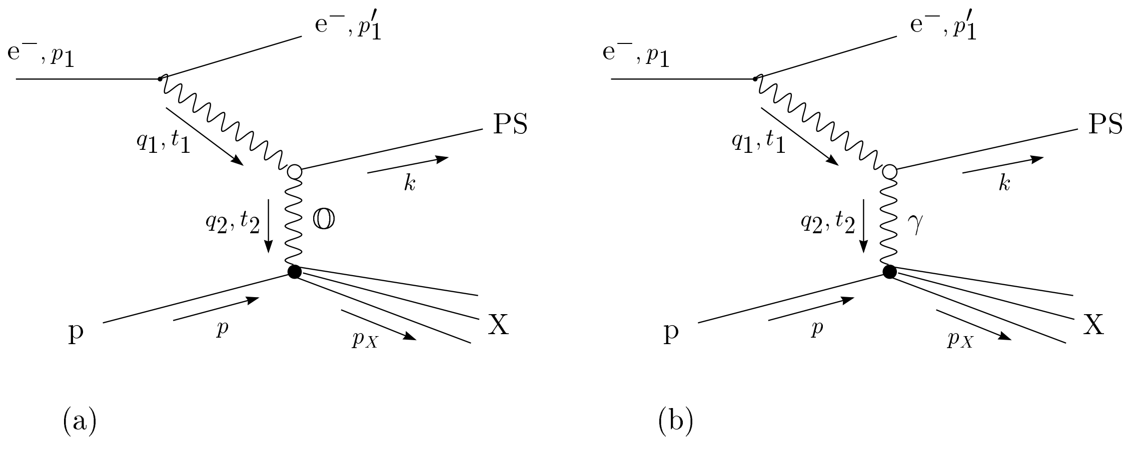

Figure 1.17: *On the left hand side the Feynman diagram of the Odderon induced process investigated in this analysis is shown (a). Its signature is a high energetic pseudoscalar meson ($PS = \pi^0, \eta, \eta', \eta_c$) in the backward direction. On the right hand side the Odderon is replaced by a photon (b) which results in a indistinguishable background process.*

The differential γp-cross section can be written as:

$$\frac{d\sigma^{\mathbb{O}}_{\gamma p}}{dt_2} = \frac{1}{16\pi s^2_{\gamma p}} \frac{1}{2} \sum_{\lambda} \sum_{\lambda_\gamma} |T_{\lambda,\lambda_\gamma}|^2, \tag{1.57}$$

with the squared four-momentum transfer t_2 (see figure 1.17) and the helicities λ_γ, λ of the photon and the orbital helicity of the resonance, respectively. The scattering amplitude $T_{\lambda,\lambda_\gamma}(s_{\gamma p}, t_2)$ calculated in the γp centre of mass system is given by:

$$T_{\lambda,\lambda_\gamma}(s_{\gamma p}, t_2) = 2is_{\gamma p} \int d^2b e^{i\mathbf{q_{2\perp}}\mathbf{b}} J_{\lambda,\lambda_\gamma}(\mathbf{b}), \tag{1.58}$$

where $\boldsymbol{q_{2}}_\perp$ is the transverse part of $\boldsymbol{q_2}$ given in figure 1.17(a). The hadron-hadron profile function $J(\boldsymbol{b})$ is determined in the MSV [DOS94] by a convolution of the loop-loop scattering amplitude $J_{LL}(\boldsymbol{b}, \boldsymbol{r_1}, z_1, \boldsymbol{r_2}, z_2)$ with the wave functions of the initial and final state, respectively. $\boldsymbol{b}$ is the impact parameter of two lightlike dipole trajectories with transverse size $\boldsymbol{r_1}$ and $\boldsymbol{r_2}$ respectively, and the variables z_1 and z_2 correspond to the longitudinal momentum fractions of the quarks in the dipoles.

Smearing the dipole extensions $\boldsymbol{r_i}$ with the respective transition densities, the hadronic amplitude can be expressed through:

$$J_{\lambda,\lambda_\gamma}(\boldsymbol{b}) = \int \frac{d^2r_1}{4\pi} dz_1 \int \frac{d^2r_2}{4\pi} \underbrace{\sum_{f,h_1,h_2} \psi^{*\pi^0}_{fh_1h_2}(\boldsymbol{r_1}, z_1) \psi^{\gamma}_{\lambda_\gamma, fh_1h_2}(\boldsymbol{r_1}, z_1)}_{\text{photon-pion overlap}} \underbrace{\psi^{*2P}_{\lambda}(\boldsymbol{r_2}) \psi^{p}(\boldsymbol{r_2})}_{\text{proton-proton final state overlap}} J_{LL}(\boldsymbol{b}, \boldsymbol{r_1}, z_1, \boldsymbol{r_2}, z_2), \tag{1.59}$$

with a Gaussian ansatz for the quark-diquark wave function of the proton:

$$\psi^p(\boldsymbol{r_2}) = \frac{\sqrt{2} e^{-r_2^2/4S_p^2}}{S_p}, \tag{1.60}$$

where S_p is a parameter describing the proton size. For the low-lying degenerate excited states, a wave function in a P-state analogous to the proton was chosen:

$$\psi^{2P}_{\lambda}(\boldsymbol{r_2}) = \frac{r_2 e^{-r_2^2/4S_p^2}}{S_p^2} e^{i\lambda\theta_2}, \tag{1.61}$$

with the same extension parameter S_p as for the proton. The dependence on the longitudinal momentum fraction on the proton side z_2 is neglected.

The detailed discussion can be found in [BER99a, BER99] and references therein with the photon-pion overlap taken from [RUE98].

The resulting differential cross section is shown in figure 1.18. The parameters of the

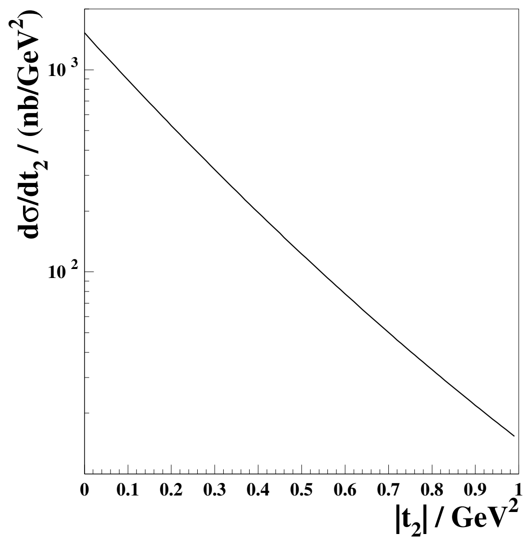

Figure 1.18: *The differential cross section $d\sigma^{\mathbb{O}}_{\gamma p}/dt_2$ of the process $\gamma p \to \pi^0\{2P\}$ as a function of t_2.*

model are fixed at a γp-centre of mass energy of $\sqrt{s_{\gamma p}} = 20$ GeV. The energy scaling of the cross section was argued to behave like [BER99a]:

$$c(s_{\gamma p}) = \left(s_{\gamma p}/400\mathrm{GeV}^2\right)^{0.15}. \tag{1.62}$$

The total cross section is obtained by integration:

$$\sigma^{\mathbb{O}}_{\gamma p}(\gamma p \to \pi^0\{2\mathrm{P}\}) = \int d|t_2| \frac{d\sigma^{\mathbb{O}}_{\gamma p}}{d|t_2|}. \tag{1.63}$$

The results are shown in table (1.1).

final state unit	MSV		lower limit		mean		upper limit	
	$\sigma^{\mathbb{O}}_{\gamma p}$	$\sigma^{\mathbb{O}}_{ep}$	$\sigma^{\mathbb{O}}_{\gamma p}$	$\sigma^{\mathbb{O}}_{ep}$	$\sigma^{\mathbb{O}}_{\gamma p}$	$\sigma^{\mathbb{O}}_{ep}$	$\sigma^{\mathbb{O}}_{\gamma p}$	$\sigma^{\mathbb{O}}_{ep}$
$e\pi^0\{2\mathrm{P}\}$ [nb]	294	4.01	562	7.66	597	8.14	638	8.70
$e\pi^0\mathrm{X}$ [nb]	341	4.64	651	8.86	692	9.41	740	10.06
$\sigma^{\gamma}_{ep}(ep \to e\pi^0\mathrm{X})$ [nb]	0.0020		0.0038		0.0041		0.0043	
$\sqrt{s_{\gamma p}}$ [GeV]	20		174		211		266	
scaling factor $c(s_{\gamma p})$	1		1.91		2.03		2.17	
c_{EPA}	0.0136							

Table 1.1: *The Odderon induced γp and ep cross sections are given treating the final state as a small number of resonances (2P) or as a free quark-diquark pair (X). For comparison the ep cross section for photon-photon fusion is shown [BER99a]. In the following row the γp centre of mass energy used in the model and accessible in the data (photoproduction region see equation (1.14)) is given, calculated via the approximation $\sqrt{s_{\gamma p}} = \sqrt{ys}$ (5.17). From this follows the scaling factor using equation (1.62). c_{EPA} is evaluated via equation (1.29) for pseudoscalar meson production and integration over the accessible ranges in y and Q^2.*

Finally, an estimate of the uncertainty is given. Due to uncertainties coming from the sensitivity to the parameters of the MSV or the proton-2P overlap etc., the uncertainty on the cross section in this model could be a factor of the order of 2 [BER99a].

1.3.4 The Photon-Photon Contribution

Because the quantum numbers of the photon are the same as the Odderon, photon-photon fusion, where in Feynman-diagram 1.17 (a) the Odderon is replaced by a photon as seen in 1.17 (b), can lead to the same final state as the Odderon-photon fusion. The inelastic cross section for π^0 production with a (quasi-) diffractively excited proton is calculated in [BER99a], summing over all hadron final states with an invariant mass accessible at HERA (see table 1.1). The contributions are very small compared with the elastic case from phase space arguments in the limit $t_2 \to 0$ (left plot in 1.19). The right plot in 1.19 shows that the cross section for Odderon exchange is significantly larger than for photon-photon fusion (see also table 1.1).

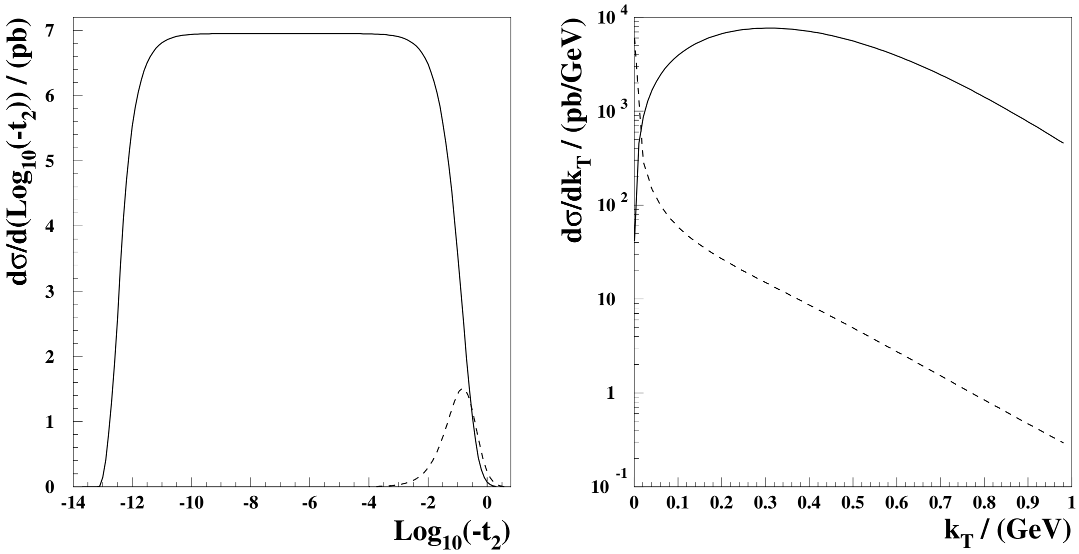

Figure 1.19: *The plot on the left hand side shows the* $\log_{10}(-t_2)$ *distribution for elastic (solid line) and inelastic (dashed line)* π^0 *production in photon-photon-fusion, integrated over the whole resonance region. On the right hand side the pion's transverse momentum* k_T *distribution for Odderon exchange (solid line) is compared to the result for photon exchange (dashed line), summed over the elastic and inelastic channels.*

1.4 Kinematics of the Pion Decay

The process introduced in equation (1.56) with the Feynman diagram from figure 1.17(a) predicts a pseudoscalar in the final state. The presented analysis deals with the evidence of the π^0 via the detection of the two photons into which the pion decays. In this section the kinematics of the decay:

$$\pi^0 \to \gamma\gamma \tag{1.64}$$

are elaborated.

Two calorimeters allow for the detection of the two photons: The VLQ and the Spacal (described in chapter 3 and section 2.4, respectively). These calorimeters have a certain geometric and energy acceptance, therefore it is worthwhile to investigate the energy and angular distributions of the considered photons.

The coordinate system, used to describe the kinematics, is chosen such that the pion propagates along the $+z$-axis. In addition to the laboratory system (in the following called *lab*) it is informative to also consider the centre of mass system of the pion (in the following called CM) obtained by a Lorentz boost in the $-z$ direction. Since the system possesses rotational symmetry, there is no dependence on the azimuthal angle ϕ. The following variables are useful in understanding the kinematic characteristics of the reaction:

- The pion decay angle of the most energetic photon γ_1 (as defined in the lab system):

$$\theta_{\gamma_1,CM} \qquad \text{with} \qquad 0 \leq \theta_{\gamma_1,CM} \leq \pi/2.$$

The allowed range is restricted by the fact that the photon with highest energy always moves in the forward ($+z_{CM}$) direction. This variable already determines the kinematical configurations of the decay for a given pion energy $E_{\pi^0,lab}$.

- The opening angle of the two photons in the lab system:

$$\Phi_{\gamma_1\gamma_2,lab}.$$

- The energies of the two photons in the lab system:

$$E_{\gamma_1,lab} \qquad \text{and} \qquad E_{\gamma_2,lab}.$$

Figure 1.20 shows the dependence of $\Phi_{\gamma_1\gamma_2,lab}$ on $\cos\theta_{\gamma_1,CM}$. The pion decay is isotropic, which means that the phase space is proportional to the solid angle $\mathrm{d}\phi\mathrm{d}\cos\theta_{\gamma_1,CM}$ and therefore flat in $\cos\theta_{\gamma_1,CM}$.

The experimental conditions restrict the values of y (see section 2.8), which means a restriction of the possible energies of the virtual photon, emitted by the electron. The produced pion gets its energy mainly from the photon, $E_{\pi^0} \approx E_{\gamma^*}$. Using equation (1.15), the accessible range of pion energies (see figure 4.1 (c)) can be calculated:

$$8\ \text{GeV} \lesssim E_{\pi^0} \lesssim 20\ \text{GeV}. \tag{1.65}$$

Figure 1.21 shows the energies of the two photons as a function of the opening angle and as a function of the pion decay angle, respectively.

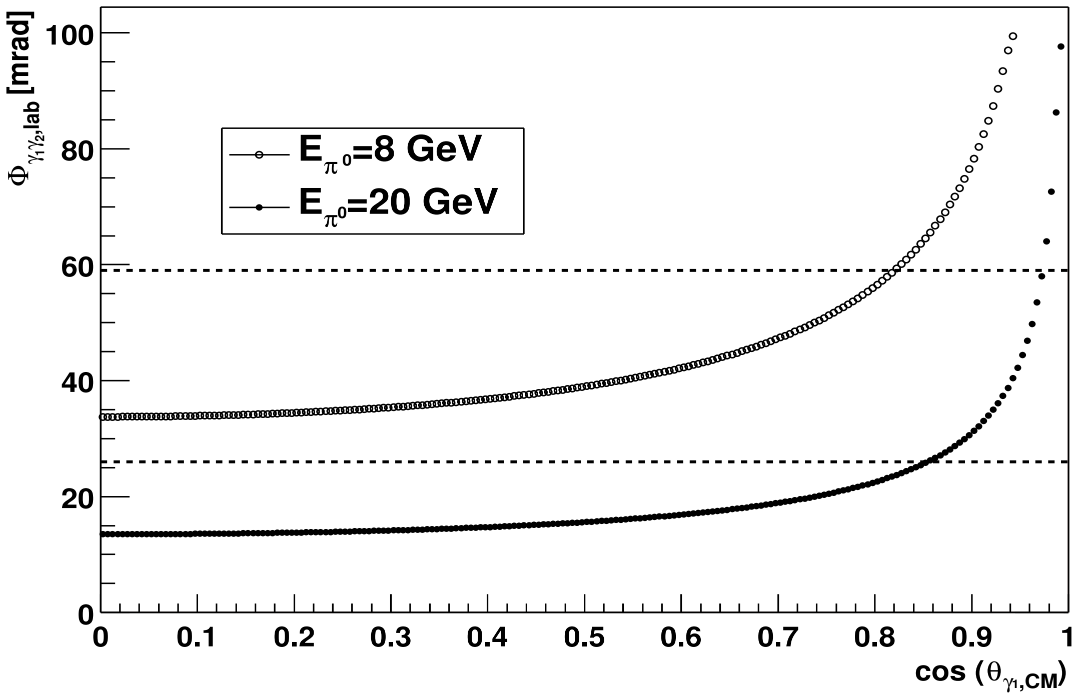

Figure 1.20: *The opening angle $\Phi_{\gamma_1\gamma_2,lab}$ of the two photons from the pion decay is shown as a function of the decay angle of the most energetic photon. The maximum and the minimum detectable pion energies are considered (20 GeV, filled circles;8 GeV, open circles). Only the range up to 100 mrad is shown, but all values for the opening angle are possible ("a photon can not be overtaken").The pion decay is isotropic resulting in a phase space which is flat in $\cos\theta_{\gamma_1,CM}$ where the cosine takes the spherical projection into account. Thus the abscissa is a linear representation of the phase space. The two dashed lines define the geometric acceptance of a pion for a special configuration: one photon in the upper VLQ module and one in the lower (see figure 5.3). It can be seen that the geometric acceptance for low energetic pions is larger than for high energetic pions ($\approx$ 15% for 20 GeV pions and $\approx$ 80% for 8 GeV pions). The other configurations are defined by $\Phi_{\gamma_1\gamma_2,lab} \lesssim 44$ mrad (both photons in the identical VLQ module), and $\Phi_{\gamma_1\gamma_2,lab} \gtrsim 22$ mrad (one photon in the VLQ and one in the Spacal).*

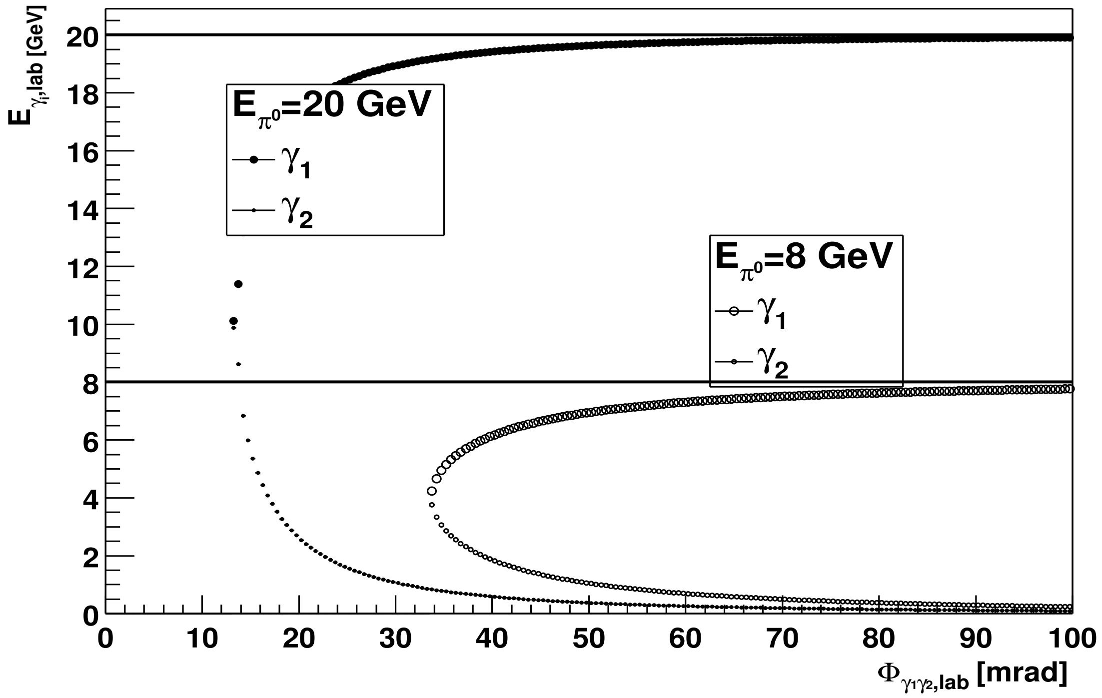

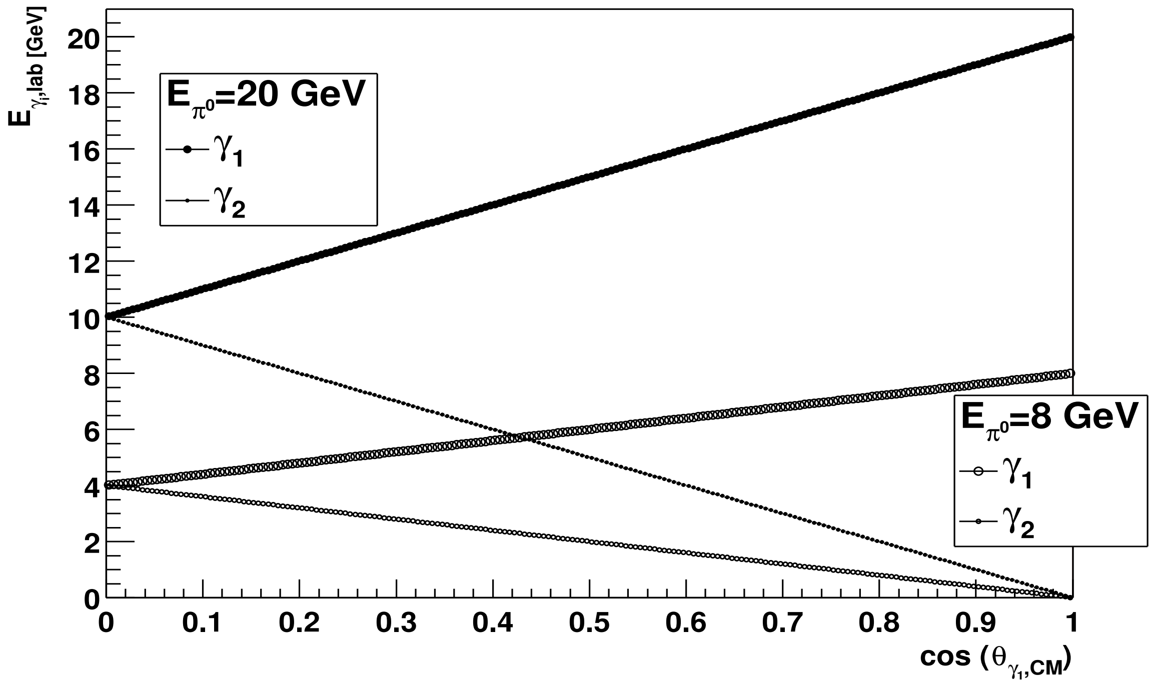

Figure 1.21: *The upper plot shows the energies of the two photons as a function of the opening angle of the two photons. The maximum and the minimum detectable pion energies are considered (20 GeV, filled circles; 8 GeV, open circles). At each case the highest energetic photon is represented by large circles and the lowest energetic photon by small circles. The lines give the respective maximum accessible energy. It can be seen that the minimum angle is assumed for maximum energy of the pion and equal energies of the two photons. In the lower plot the photon energies depend on the pion decay angle. The linear dependence reveals that all possible energy configurations of the two photons occur with the same probability.*

Chapter 2

HERA and the H1 Detector

2.1 The *ep* Collider HERA

At the Deutsches Elektronen-Synchrotron (DESY) in Hamburg, the storage ring HERA (Hadron-Elektron-Ring-Anlage) [HER81] has been in operation since 1991 (figure 2.1), colliding

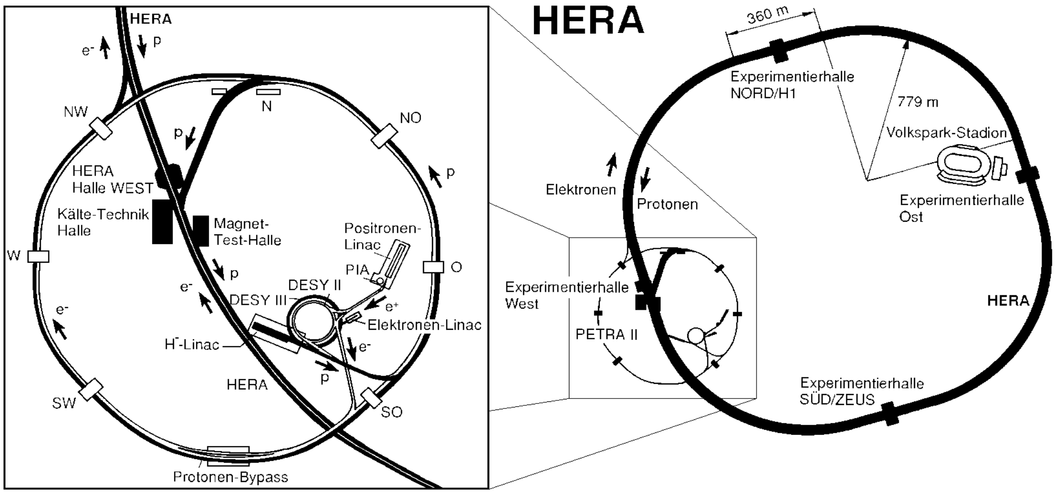

Figure 2.1: *Schematic overview of the storage ring complex HERA*

electrons[1] with an energy of $E_e = 27.56$ GeV and protons with an energy of $E_p = 920$ GeV head-on[2]. Consequently, the centre of mass energy available for a typical reaction is:

$$\sqrt{s} \approx \sqrt{4E_eE_p} \approx 318.5 \text{ GeV}. \tag{2.1}$$

For photoproduction, the (γp) centre of mass energy is only around 200 GeV. The beam particles are injected into two parallel rings, separated by 1 m, one on top of the other, and with a circumference of 6.3 km. In order to minimize beam particle interactions with gas

[1] e^+: 94-97, 99-00. e^-:98-99. In the following, the term electron is used for both electrons and positrons
[2] 820 GeV: 94-98. 920 GeV: 98-00.

atoms, the beam pipes are highly evacuated with a remaining pressure of about 10^{-9} hPa. In order to keep the protons and electrons in their proper orbit in the ring accelerator, magnetic fields are applied. The higher proton energies necessitate the use of superconducting magnets, whereas conventional magnets are used for the electrons.

In figure 2.1, the system of pre-accelerators (PIA, DESY II/III, PETRA) is illustrated. The pre-accelerators are used to prepare the beam particles before they are finally injected into the two main accelerators of the HERA ring. First the protons are accelerated to an energy of 40 GeV and injected into HERA. When enough protons are accumulated in the ring, they are accelerated to their final energy. Subsequently, the pre-accelerated electrons are injected with an energy of 12 GeV and later accelerated to an energy of 27.56 GeV.

The particle beams are not continuous but consist of 175 bunches, separated from each other by 96 ns. Each bunch contains 10^{10} - 10^{11} particles.

In addition, so-called pilot-bunches are injected. These are bunches of electrons and protons respectively that have no colliding partner. They serve to estimate the background event rate caused by interactions between the beam and the rest gas or between the beam and the beam pipe.

The relevant physical reactions take place at four points where the particle beams collide. Two of the experiments, H1 and ZEUS, operate in the experimental North and South Halls with the goal to examine the structure of the proton in previously inaccessible kinematical regions. The other two experiments work with fixed targets. In the West Hall, HERMES studies the spin structure of the proton with the aid of the electron beam. In the East Hall HERA-B is designed to study CP-violation in the neutral B-meson system making use of the proton beam.

2.2 The H1 Detector

Figure 2.2 shows a cross-section through the H1 detector. A detailed description is given in [H1D97]. Its main components are listed in the legend of the figure. The electrons and the protons collide in the centre of the detector. The main task of the detector is to detect as many of the produced particles as possible, identify them and determine their four momenta. Therefore it covers almost the entire solid angle.

The right handed H1 coordinate system is chosen as follows: the $+z$-axis is identical with the direction of the protons, called the forward direction, and the $+x$-axis is oriented horizontal and points to the centre of the storage ring HERA. Since the proton energy is much higher than the electron energy, the centre of mass of the electron-proton-system is boosted in the proton direction and thus the energy flow and particle production is concentrated mainly in this direction. This asymmetry is reflected by the construction of the detector which is considerably more massive and highly segmented in the forward direction than in the backward direction, as can be seen in figure 2.2.

The individual components are discussed in the following sections, with an emphasis on the components used in this analysis:

- the VLQ (**V**ery **L**ow $\mathbf{Q}^2$ calorimeter), between $\boxed{7}$ and $\boxed{12}$, figure 3.4, chapter 3
- the Spacal (**Spa**ghetti **Cal**orimeter), $\boxed{12}$, section 2.4

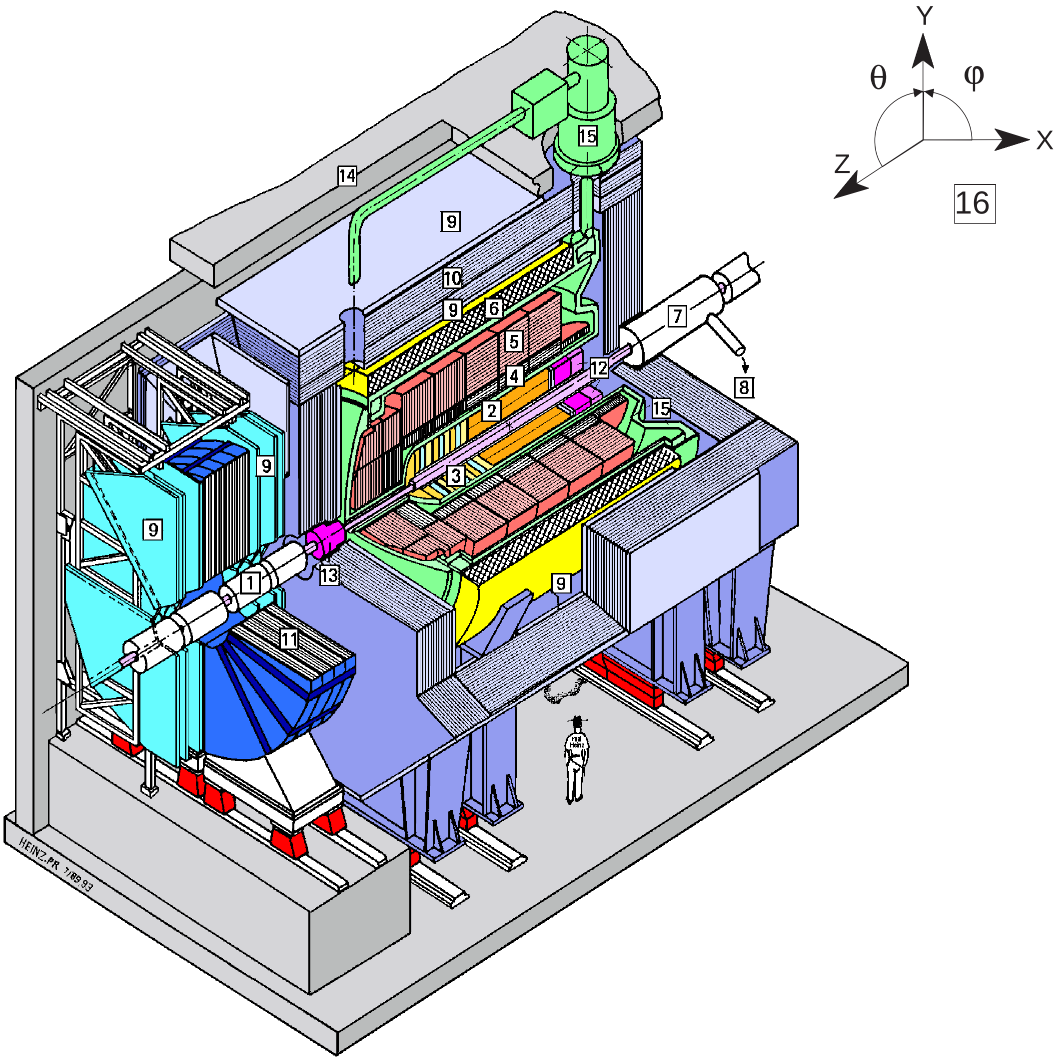

1 Beam pipe and beam magnets
2 Central track detectors
3 Forward track detectors
4 Electromagnetic LAr calorimeter
5 Hadronic LAr calorimeter
6 Superconducting coil (1.15 T)
7 Compensating magnet
8 Helium supply for 7
9 Muon chambers
10 Instrumented iron yoke
11 Forward muon toroid
12 SPACAL and Backward DC
13 Plug calorimeter
14 Concrete shielding
15 Liquid argon cryostat
16 H1 coordinate system

Figure 2.2: *An isometric view of the H1 detector which has a size of* $\sim 12 \times 10 \times 15\ m^3$ *and a weight of* $\sim 2800\ t$. *The individual components are described in the text.*

- The FNC (**F**orward **N**eutron **C**alorimeter), figure 2.4, section 2.5
- the luminosity system, figure 2.6
- the tracking system, figure 2.5

The numbers, given in boxes, are related to the legend of figure 2.2.

2.3 The Calorimeters

A calorimeter is designed to measure the energy and the position of a particle. In order to provide clear identification and precise measurements of both electromagnetically interacting and hadronically interacting particles, two kinds of calorimeters are implemented in the H1 detector: a particle, coming from the vertex, first passes through the electromagnetic calorimeters $\boxed{4}$, $\boxed{12}$, and then through the hadronic calorimeters $\boxed{5}$, $\boxed{12}$, $\boxed{13}$. This composition of the calorimeters is due to the fact that the hadronic interaction length is much longer than the radiation length of electromagnetically interacting particles in the same material. Electrons and photons are absorbed for the best part in the electromagnetic section whereas hadrons are very likely to interact first in the hadronic part.

2.3.1 The Liquid Argon Calorimeter

The Liquid Argon sampling calorimeter is the largest calorimeter of the H1 detector and covers the forward and central region around the interaction point. It consists of an electromagnetic $\boxed{4}$ and a hadronic part $\boxed{5}$. Both parts are embedded in liquid Argon that is kept at a temperature of $-182°$C by a cryostat. The electromagnetic part consists of layers of liquid argon as the active material separated by lead plates. The thickness of the electromagnetic Liquid Argon calorimeter varies between 20 and 30 radiation lengths. The energy resolution of the Liquid Argon electromagnetic section is $\sigma(E)/E = 12\%/\sqrt{E/\mathrm{GeV}} \oplus 1\%$ [3].

The total thickness of the hadronic Liquid Argon calorimeter, consisting of stainless steel absorber plates, corresponds to 4.5 - 8 hadronic interaction lengths. The granularity is coarser than in the electromagnetic part and the energy resolution is $\sigma(E)/E = 50\%/\sqrt{E/\mathrm{GeV}} \oplus 2\%$.

2.3.2 The Plug Calorimeter

The Plug sampling calorimeter $\boxed{13}$ consists of nine copper absorber plates interleaved with 8 sensitive layers of large area silicon detectors. It is utilized to close the gap between the beam pipe and the Liquid Argon in order to minimize losses of particles leaving the detector in the forward direction

[3] The sign $\oplus$ means: $a \oplus b = \sqrt{a^2 + b^2}$.

2.3.3 The Muon System

In the central region the calorimeters and tracking devices are enclosed by a superconducting coil $\boxed{6}$, generating a magnetic field of 1.2 T. A 2000 t heavy iron yoke $\boxed{10}$ surrounds the total H1 detector and serves as a return yoke for the magnetic flux. It is interleaved with slits equipped with muon detectors. They render the possibility to detect muons with energies higher than 1.5 GeV and they also serve as tail catchers for hadronic showers that are not completely absorbed in the hadronic calorimeters.

Another muon spectrometer is situated in the forward region consisting of drift chamber planes $\boxed{9}$ mounted on either side of the toroidal magnet $\boxed{11}$.

2.4 The Spacal

The Spacal (figure 2.3) covers part of the backward region of the H1 detector, namely the azimuth angular range $153° \leq \theta \leq 178°$ which corresponds to a rapidity (equation (1.11)) range of $-3.5 \leq y \leq -1.4$ for pions. The Spacal is a lead-scintillating fibre calorimeter

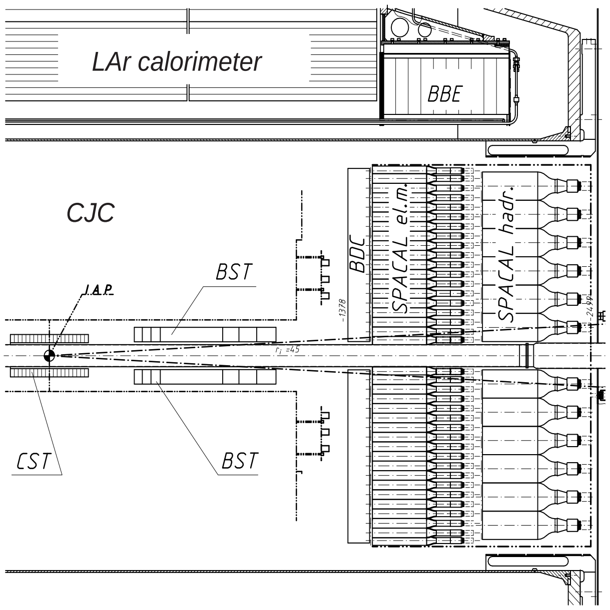

Figure 2.3: *A side view of the backward region of the H1 detector*

called spaghetti-type calorimeter. Bunches of fibres are read out by a photomultiplier tube, characterized by their low noise level. The Spacal consists of an electromagnetic and a hadronic section of equal size. The electromagnetic section is segmented into 1192 cells, and has a depth corresponding to 27 radiation lengths with a Molière radius[4] of 25.5 mm. This ensures a good spatial resolution. The hadronic section, consisting of 128 cells, has a depth of one hadronic interaction length. The lead-to-fibre ratio is higher than in the electromagnetic section, and the geometrical cross section of the cells is larger. A detailed description can be found in [APP96, APP97, NIC96]. The energy resolution of the electromagnetic Spacal section is:

$$\frac{\sigma(E)}{E} = \frac{7.5\%}{\sqrt{E/GeV}} \oplus 0.01, \tag{2.2}$$

where E is the energy deposited in the Spacal by an electromagnetically interacting particle. The spatial resolution is of the order of a few millimeters which corresponds to an angular resolution better than 2.5 mrad.

The uncertainty of the absolute energy scale in the energy range from 0.2 GeV to 10 GeV is known to be 4%, while for energies beyond 10 GeV the precision is on the 1% level.

The Spacal is part of the trigger and provides time-of-flight information. The time resolution of 2 ns allows one to define a time window in which particles from the ep-interaction are expected to hit the Spacal.

2.5 The Forward Neutron Calorimeter

The Forward Neutron Calorimeter (FNC) located at $z = +107$ m from the interaction point in the HERA tunnel detects high-energy neutrons which are produced at very low scattering angles of $\theta \lesssim 0.6$ mrad. In figure 2.4, the position of the FNC with respect to the beam

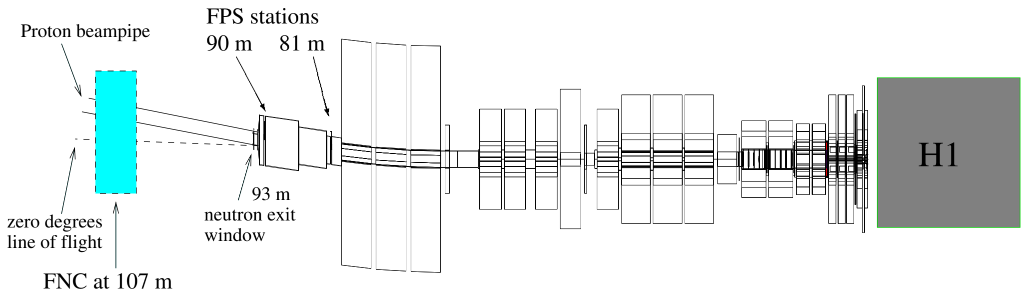

Figure 2.4: *Sketch of the HERA forward beam line including FNC and FPS. The position of the FNC and the two vertical roman pot stations are shown. H1 and the magnets of the proton beam optics are indicated*

pipe is shown. The FNC is a lead-scintillating fibre calorimeter consisting of interleaved layers of 2 m long lead strips and longitudinally aligned scintillating fibres. This kind of

[4]Molière radius R_M: approximately 99 % of the energy is contained inside the cylinder with a radius of $3.5R_M$

construction is called a spaghetti-type calorimeter (see Spacal 2.4). It has a depth of 9.5 hadronic interaction lengths, and a energy resolution [MET98]:

$$\frac{\sigma(E)}{E} \approx 20\%, \tag{2.3}$$

for neutron energies between 300 GeV and 920 GeV. The energy dependence of the spatial resolution of the FNC is given by [NUN99]:

$$\sigma_{xy}(E) = \left(\frac{5.13 \pm 0.81}{\sqrt{E/\mathrm{GeV}}} + (0.22 \pm 0.07) \right) \text{ cm.} \tag{2.4}$$

Charged particles can be vetoed by two segmented hodoscopes which are placed in front of the calorimeter. A tail catcher behind the calorimeter can measure the energy leakage.

Leading neutrons which are produced at the nominal interaction point and scattered under very low angles move along the beam line and leave the beam pipe at $z = 93$ m through an exit window to reach the FNC. The apertures of the proton beam line (bending and focusing magnets), located between the interaction point and the neutron calorimeter, are mainly responsible for the limitation of the acceptance of the FNC for detecting neutrons [NUN96]. The acceptance is $\sim 90\%$ for scattering angles of $\theta \lesssim 0.1$ mrad and decreases smoothly up to the highest detectable scattering angles of approximately 0.6 mrad. Further information about the FNC and its acceptance region can be found in [NUN96], [NUN99], [MET98] and in section 5.5.

2.6 The Central Tracking System

The H1 tracking system comprises three major devices, the forward, central and backward trackers. The central tracking system of the H1 detector consists of (starting from the interaction point and proceeding outwards):

- CIP (**C**entral **I**nner **P**roportional Chamber)
- CIZ (**C**entral **I**nner **Z**-Chamber)
- CJC1 (**C**entral **J**et **C**hamber **1**)
- COZ (**C**entral **O**uter **Z**-Chamber)
- COP (**C**entral **O**uter **P**roportional Chamber)
- CJC2 (**C**entral **J**et **C**hamber **2**)

For charged particles, the track curvature allows one to measure the particles' momenta. Since the velocity of the particles can be determined via the Bethe-Bloch equation [BET30] [BLO33], particles may be identified by measuring the specific energy loss dE/dx. In addition, the vertex of the interaction can be gained from the tracks. The forward tracking system covers the polar angular range θ from 5° to 25°, the central one from 15° to 165° and the backward drift chambers (BDC) extends the angular measurement over the range

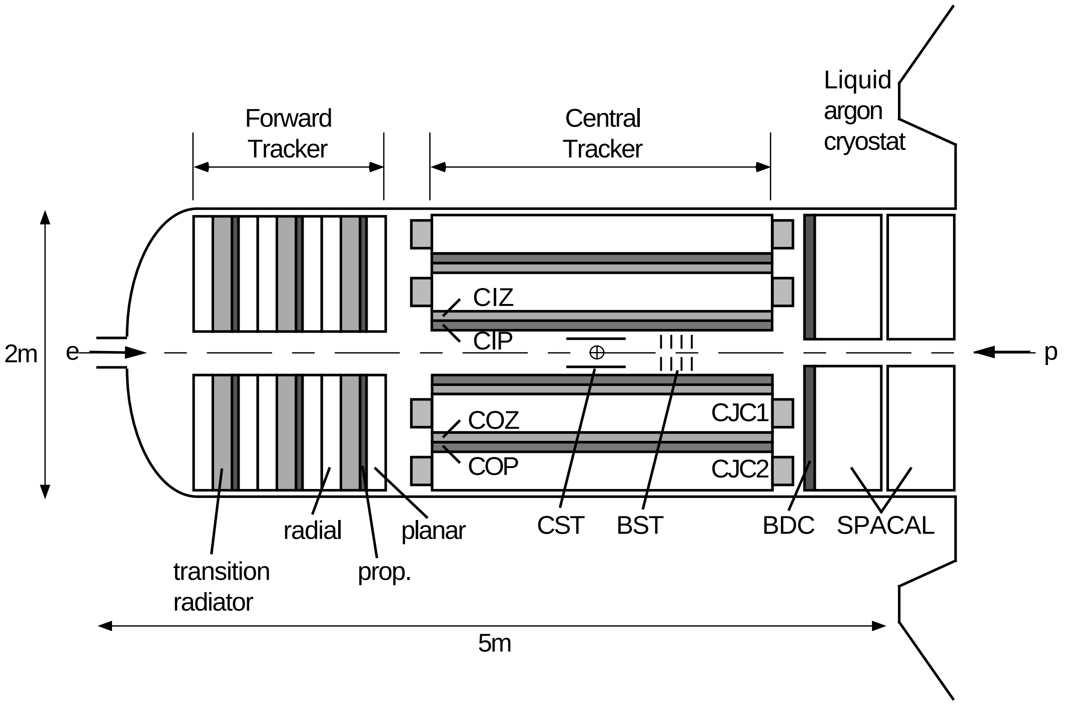

Figure 2.5: *A side view of the H1 tracking system*

155° to 178°. Figure 2.5 shows the complete tracking system from a side view. The central proportional chambers CIP and COP are Multi-Wire Proportional Chambers (MWPC) and provide fast signals for the first trigger level. The track reconstruction in the central region is based on the large concentric drift chambers CJC1 and CJC2. The spatial accuracy in the $r\phi$-plane is 170 μm. The determination of the z-coordinate of the particles can be improved with the help of the central (inner and outer) z-chambers CIZ and COZ, which leads to a resolution of $\sigma_z = 0.26$ mm. The Backward Drift Chamber BDC, directly mounted in front of the Spacal (2.4), measures backward scattered charged particles.

The present analysis uses the tracking detectors, from which the vertex finding is based, as a veto for particle activity in the central region of the H1 detector.

2.7 The Time-Of-Flight (TOF) System

The time of flight (TOF) system consists of scintillators which are situated at several positions along the beam pipe. At $z = +7$ m the forward TOF and at $z = +5.3$ m the Plug TOF can be found, the VLQ TOF (see section 3.5) is located behind the VLQ calorimeter at z = -3.2 m and the Veto Walls at z = -8.1 m and z = -6.5 m.

The TOF system is designed to reject proton beam induced background by defining a time window in which particles from an ep reaction at the nominal interaction vertex are expected to cross the scintillators (see also 3.5).

2.8 The Luminosity System

The event rate $\dot{N}$ is proportional to the interaction cross section σ, and the luminosity $\mathcal{L}$ is defined as the factor of proportionality:

$$\dot{N} = \mathcal{L}\sigma. \tag{2.5}$$

If two bunches, colliding with frequency f, contain n_1 and n_2 particles, then the luminosity is:

$$\mathcal{L} = f\frac{n_1 n_2}{4\pi\sigma_x\sigma_y} \tag{2.6}$$

where σ_x and σ_y are the standard deviations of the approximated Gaussian transverse beam profiles in the x and y directions perpendicular to the beam pipe. Equation (2.6) shows that the luminosity $\mathcal{L}$ is a machine dependent variable. From equation (2.5) it is clear that

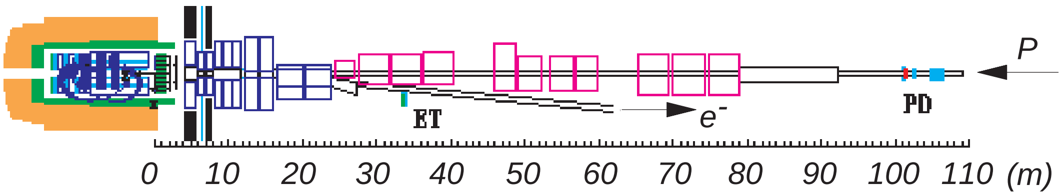

Figure 2.6: *The luminosity system of H1*

an exact measurement of the luminosity $\mathcal{L}$ is of prime importance for the determination of cross sections. On the other hand, the luminosity can be calculated via equation (2.5) by measuring the rate $\dot{N}$ of a well-known cross section. For this purpose at HERA the bremsstrahlung or Bethe-Heitler process $ep \to e\gamma p$ is used whose cross section is known with high precision from QED[5] calculations.

The integrated luminosity is defined as the time integral

$$L = \int \mathcal{L}(t)\, dt. \tag{2.7}$$

Figure 2.6 shows the luminosity system of H1, consisting of an electron tagger[6] (ET) at $z = -33.4$ m and a photon detector (PD) at $z = -102.9$ m .

The electron tagger is a crystal Cherenkov calorimeter with 49 channels, a total transverse size of 15.4×15.4 cm and a depth of 20 cm according to 22 radiation lengths.

The photon detector is also a crystal Cherenkov calorimeter with 29 channels, a total transverse size of 10×10 cm and the same depth as the electron tagger, 20 cm.

[5]QED: Quantum Electro Dynamics

[6]The expression “electron tagger” is used here as a synonym for the expression “electron detector”. “Electron tagger” denotes that the detected electron provides energy information about the virtual photon.

The electron tagger works as a magnetic spectrometer, detecting only those electrons within an energy range corresponding to roughly $0.3 \lesssim y \lesssim 0.7$ (see equation (1.6)) and $Q^2 < 0.01$ GeV^2 (see equation (1.3)).

There are further electron taggers at $z = -7$ m, $z = -8$ m, and $z = -44$ m covering the subsequent energy ranges. This analysis focuses on the electron detector at $z = -33.4$ m in order to detect the scattered electron.

2.9 The Triggering System of H1

The task of the trigger system is to select relevant ep-interaction events and to reject background. The background at HERA originates from proton- and electron-gas interaction in the beam pipe, synchrotron radiation from the electron beam, and stray protons hitting the beam pipe or other materials producing particle showers. Further background sources are muons from cosmic radiation and finally so called Halo muons which fly in parallel with the proton bunches.

The cross sections of physics processes vary by orders of magnitude and are directly reflected in the respective rates. At design luminosity ($\mathcal{L} = 1.5 \cdot 10^{31} cm^{-2} s^{-1}$), the lowest rates for charged current interactions start with a few events per hour, deep inelastic scattering occurs at a few events per second and photoproduction reaches up to 30 Hz; on the other hand, beam gas interactions occur roughly 50000 times per second.

This implies that a trigger must provide both a quick and a reliable decision. A compromise between these two requirements, on the one hand quickness, in order to minimize the dead-time, and on the other hand thorough information, is best matched by a set of 5 trigger levels at the H1 experiment.

trigger level L1: The first trigger level provides a decision after 2.5 μs. Indeed the time interval between two bunch crossings is 96 ns, corresponding to a frequency of 10.4 MHz. The full information about the 26 bunch crossings are stored in a pipeline while the decision is made. This ensures that the trigger level L1 runs dead-time free, which is important since the probability for an ep interaction is of the order of 10^{-3} per bunch.

At this level most subdetectors of H1 provide simple, but fast, information which is used by the trigger. A combination of different requirements on these information (trigger elements) is called a subtrigger. An event is accepted if at least one of the 128 subtriggers at H1 reaches a positive decision. In addition, every subtrigger can be furnished with a so called prescale factor to downscale the triggering rate. A prescale factor k means that only one event is accepted out of k events that are triggered. In this analysis the trigger elements from the eTAG, the FNC and the VLQ are combined into two subtriggers (see section 5.1.1 and 5.1.2).

If an event accepted, the pipeline is stopped and the trigger level L2 is started.

trigger level L2: The latency on level 2 is 20 μs. A larger number of detector signal correlations is evaluated making use of a neural network and a complex topological correlator. An accepted event causes the readout of the complete detector and data are copied from the pipelines.

trigger level L3: This level is not implemented.

trigger level L4: The level 4 trigger is composed of a processor farm, and the full H1 detector raw data (RAW) is available for reconstruction ($\approx$ 40 kByte per event). An asynchronous software trigger uses the full intrinsic detector information for the decision making algorithms. Besides the rejection of events, identified as background, the level 4 filter farm serves as a monitoring tool for data taking and for the online calibration of individual components.

trigger level L5: This level is not a real trigger in the sense of rejecting an event irrevocably, it is an offline operating trigger that fully reconstructs the events and classifies them according to their physics signature. All data are stored on a magnetic tape, called POT[7] (120 kByte per event). To allow for a fast access, the data is compressed to 6 kByte per event and stored on hard disk drives, so-called DST[8], the starting point for each data analysis.

[7]POT: Physics Output Tape
[8]DST: Data Summary Tape

Chapter 3

The VLQ Spectrometer

3.1 The Physical Motivation

Figure 3.1 shows the $\gamma^* p$-cross-section as a function of Q^2 with the $\gamma^* p$-centre of mass energy W as a parameter. The process

$$\gamma^* + p \rightarrow X \tag{3.1}$$

is considered. The depicted measurement was made by the H1 collaboration before the VLQ spectrometer was available. As figure 3.2 demonstrates, the insertion of the VLQ

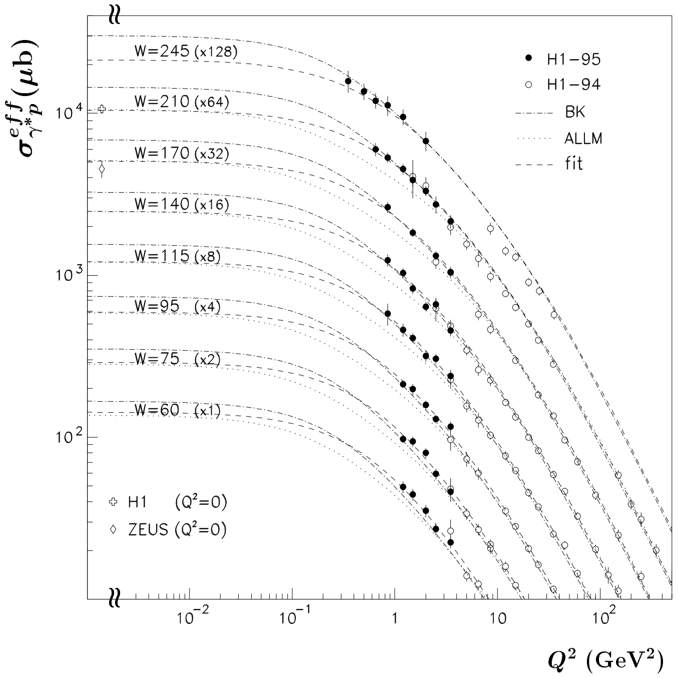

Figure 3.1: *The photon-proton cross section as a function of Q^2 parameterized by the invariant mass W. The measurement was made by H1 previous to the installation of the VLQ spectrometer. The curves are scaled with the given factors in brackets [H1D96].*

spectrometer allows for the extension of measurements to phase space regions not available previously. On the one hand, the measured points of the cross sections in figure 3.1 were determined with the aid of the electron taggers for $Q^2 < 0.01$ GeV^2 (see figure 3.2), so-called “tagged photoproduction”. On the other hand, the cross sections in figure 3.1 were measured for values of $Q^2 > 1$ GeV^2 with the electron detected in the Spacal or in the Liquid Argon Calorimeter. The Spacal is sensitive to the Q^2-region between 1 GeV^2 and 10^2 GeV^2, the Q^2 region from 10^2 GeV^2 to 10^5 GeV^2 is covered by the Liquid Argon Calorimeter. The VLQ spectrometer closes the gap in Q^2 from 0.01 GeV^2 to 1 GeV^2.

In the presented analysis the VLQ is used to detect photons from a pion decay, however. The VLQ denotes an enlargement of the phase space compared to the Spacal especially, since the considered process has a steep t distribution and the highest activity is expected close to the beam pipe. Furthermore the VLQ has a high spatial resolution.

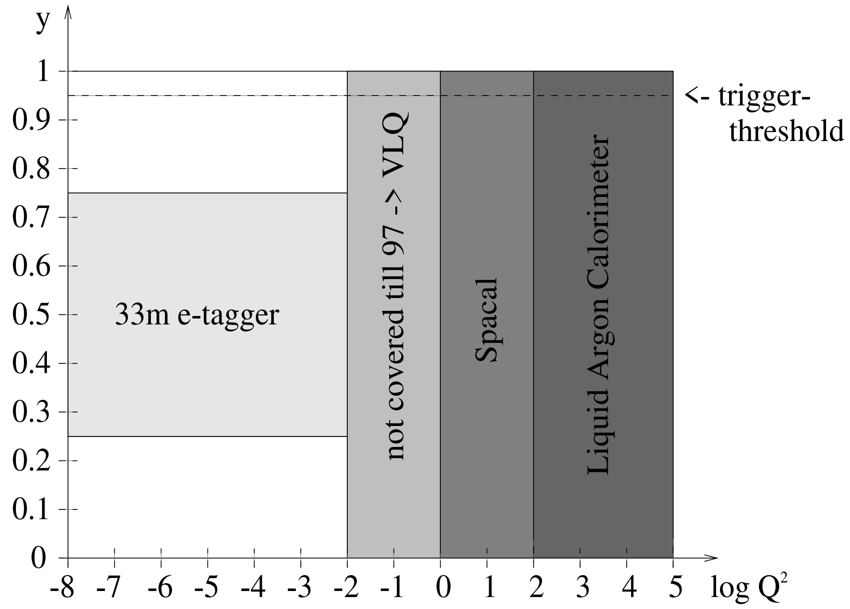

Figure 3.2: *The acceptance regions of the different subdetectors of the H1 detector are illustrated in the y - $\log_{10} Q^2$ plane. Compared to the other components the y-acceptance of the electron tagger is restricted as a consequence of its smaller acceptance region for the energy of the scattered electron (see section 2.8).*

3.2 The Setup of the VLQ Spectrometer

The VLQ spectrometer [H1D96] consists of four individual components. These are

- the tracker
- the calorimeter
- the **T**ime **O**f **F**light system (TOF)

- the moving mechanics.

In the following, these components are described in greater detail. As mentioned above, the VLQ spectrometer is designed to cover the region of Q^2 between 10^{-2} GeV^2 and 1 GeV^2. From equation (1.3) it is clear that these Q^2-values imply very small scattering angles of the electron, which correspond to $\theta \approx 180°$ in the H1 coordinate system. Therefore, the VLQ-Calorimeter is mounted nearby the beam pipe in the backward direction. Figure 3.3 shows a profile of the H1 detector. The location of the VLQ, denoted by the arrows, is

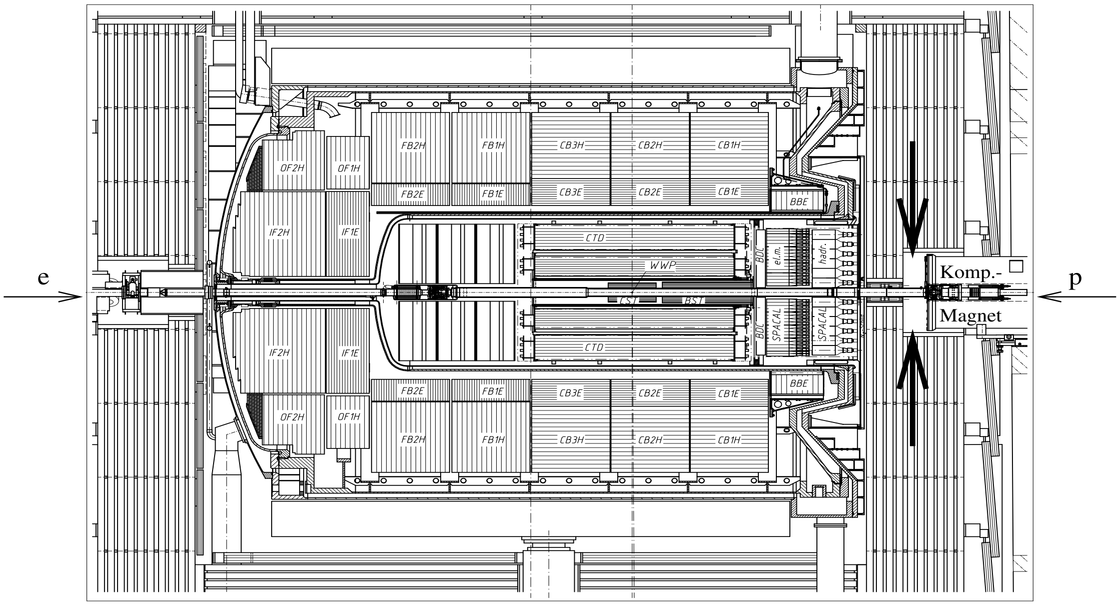

Figure 3.3: *Profile through the H1 detector. The arrows show the mounting position of the VLQ-Spectrometer. The protons come from the right hand side and the electrons from the left hand side.*

situated between the compensation magnets and the return yoke (see also figure 2.2). The electromagnetic and hadronic calorimeters of the Spacal are shown in the same figure 3.3. The electromagnetic Spacal, covering the polar angular range $152° \leq \theta \leq 177.5°$, exactly follows the polar angular acceptance region of the VLQ spectrometer of $177.3° \leq \theta \leq 179.4°$, yet the VLQ is not symmetric in ϕ. Unfortunately, the acceptance region of the VLQ is shadowed by the Spacal Insert, which cannot be used for the analysis, so that the polar angular range is limited to values larger than $178.3°$ (see also figure 5.3).

Figure 3.4 gives a closer look at the VLQ spectrometer. On the right hand side, the cylindric compensation magnet is shown, to which the spectrometer is attached, as well as the iron return yoke for the magnetic field. The exact arrangement of the components (tracker, calorimeter, TOF, and moving mechanics) can easily be identified. The VLQ spectrometer consists of two identical modules mounted on the top and the bottom of the beam pipe. In order to minimize dead material in which the particles must travel through, the beam pipe is decreased conically in front of the VLQ. The reduced diameter of 6 cm allows measurements of scattered particles under very small angles.

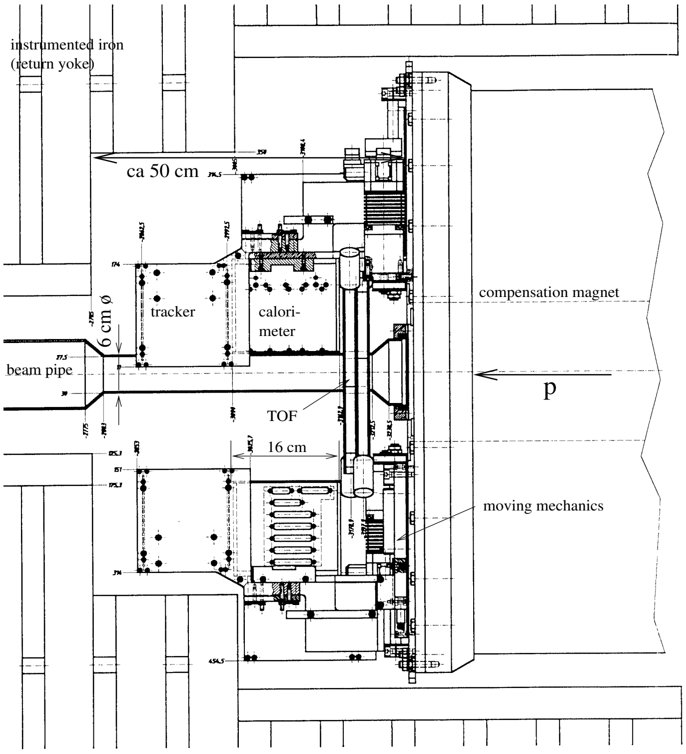

Figure 3.4: *A more detailed view of the VLQ's position at the rear end of the H1 detector. On the right hand side, the compensation magnet is shown, to which the spectrometer is attached.*

3.3 The Tracker

Starting from the vertex and proceeding outwards, the tracker is the first component of the VLQ spectrometer that a scattered particle passes through. The tracker consists of two double layers of silicon strip detectors separated by 13 cm. The anodes are partitioned in stripes with a width of 62.5 μm, which results in a resolution of 18 μm.

The tracker has two main tasks: First, it performs a precise measurement of the scattering angle of the electron, and secondly, it allows for a determination of the z-vertex. This can be done by fitting a straight line through the two impact points and extrapolating this line to the point of intersection with the z-axis, which gives the z-vertex.

The present analysis does not make use of the tracker information.

3.4 The Calorimeter

The VLQ "Energy Projection" calorimeter follows the tracker in the $+z$-direction. Its task is to measure the energy, the x- and the y-coordinates of the impact points of electromagnetically interacting particles which enter the calorimeter. Thereby, an ambiguity of the track reconstruction can be eliminated by the redundant measurement of the calorimeter. Since the bremsstrahlung-spectrum almost becomes extinct at a few MeV and the calorimeter begins sensitivity only for energies above 2 GeV [NIX00], the calorimeter cannot resolve photons from synchrotron radiation.

The VLQ is an electromagnetic sampling calorimeter which is elaborated in the following.

The most important duty of an **electromagnetic** calorimeter is to measure the energy of electromagnetically interacting particles such as electrons and photons. The kind of interaction between the particle and the surrounding matter depends on the particle's charge. For charged particles (electrons) the dominate process, leading to an energy loss, is bremsstrahlung[1]. Neutral particles (photons) interact with matter via the photo effect, Compton effect and (e^+e^-)-pair-production, where pair-production is the dominant process for photon energies above a few MeV.

The VLQ **sampling** calorimeter is not homogeneous, but is made of scintillator (active medium) and tungsten (passive medium) plates (figure 3.5). The calorimeter is forced to be very compact and at the same time represent a large number of radiation lengths. Having a high atomic number ($Z = 74$) and a large density ($\rho = 19.3 g/cm^3$), tungsten is well suited for the absorber material. The VLQ differs from ordinary sandwich-calorimeters,

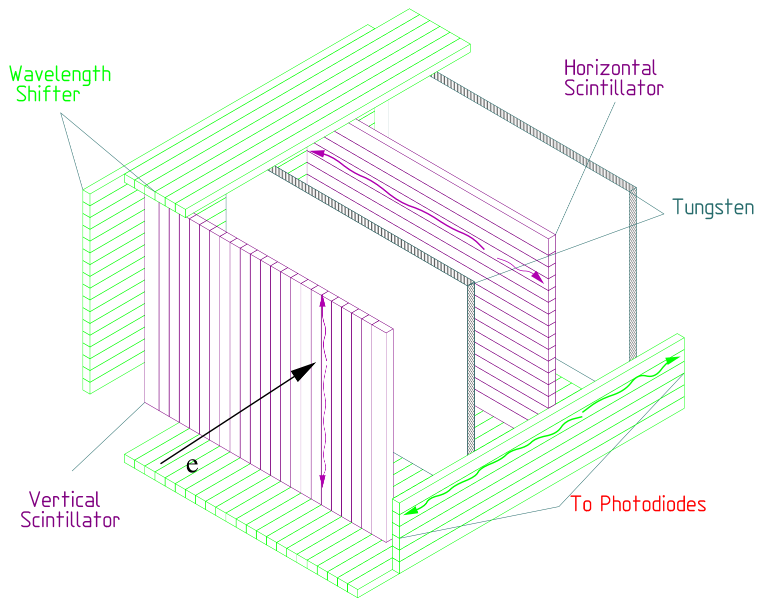

Figure 3.5: *Schematic exploded view of the VLQ calorimeter. The active medium consists of scintillator strips, oriented perpendicular to the strips in the neighbouring layer. The light originating in the scintillators is absorbed by the wavelength shifters, guided to the abutting faces where it can be detected by photodiodes. [H1D96].*

as the longitudinal structure of the calorimeter consists of alternating layers of horizontal scintillator bars, tungsten absorber plates and vertical scintillator bars. Therefore the strips oriented in the x-direction measure the y-coordinate and in the same manner the strips oriented in the y-direction measure the x-coordinate. White paper wrapped around the

[1] A further process is ionisation of atoms in the detector material which can be described by the Bethe-Bloch-formula [BET30] [BLO33].

strips provides for a suppression of optical cross-talk. This renders the possibility to verify the spatial position of electromagnetically interacting particles without making use of the tracker. Because this analysis does not make use of the tracker, this last point is important.

The blue light from the scintillators is proportional to the energy of the particle shower and is guided to both ends of the scintillators making use of total reflection. At the ends, wavelength shifters, arranged on the top, bottom, left and right surfaces of the calorimeter stack, collect the light from the scintillators. All identically oriented scintillators deposit their light in the same wavelength shifter at their respective ends. The wavelength shifters absorb the blue light and remit it in the green range. Photodiode arrays are glued to the end surfaces of the wavelength shifters and convert the light signal into electric charges. The charge-signals from the two ends are added electronically which results in 84 readout channels per module. A summary of the most important characteristics of the VLQ calorimeter is given in table 3.1, and the structure of the VLQ is shown in figure 3.6.

parameter	value
lengths	129.5 mm
width	124 mm
height	94 mm
number of absorber layers	23
radiation length in the absorber	3.9 mm
radiation length in the scintillator material	424 mm
depth in radiation lengths	15.3
Molière radius	1.25 cm
number of wavelength shifters per module	84
number of photodiodes per module	168

Table 3.1: *Characteristics of the VLQ calorimeter [STE98].*

The energy and spatial resolution of the VLQ calorimeter were determined with the aid of a test beam of electrons and positrons with energies between 1 and 6 GeV. The energy resolution was found to be [STE98]:

$$\frac{\sigma(E)}{E} = \sqrt{\left(\frac{19\% \pm 6\%}{\sqrt{E/\mathrm{GeV}}}\right)^2 + (6.4\% \pm 3\%)^2 + \left(\frac{23.4\% \pm 0.9\%}{E/\mathrm{GeV}}\right)^2}. \tag{3.2}$$

There are three contributions:

- **sampling term**: proportional to $\frac{1}{\sqrt{E}}$. Its characteristic dependence on the energy results from the Poissonian distribution of the events.

- **constant term**: Due to the finite dimensions, shower particles can leak from the calorimeter leading to an energy loss proportional to E.

- **noise term**: proportional to $\frac{1}{E}$. It comes from the electronic noise, which is independent of the energy.

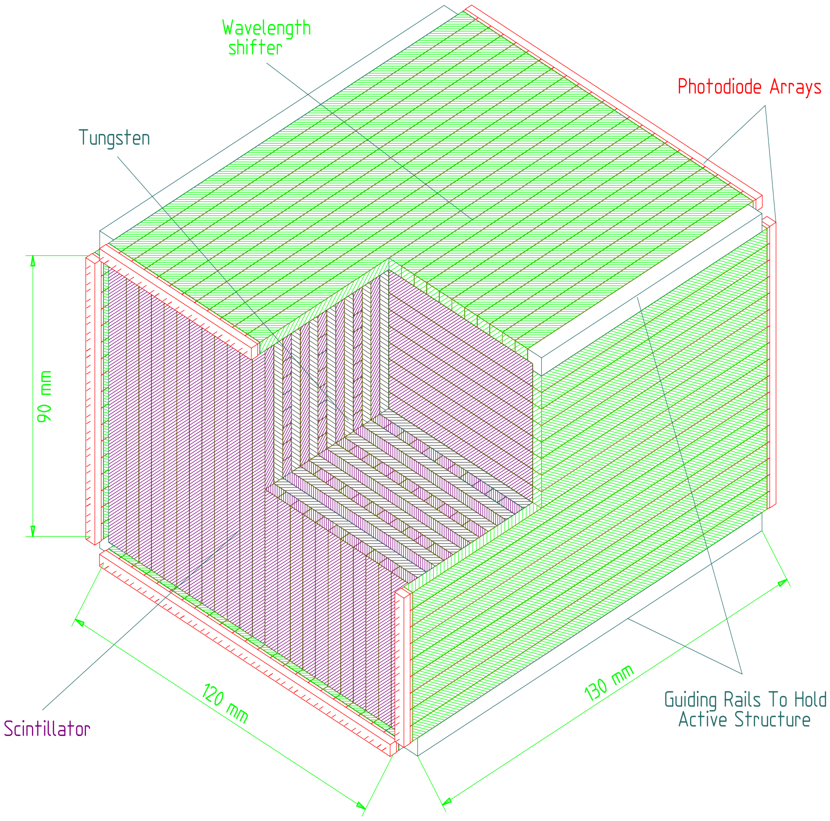

Figure 3.6: *The structure of the VLQ-Calorimeter [H1D96].*

An energy calibration of the VLQ calorimeter with kinematic peak electrons was performed [NIE00] and applied to the data.

The spatial resolution of the VLQ calorimeter is also energy dependent [STE98]:

$$\Delta x = \frac{(2.06 \pm 0.02)\mathrm{mm}}{\sqrt{E/\mathrm{GeV}}}. \tag{3.3}$$

It improves with rising energy and is on the 1 mm level for the photons, resolved by the calorimeter.

3.4.1 The Energy and Position Reconstruction of the VLQ

The event reconstruction is based on the energies of all 2×84 channels, corrected for the pedestal value of the respective channel. The pedestal value is the mean noise level of a channel which averages 35 MeV. The corrected energies of the 84 channels of a module are arrayed corresponding to the 4 projections of a module. The event is only reconstructed if the energy of at least one channel of a module exceeds the triple mean noise level. If an event fulfils this requirement, it is scanned for single diodes, which occur in approximately 60% of all events. *Single diode events* are signals with a particle directly hitting a photodiode and thus faking a huge energy deposition. Channels contaminated with a single diode are excluded. Subsequently, the actual reconstruction of an electromagnetic shower begins. Spatially contiguous energy depositions of the projections are assigned to be an electromagnetic shower, called a cluster. All possible compositions of the different projections are built as is shown in figure 3.7 for the relevant number of particles in one module.

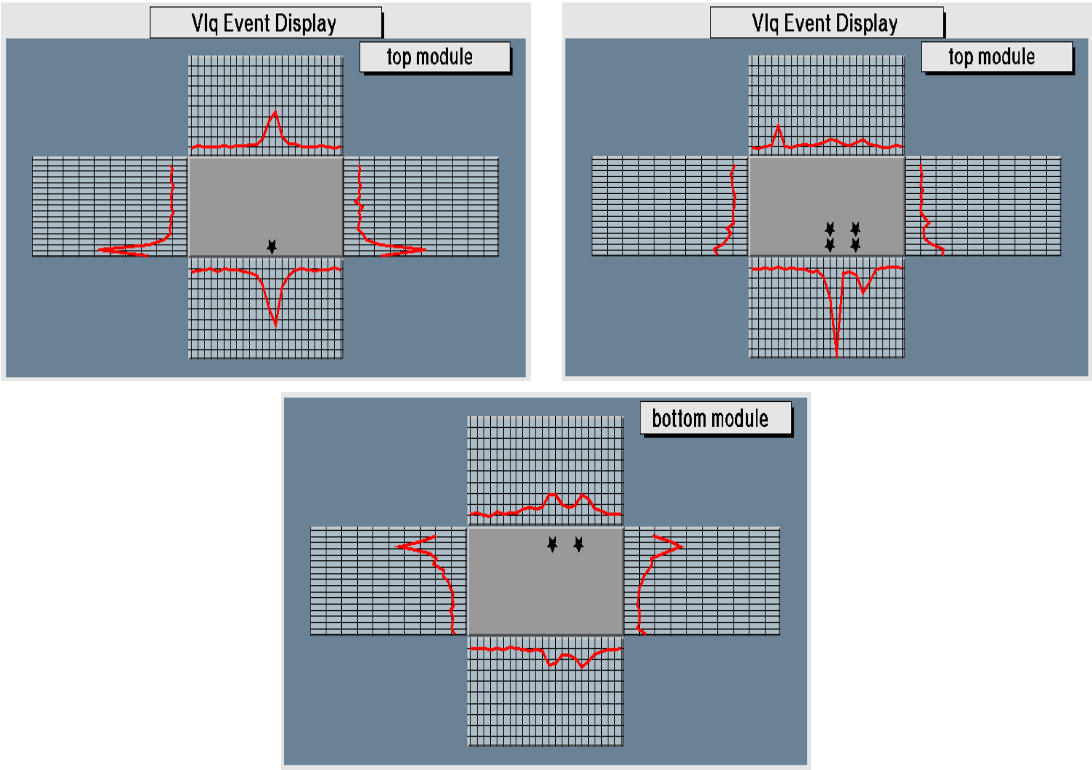

Figure 3.7: *Three examples from the data sample investigated: The top left event display shows the energy depositions of one electromagnetically interacting particle. Thus, one cluster is reconstructed where the intercept point of the four energy projections lies. The second display (top right) shows the case for two particles. There is an ambiguity which of the four reconstructed clusters belong to the two particles. In this case, according to the magnitude of the energy projections, the upper right and the lower left point of interception are identified as the two clusters. In addition, a single diode signal can be seen in the upper projection. Since there is no energy projection on the opposite side, no cluster is associated with it. The bottom display represents the degenerate case of the second picture where the two particles hit the VLQ in a (horizontal or vertical) plane that contains two opposite channels. By splitting the energies of the degenerate projection proportional to the two projections that are not degenerate, this case is also treated as four clusters.*

The energy is calculated by summing over all channels i belonging to a cluster:

$$E = \sum_i E_i. \tag{3.4}$$

Electromagnetic showers have an energy profile that can be described by two exponential functions. On calculating the centre of gravity of the clusters, this behaviour is accounted for by a logarithmic weighting of the channel energies. The x (respectively, y) coordinate of the cluster is determined by:

$$x = \frac{\sum_i w_i x_i}{\sum_i w_i}, \tag{3.5}$$

with

$$w_i = \begin{cases} W_0 + \ln\left(\frac{E_i}{E}\right) & , \quad \left(\frac{E_i}{E}\right) > e^{-W_0} \\ 0 & , \quad \left(\frac{E_i}{E}\right) \leq e^{-W_0} \end{cases} \tag{3.6}$$

where W_0 is a free parameter that was adjusted to be 3 [MEY00]. The z coordinate of all clusters is assumed to coincide with the front side of the calorimeter at

$$z = -301.7 \text{ cm}. \tag{3.7}$$

3.4.2 The VLQ Calorimeter Trigger

The VLQ trigger is designed to recognize events with energy deposits in the calorimeter. The trigger fires when a certain threshold is exceeded and the energy deposition takes place within the HERA bunch crossing time. Analog sums of signals from different calorimeter channels in the vertical projections are built forming so-called trigger windows. In order to have a sharp trigger threshold, it is desirable that only the particle's signal contributes to the trigger decision, otherwise channels consisting of coherent noise soften the threshold.

Signals of 9 subsequent channels are combined into a trigger element. In order not to lose energy of a particle that hits the end of such an area, neighbouring elements overlap by 6 channels, which are called "Sliding Windows". The overlap is chosen in such a way that the 6 channels (equals 3 cm) comprise the greatest part of the energy according to the small Molière radius of 1.25 cm. As mentioned above already, the upper 6 channels out of the 18 vertical calorimeter channels are not included in the trigger logic because this area is shaded by the Spacal Insert. Thus the remaining 12 channels are divided into 4 trigger elements for each module.

A discriminator verifies whether the signal of a trigger element exceeds a threshold and compares opposite trigger windows. This is done to exclude single diode events that appear most likely only in one projection. Three different energy thresholds exist for the VLQ: NOISE (6 GeV), LOW (8.5 GeV) and HIGH (10 GeV). If the sum of the energies in one trigger channel exceeds one of these thresholds, then the respective trigger element is set. The 8 trigger elements are sent to the **C**entral **T**rigger **L**ogic (CTL) of the H1 detector and by logic operations Level 1 subtriggers can be built.

3.5 The VLQ Time-Of-Flight (TOF) System

The TOF system directly follows the calorimeter in the $+z$-direction shown in figure 3.4. Its purpose is to suppress events from proton induced background. This background emerges from inelastic interactions of the proton beam with rest gas atoms in the beam pipe or with the wall of the beam pipe. These events can take place at any location within the HERA ring, but particles from proton induced background hit the H1 detector always coming from the proton direction, as the proton transfers momentum to these particles (comparatively at rest). This matter of fact is utilized by the TOF detector: It measures the time difference between the electron proton collision and the signal from particles hitting the TOF system. Particles from *ep*-collisions arrive later than particles from proton induced background with respect to the bunch crossing time. Thus the TOF system works for signals occurring too early. In contrast, background coming from the electron direction cannot be excluded; photons from synchrotron radiation may also be late with respect to the bunch crossing time and therefore the TOF detector cannot veto them.

3.6 The Moving Mechanics

The moving mechanics shown in figure 3.4 was built to protect the calorimeter and the tracker against radiation damage. In case of bad background conditions, caused by synchrotron radiation or unstable beams, the VLQ spectrometer can be retracted away from its operational position close to the beam pipe, as displayed in figure 3.4: the upper module is in the nominal position of data-taking whereas the lower module is retracted.

The position of the VLQ can be determined with a precision of about 1 μm, making use of the Bethe-Heitler process which is well known.

Chapter 4

Monte Carlo Simulation

The physics processes studied in the presented analysis cannot be observed directly, but only by the signature of the final state left in the components of the H1 detector. An understanding of the detector response necessitates a detailed simulation of the interaction between final state particles and detector material. This allows for the determination of acceptances and – in case this cannot be concluded from data – detector efficiencies.

The simulation is calculated by means of the Monte Carlo method. The Monte Carlo method, based on the theorem of Monte Carlo [PRE92], uses random numbers to perform numerical calculations. The process of simulation can be subdivided into four parts:

Generation In a first step the Monte Carlo generators produce final state particles according to probabilities derived from a specific physics model. A large number of events is generated and the uncertainty of Monte Carlo predictions is generally proportional to the square-root of the number of generated events.

On this level all information about all particles produced are available: their four-momenta, masses, charges and the particles' mothers and daughters, if existent.

Detector Simulation Subsequently, a detailed simulation of the particles' way through the H1 detector and the interaction with the detector material is processed. This is realized by the program H1SIM [H1I89], which was assembled within the GEANT [GEA93] framework. A virtual copy of the full H1 detector is implemented therein, including the detailed geometry of the subdetectors and assigning matter-specific constants. The magnetic field as well as the generation of secondary particles and particle showers are considered. The simulation returns the impact points of the particle tracks and the energy depositions in the active material of the calorimeters. A detailed time-consuming version exists, describing the components in detail, and a simplified fast version with an energy shower parametrisation, H1FAST (see for example [SED00]), utilized in this analysis.

In section 5.5 a special treatment of the detector component FNC, not implemented in the official H1 detector simulation, but needed for this analysis, is presented.

Digitisation The digitalisation step simulates the response of the sensitive detector components, the effects of the electronic readout, digitalisation and electronic noise. The format of the created information is very close to the real raw data (RAW).

Reconstruction In the last step the generated and simulated events are reconstructed in the way described in section 2.9 and can be treated like real data (POT).

In this analysis the simulation procedure was applied on three different sets of data generated by $\mathbb{O}\mathbb{P}$IUM [KOR00], PYTHIA [SJO94] and DIFFVM [LIS99]. The acceptance of the electron tagger (see section 2.8) restricts events to the kinematic regions

$$0.3 \leq y \leq 0.7 \qquad \text{and} \qquad Q^2 < 0.01\ \text{GeV}^2, \tag{4.1}$$

so that only events fulfilling conditions 4.1 are generated.

DIFFVM is presented first since $\mathbb{O}\mathbb{P}$IUM is an extension of it and finally the general background generator PYTHIA is explained.

4.1 The DIFFVM Generator

DIFFVM produces special background processes which have almost the same final state as the signal (4.4): The diffractive production of vector mesons (VM). The DIFFVM generator [LIS99] produces vector mesons based on the Vector Meson Dominance model introduced in section 1.1.2 and depicted in figure 1.6. According to the Feynman-diagram in figure 1.6 in a first step the generator simulates the radiation of a virtual photon by the incoming electron. Subsequently, the fluctuation of the virtual photon into a virtual vector meson is performed on basis of the VMD. The real vector meson is produced by interaction with the Pomeron:

$$e + p \rightarrow e + VM + N^*. \tag{4.2}$$

The only relevant decay mode for background is the channel in which the VM decays into a pion and a photon:

$$VM \rightarrow \pi^0\gamma. \tag{4.3}$$

The two main contributions come from the ω and the ρ^0 mesons. Since the masses of the ω and the ρ^0 are almost equal only ω mesons with the decay mode (4.3) were generated.

4.2 The $\mathbb{O}\mathbb{P}$IUM Generator

In this analysis the process:

$$e + p \rightarrow e + \pi^0 + N^* \tag{4.4}$$

is investigated, where the incoming electron emits a virtual photon γ^*, from which a high-energetic pion is produced via γ^*-$\mathbb{O}$-fusion, and an excited proton is in the final state. Comparing figure 1.17 (a) with figure 1.6, this process is identical to the diffractive production of vector mesons (discussed in 4.1) where the Pomeron is replaced by the Odderon and the vector meson by a pseudoscalar, in particular the π^0. Thus $\mathbb{O}\mathbb{P}$IUM [KOR00] is an extension of the generator DIFFVM with a pion in the final state and the t-dependence calculated in

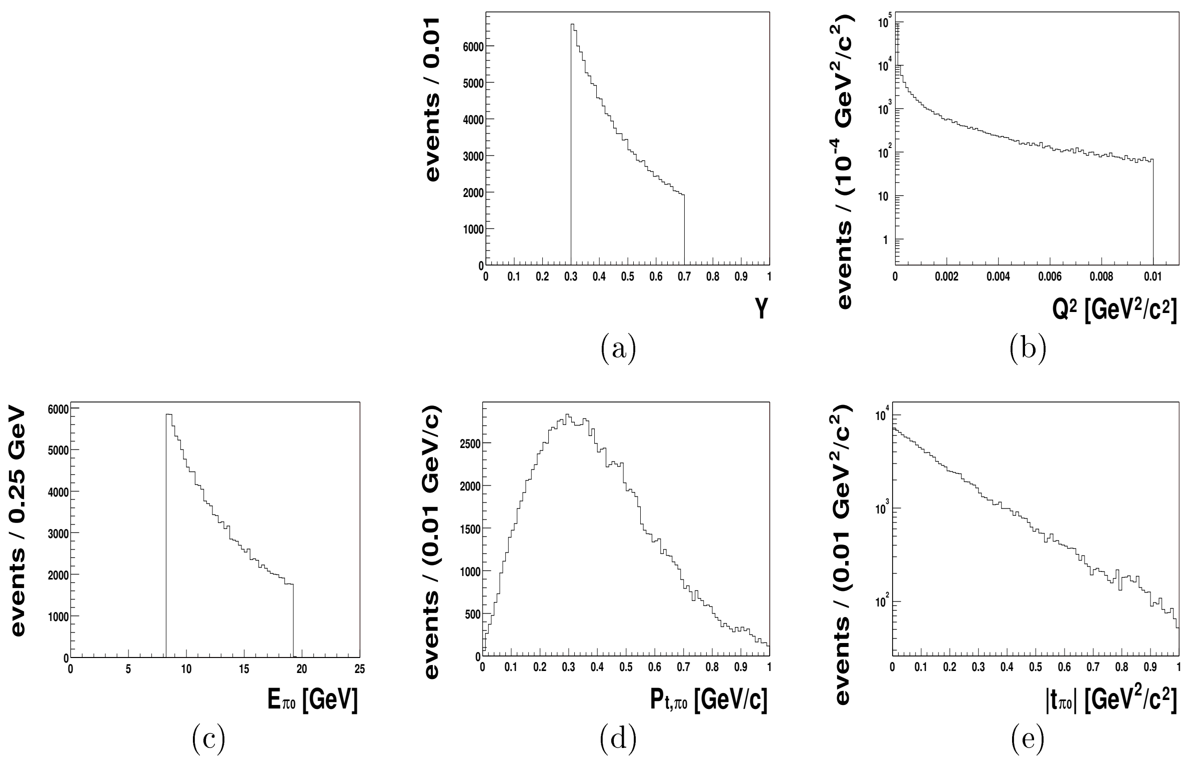

Figure 4.1: *Relevant generator distributions for $\mathbb{OP}$IUM: (a) y, (b) Q^2, (c) pion energy, (d) pion transverse momentum, (e) the transverse momentum squared which can be identified by the Mandelstam-variable t (see equation (1.8) and (5.20)) and can directly be compared with figure 1.18.*

the MSV [BER99a] as shown in figure 1.18. $\mathbb{OP}$IUM denotes **$\mathbb{O}$**dderon and **$\mathbb{P}$**omeron **I**nduced **U**nified **M**eson maker[1]. The relevant generator distributions are shown in figure 4.1.

$\mathbb{OP}$IUM describes neither the excitation nor the dissociation of the proton. Since the Odderon triggers (see section 5.1) applied for this analysis ask for the detection of a neutron in the FNC (see section 2.5), it is mandatory to simulate the proton final state on top of the processes implemented in $\mathbb{OP}$IUM.

4.2.1 The Treatment of the Nucleon Resonance N^*

In [BER99a] two possibilities, leading roughly to the same results, are discussed to treat the final state either as a free quark-diquark pair or as a nucleon resonance. The latter possibility is performed here. The break-up of the nucleon by Odderon exchange leads to negative parity, isoscalar final states, and for dynamical reasons the total angular momentum of the nucleon resonance is restricted to the allowed quantum numbers $I(J^P) = \frac{1}{2}(\frac{3}{2}^-), \frac{1}{2}(\frac{1}{2}^-)$. The only allowed nucleonic states are summarized in table 4.1 In order to simulate the **excitation** of the proton, it is important to know the probabilities for the different nucleon resonances. A

[1]Beside pseudoscalars, $\mathbb{OP}$IUM can also produce tensors such as f_2 and a_2 which are investigated in [CUB01] and [BER01], respectively.

m_{N^*} [MeV]	$I(J^P)$	$\Gamma_{p\to N^*}/\Gamma_{tot}$
1520	$\frac{1}{2}(\frac{3}{2}^-)$	0.45
1535	$\frac{1}{2}(\frac{1}{2}^-)$	0.45
1650	$\frac{1}{2}(\frac{1}{2}^-)$	0.05
1700	$\frac{1}{2}(\frac{3}{2}^-)$	0.05

Table 4.1: *Nucleon resonances allowed to occur in Odderon induced processes according to [BER99a] with masses m_{N^*} and quantum numbers [PDG00]. The last column gives the probability that an excited state N^* with the mass m_{N^*} is produced [DOS00].*

calculation in the MSV showed that the mass dependence of the proton excitation is steeper than the $1/m_{N^*}^2$ proportionality. The last column of table 4.1 gives the branching ratios used [DOS00].

At this point the excitation of the protons with the predicted t-distribution is modelled. The next step is the simulation of the **decay** of the excited nucleon state. In table 4.2 the three dominant decay modes are given which amount to 93 to 99% of all decay modes.

m_{N^*} [MeV]	$\Gamma_{N^*\to N\pi}/\Gamma_{tot}$	$\Gamma_{N^*\to N\pi\pi}/\Gamma_{tot}$	$\Gamma_{N^*\to N\eta}/\Gamma_{tot}$
1520	0.55	0.45	-
1535	0.48	0.07	0.45
1650	0.75	0.17	0.08
1700	0.10	0.90	-

Table 4.2: *The branching ratios for the three dominant decay modes, amounting to 93 to 99% of all decay modes, are given.*

However, the available Odderon triggers (see section 5.1) are designed for the detection of neutrons only, consequently only N^* with a neutron in the final state have to be considered. The neutron rate can be calculated with the Clebsch-Gordan coefficients (see table 4.3). In principle, now the number of neutrons in the final state is known, but the energy and

$\Gamma_{N^*\to n\pi^+}/\Gamma_{N^*\to N\pi}$	$\Gamma_{N^*\to n\pi^+\pi^0}/\Gamma_{N^*\to N\pi\pi}$	$\Gamma_{N^*\to n\eta}/\Gamma_{N^*\to N\eta}$
2/3	2/7	0

Table 4.3: *Fraction of decays where a neutron n is produced over all possible decays where a nucleon N is in the final state for the three main decay modes. The results were obtained by considering the Clebsch-Gordan coefficients. For the proton in the initial state the η-decay mode yields no neutrons.*

p_t-distribution needs to be known for the simulation of the FNC trigger element (section 5.1) and the FNC acceptance region (section 5.5.1). For this reason the N^* decay is modelled using the particles' four momenta.

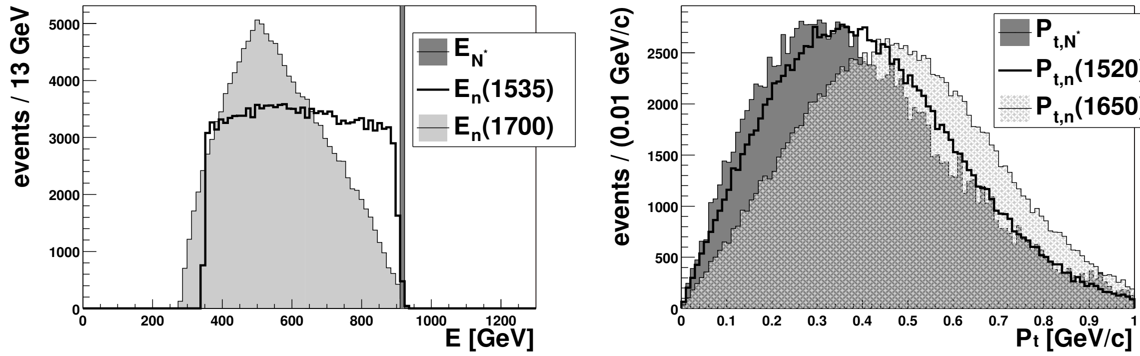

Figure 4.2: *The energy and the transverse momentum of the* $\mathbb{O}\mathbb{P}$*IUM-neutrons are shown for different particle mothers at each case. The distributions depend on both the mass of the* N^* *and the fraction decaying in one and two pions, respectively. For the decay in only one pion the energy distribution would be flat within the kinematically accessible range (compare lower plot of 1.21 for photons) An admixture of two-pion decays distorts the shape (see tables 4.2 and 4.3). The larger the available energy for the neutron from the* N^**-decay (large* N^**-mass and small (effective-)pion-mass), the larger the transverse momentum. For comparison the respective distributions for the* N^**-mothers is shown. It can be seen that the energy of the excited proton has almost not changed.*

For the simulation of the two decay modes with a neutron in the final state a Lorentz transformation to the centre of mass system of the designed N^* is performed. The decays are approximated by isotropic decays. In the case of the two-body decay $N^* \to n\pi^+$ this is straight forward, however for the three-body decay $N^* \to n\pi^+\pi^0$ a further simplification was applied. The three-body system is considered as an effective two-body system where one particle consists of the two pions and the other one is represented by the neutron. The mass $m_{\pi^+\pi^0}$ of the former effective pion-pion particle is limited to the range 274.55 MeV$\equiv m_{\pi^0} + m_{\pi^+} \leq m_{\pi^+\pi^0} \leq m_{N^*} - m_n$ and is randomized from a uniform distribution within the stated bounds. 80.4 % of the neutrons are accompanied by one pion and the remaining 19.6 % by two pions, which is reflected in the decay simulation. In 42.0 % of all cases a neutron is in the final state with the main contribution of 53 % from the $N^*(1520)$.

The neutron obtained is transformed back in the lab-system and from now on it can be treated like a regular generated particle. Figure 4.2 shows the energy and transverse momentum distributions for the particular neutrons stemming from the different N^* considered, and figure 4.3 shows the respective impact points of the neutrons in a plane perpendicular to the beam axis.

4.3 The PYTHIA Generator

Beside the reaction in (4.2), it is possible that other background processes have a similar signature as the signal (4.4). In order to prove compatibility of the data it is also important to simulate these background events. Therefore the generators *PYTHIA 5.7 and JETSET*

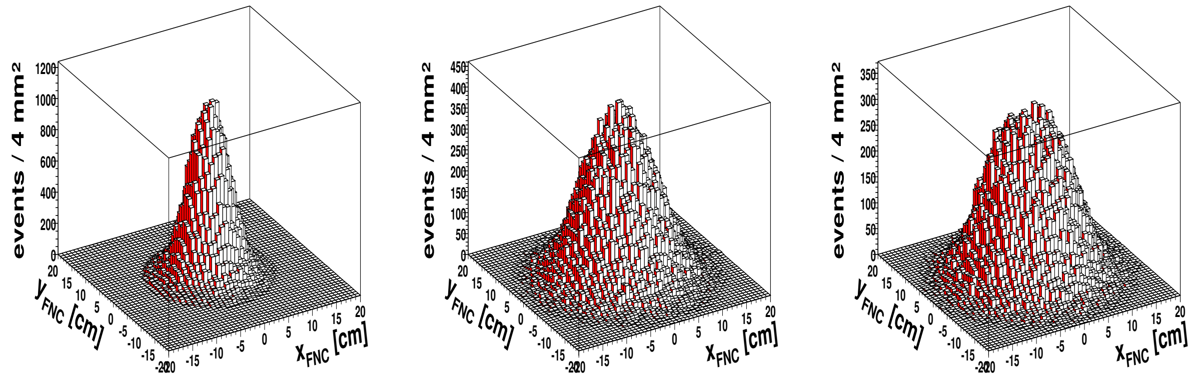

Figure 4.3: *The impact points of the $\mathbb{O}\mathbb{P}$IUM-neutrons in a plane through the FNC perpendicular to the beam axis is shown. The left plot contains the distribution for the N^*, the centre and the right one represent the neutrons from the $N^*(1520)$ and $N^*(1535)$ decays, respectively.*

7.4 [SJO94] were used. The program is intended to generate complete events, in as much detail as experimentally observable, within the bounds of the current understanding of the underlying physics. In particular PYTHIA comprises the processes generated by DIFFVM so that only PYTHIA is used for a direct comparison of the data and the Monte Carlo.

The acceptance for detectable events (see section 5.1) is restricted to the region in equation (4.1), which is represented by the photoproduction regime (see section 1.1.2). PYTHIA renders the possibility to access different kinematical regions in *ep*-scattering. For photoproduction a mix of the three allowed processes is available, which is chosen in this analysis: direct, VMD and anomalous (see section 1.1.2).

4.3.1 Treatment of PYTHIA

PYTHIA is a program for multi-particle production, but it is not a safe prediction for exclusive few-body final states, and the same holds for all other general-purpose generators. This section demonstrates the problems resulting from the use of PYTHIA and how this “grey area” is handled best.

The main background is expected from low multiplicity events with a pion in the final state according to the exclusiveness of the measurement (see section 5.4.4). These final states are induced by so-called “diffractive states”[2] supplied by PYTHIA. However, isospin conservation is violated by some of these decays. For example the decay is allowed:

$$\gamma p \rightarrow \text{rho\_diff0}\; p \rightarrow \pi^0 \pi^0 X, \tag{4.5}$$

where X is the excited proton. According to [SJO00] these “diffractive states” are supposed to represent a γ that by VMD turns into a ρ^0 which thereafter scatters (by Pomeron exchange) to an excited colour-singlet state in the final state. Yet the decay is described as a string whose fragmentation is not fed any information on isospin.

[2] In particular the particles “rho_diff0” (KF = 110), “omega_diff0” (KF = 220), “phi_diff0” (KF = 330).

On the one hand these "diffractive" processes contribute considerably to the background, on the other hand they represent a model to describe high multiplicity states on average and there is no proof that they correctly model exclusive states.

For a conservative approximation two extreme *ansätze* are pursued. Two PYTHIA samples are used: The first one is the default PYTHIA (called *PYTHIA* in the following), in the second sample all processes induced by "diffractive states" are excluded (called *PYTHIA ND* – *N*o *D*iffractive states – in the following). A mixture of these two bordering cases is believed to yield the most realistic description of observed data.

4.3.2 Preselection

The cross section for the considered photoproduction regime (see equation (4.1)) amounts to:

$$\sigma_{ep} = 2.308\ \mu\text{b}, \tag{4.6}$$

which is huge compared to the predicted cross section of the signal process (see table 1.1). From equation (2.5) follows that the number of events is proportional to the cross section, given the luminosity. In order to minimize the number of events necessary to produce a luminosity of comparable size, the PYTHIA generation is restricted to the kinematically accessible regions available to the experiment. The cuts for this preselection, which are applied before the time-consuming detector-simulation, are enumerated in table 4.4.

cut	ϵ_i	$\prod_i \epsilon_i$
$N_\gamma(179.7° > \theta_\gamma > 176°\ \&\&\ E_\gamma > 2\text{ GeV}) \geq 1$	8.1%	8.1%
$N_\gamma(179.7° > \theta_\gamma > 145°\ \&\&\ E_\gamma > 0.01\text{ GeV}) \geq 2$	82.9%	6.8%
$(E - P_z)_{e' N_\gamma(179.7° > \theta > 145°\ \&\&\ E_\gamma > 0.01\text{ GeV})} > 47\text{ GeV}$	25.9%	1.7%

Table 4.4: *PYTHIA preselection cuts with the efficiency in the second column and the all over efficiency in the last column. The cuts are explained in the text.*

The two calorimeters provided for the detection of a photon are the VLQ (see section 3) with a minimum resolved energy larger than 2 GeV and the Spacal (see section 2.4) with a minimum resolved energy larger than 0.01 GeV. Furthermore the Odderon-triggers (equations (5.9)-(5.11)) demand activity in the VLQ.

Thus, the first cut requires at least one photon in the cone around the VLQ and with an energy larger than 2 GeV. The second cut demands at least two photons in the cone including the Spacal and the VLQ with an energy larger than 0.01 GeV. In addition a further cut is applied on the exclusivity of the event explained in 5.4. The cuts are rather soft in order not to introduce a bias, but still a reduction of approximately a factor of 60 is reached.

Table 4.5 gives an overview over the number of events generated:

	PYTHIA	OPIUM	DIFFVM
$N_{generated}$	16 200 000	143 904	101 932
$N_{after\ preselection}$	280 068	143 904	101 932
σ_{ep} [nb]	*2 308	9.41 (tab. 1.1)	**12.2 [BER97] (***1.04)
L [pb^{-1}]	7.02	15.29	98.3

Table 4.5: *Overview over the event generation: The number of events produced, the number after the PYTHIA preselection, the cross sections, and the resulting luminosities are given.*
* *cross section provided by the PYTHIA generator.*
** *assuming that the ratio of the elastic to proton-dissociative ω photoproduction cross section is ≈ 2, which is shown for the ρ^0 in [ZEU98].*
*** *cross section for the underlying generated decay mode $\omega \rightarrow \pi^0\gamma$.*

Chapter 5

Search for Exclusive π^0 Production

In this analysis the reaction

$$\gamma + p \rightarrow \pi^0 + N^*, \tag{5.1}$$

is studied, where the photon is emitted by the incoming electron (explained in section 1.3.2, and shown in figure 1.17). The presented investigations focus on the decay of the N^* into a final state comprising a leading neutron n:

$$N^* \rightarrow n + X. \tag{5.2}$$

Other channels will not be considered. The signature of this process, where the incoming electron and proton interact via Odderon-photon fusion, is an electron scattered under a small angle, a high-energetic pion in the backward direction, and a neutron in the forward direction. The complete final state of this reaction – i.e. the scattered electron, the leading neutron and two photons from the decayed pion – are detected. The aim of this work is to measure the cross section of this exclusive process or if this is not possible provide a confidence limit.

All data collected during the year 1999 are included in this analysis. The data taking period is divided into two parts, which differ by the trigger settings – see (5.7), (5.8) and (5.9), (5.10). In the following, the first period is stated as *99-1*, and the second as *99-2*, respectively.

For the preselection of the data two subtriggers *S96* and *S97* are available which are specified in sections 5.1.1 and 5.1.2, respectively. Requiring that all detector components used in this analysis were operational during data taking, for the *S96* subtrigger an integrated luminosity of 4.45 pb^{-1} is obtained for *99-1* and 6.61 pb^{-1} for *99-2*. In the same manner an integrated luminosity of 6.66 pb^{-1} is obtained for *99-1* and 9.91 pb^{-1} for *99-2* for the *S97* subtrigger. In the total run period in 1999 the trigger (either *S96* or *S97*) fired roughly 600 000 times.

5.1 The Odderon Trigger

The clear event signature of the signal reaction allows for the setup of a straight forward subtrigger. For the detection of the final state particles from equation (5.1), (5.2) and the scattered electron the H1 detector provides trigger signals from the following subdetectors:

- The VLQ and the Spacal in the backward direction detect the two photons from the pion decay.
- The electron tagger at $z = -33$ m (eTAG$_{33}$) identifies the scattered electron.
- The FNC is utilized to measure the leading neutron emerging in the process.

Together with additional global options these trigger elements are used to build two Odderon subtriggers *S96* and *S97*.

5.1.1 The Odderon Subtrigger "S96"

The subtrigger *S96* consists of two trigger elements on level 1, eTAG and FNC$_{Esum>1/2}$ explained in the following:

The eTAG Trigger Element

On trigger level 1 (L1) the subtrigger *S96* requires a positive signal of the electron tagger which is:

$$E_{eTAG_{33}} > 4 \text{ GeV and } E_{PD} < 2 \text{ GeV} . \tag{5.3}$$

$E_{eTAG_{33}}$ denotes the energy measured in the electron detector at $z = -33$ m and E_{PD} the energy of the photon detector. The condition in the photon detector guarantees the suppression of Bethe-Heitler processes, which have a clear signature: an electron in the electron tagger, a photon in the photon detector, and the energy sum of both particles amounting to 27.56 GeV, i.e. the beam energy of the incoming electron.

Efficiency of the Electron Tagger eTAG$_{33}$

The run dependent electron tagger efficiency [LEV95] is available as a function of y for electrons scattered into the fiducial region (5.38) of the electron tagger.

In its acceptance region, which is defined by $Q^2 < 0.01$ GeV^2 and y between 0.3 and 0.7, the eTAG$_{33}$ efficiency can be parameterized by a polynomial $\epsilon_{eTAG}(y)$ of sixth order:

$$\epsilon_{eTAG}(y) = \sum_{i=0}^{6} a_i \cdot y^i \tag{5.4}$$

with parameters a_i as shown in figure 5.1.

The correction for migration of events into and out of the y-acceptance region (0.3,0.7) is detailed in section 5.6.

The FNC Trigger Element

The second requirement of *S96* on trigger level 1 is FNC$_{Esum>2}$ for *99-1* and FNC$_{Esum>1}$ for *99-2*, denoting:

$$E_{FNC} > 200 \text{ GeV for } \textit{99-1} \text{ and} \tag{5.5}$$

$$E_{FNC} > 100 \text{ GeV for } \textit{99-2}. \tag{5.6}$$

The change from *99-1* to *99-2* is due to a gain in the trigger efficiency.

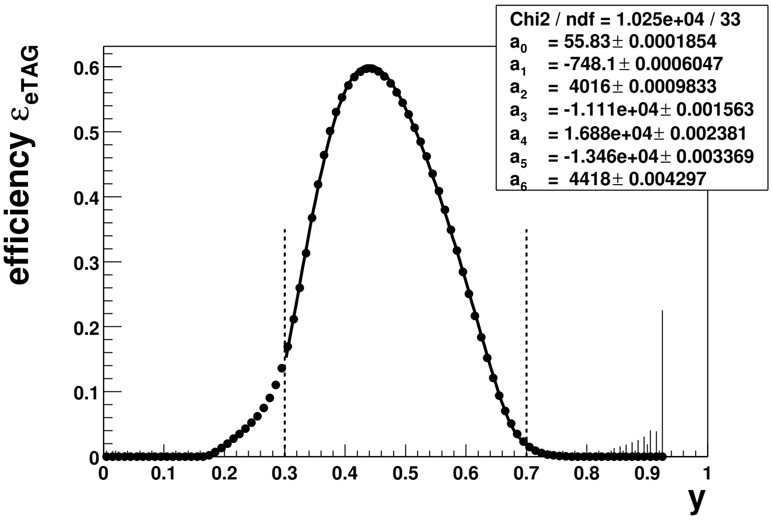

Figure 5.1: *The efficiency of the electron tagger as a function of the inelasticity y. For the y-region between 0.3 and 0.7 (indicated by the dashed lines) the curve is fitted with a polynomial of sixth order (see equation (5.4)).*

Efficiency of the FNC Trigger Element

The trigger efficiencies for *99-1* and *99-2* were determined using subtrigger *S6* (SPCLe_IET>0), which is completely independent of the FNC and asks only for energy in the Spacal. Figure 5.2 shows the efficiencies for *99-1* and *99-2*. In addition, the efficiencies for several FNC trigger thresholds are shown. Comparing plot (a) and plot (b) of figure 5.2 shows that for *99-1* $\mathrm{FNC}_{Esum>4}$ instead of $\mathrm{FNC}_{Esum>2}$ was required which had a threshold of approximately 400 GeV instead of 200 GeV. The fits shown in figure 5.2 yield:

$$\epsilon_{FNC_{99-1}}(E_{FNC}) = \frac{0.99}{\exp\left(\frac{572-E_{FNC}[\mathrm{GeV}]}{63.6}\right)+1} \tag{5.7}$$

$$\epsilon_{FNC_{99-2}}(E_{FNC}) = \frac{0.96}{\exp\left(\frac{186-E_{FNC}[\mathrm{GeV}]}{14.5}\right)+1}\,. \tag{5.8}$$

The L4 Physics Finder

In order to further restrict the rate with which events are written to tape a preselection on level 4 is necessary, where the full H1 detector raw data is used for reconstruction. Therefore a more sophisticated decision is taken:

$$N_{VLQ} > 0 \text{ for } \textit{99-1} \text{ and} \tag{5.9}$$

$$E_{VLQ} > 5 \text{ GeV for } \textit{99-2}, \tag{5.10}$$

where N_{VLQ} denotes the number of clusters reconstructed in the VLQ and E_{VLQ} denotes the energy measured in the VLQ. The requirement was changed from *99-1* to *99-2* in order to be independent of eventual misreconstruction of the clusters.

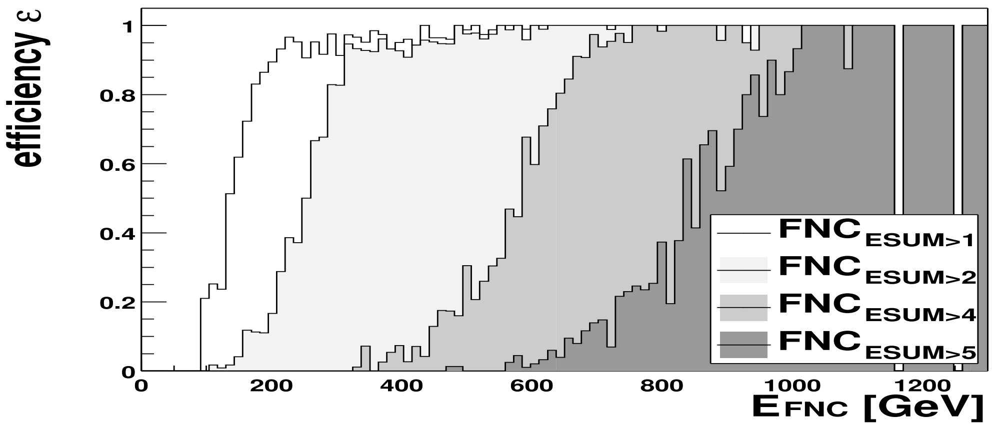

(a)

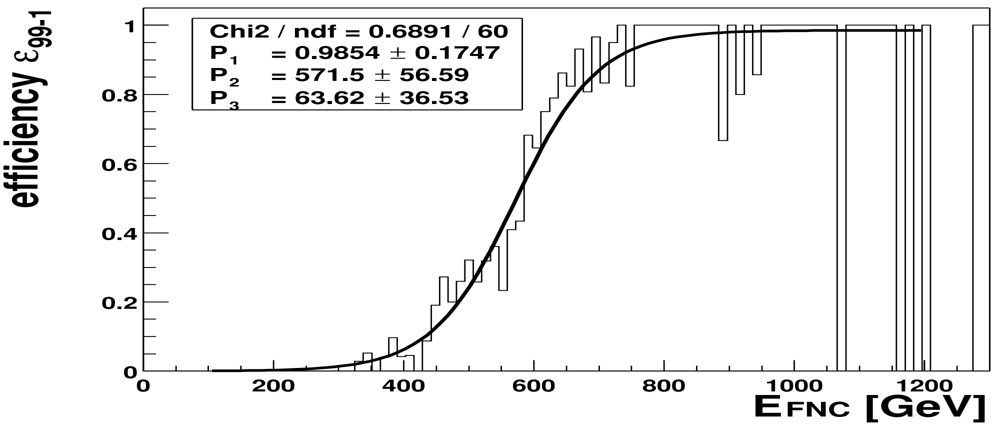

(b)

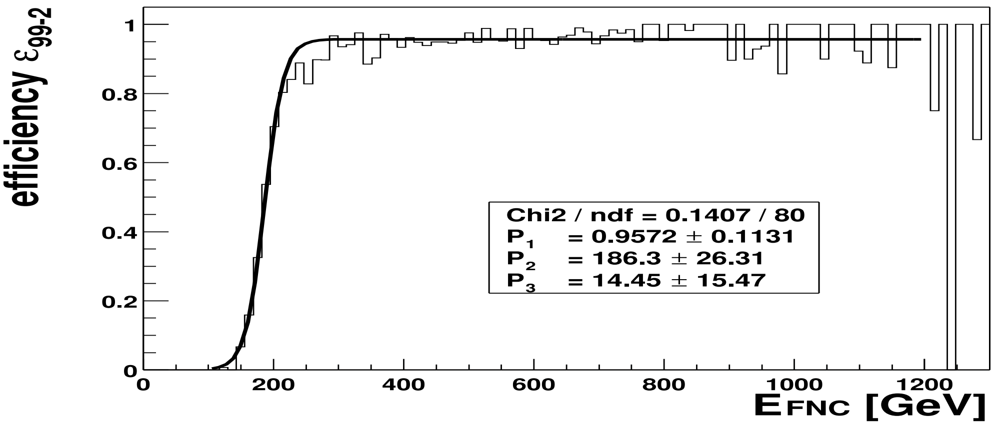

(c)

Figure 5.2: *Plot (a) shows the efficiency of the FNC trigger element for several thresholds as a function of the cluster energy in the FNC ($FNC_{Esum>3}$ is the same as $FNC_{Esum>2}$). Plot (b) shows the FNC trigger efficiency for* 99-1 *($FNC_{Esum>2}$) and plot (c) shows the FNC trigger efficiency for* 99-2 *($FNC_{Esum>1}$) as a function of the cluster energy in the FNC. Functions (5.7) and (5.8) give the result of the respective fits for* 99-1 *and* 99-2.

5.1.2 The Odderon Subtrigger "S97"

The subtrigger *S97* consists of the same trigger setup as the *S96* subtrigger ($FNC_{Esum>1/2}$ and eTAG) plus a further requirement on level 1, VLQ_{noise}, which means:

$$E_{VLQ} > 6 \text{ GeV}. \tag{5.11}$$

The efficiency of the VLQ_{noise} trigger element has not yet been determined by the end of this analysis. Hence, the Odderon subtrigger *S97* is not used in this work.

5.2 Reconstruction of the Kinematic Variables

Since the γp-centre of mass energy is approximately 200 GeV, the electron, proton and π^0 masses will be neglected for the reconstruction of the kinematic variables.

5.2.1 Reconstruction of y and Q^2 with the Electron Method

The variable y and the four-momentum transfer at the electron-photon vertex Q^2 are reconstructed making use of the electron method [BEN91]. The variables used for the kinematic reconstruction of an event are the scattering angle θ, the energy of the incoming electron E, and the energy of the outgoing scattered electron E':

$$y = 1 - \frac{E'}{E}\sin^2\theta/2 \tag{5.12}$$

$$Q^2 = 4EE'\cos^2\theta/2. \tag{5.13}$$

In the studied reactions, the electrons are scattered at small angles only so that $\theta \approx \pi$ can be assumed. This approximation leads to the following terms for y and Q^2:

$$y = 1 - \frac{E'}{E} \tag{5.14}$$

$$Q^2 = 0 \text{ GeV}^2. \tag{5.15}$$

5.2.2 Reconstruction of the Photon-Proton Centre of Mass Energy W

The photon-proton centre of mass energy is defined by equation (1.9):

$$W^2 = -Q^2 + 2qP + M^2. \tag{5.16}$$

Inserting the definition of s in the definition of y, i.e. equation (1.7) in equation (1.6), one is lead to $2qP = ys$. Consequently, with the above mentioned approximations the photon-proton centre of mass energy can be written as:

$$W = \sqrt{sy}, \tag{5.17}$$

where y is calculated from equation (5.14).

5.2.3 Reconstruction of the Four-Momentum Transfer at the Proton Vertex t

In equation (1.8), the four-momentum transfer is defined by $t = (P - X)^2$ with the four-momenta P and X of the incoming proton and of the outgoing hadronic system, respectively. Since X is not completely measured[1], t has to be determined in a different way. Four-momentum conservation yields:

$$t = (p_{\gamma\gamma} - q)^2, \tag{5.18}$$

with $p_{\gamma\gamma} = p_{\gamma_1} + p_{\gamma_2}$, the four-momentum of the two-photon system and q the four-momentum of the photon emitted by the electron. In the approximation that the virtual photon has no transverse momentum and that the energy transfer is nevertheless governed primarily by the virtual photon, the momentum transfer is given by:

$$t = -2E_{\pi^0}^2(1 - \cos\vartheta), \tag{5.19}$$

where ϑ is the angle of the outgoing pion. At small values $\cos\vartheta \approx 1 - \vartheta^2/2$ and $\vartheta \approx \sin\vartheta$. Therefore, in this approximation

$$t = -2E_{\pi^0}^2(1 - 1 + (\sin^2\vartheta)/2) = -E_{\pi^0}^2 \sin^2\vartheta = -(\boldsymbol{p}_{\gamma\gamma,\perp})^2. \tag{5.20}$$

5.2.4 Reconstruction of the Invariant Mass $m_{\gamma\gamma}$ of the Photon-Photon System

The mass of the two-photon system is obtained by the sum of the four-momenta of the two photons:

$$m_{\gamma\gamma} = \sqrt{p_{\gamma\gamma}^2} = 2E_1E_2(1 - \cos\Phi_{\gamma_1\gamma_2}) \qquad \text{with} \qquad p_{\gamma\gamma} = p_{\gamma_1} + p_{\gamma_2}. \tag{5.21}$$

Here, E_1 and E_2 are the energies of the measured calorimeter clusters and $\Phi_{\gamma_1\gamma_2}$ is their opening angle.

5.3 The Four Different Event Signature Classes

This section gives an overview of the calorimeter configurations possible for the detection of the two photons (see figure 5.3). As specified in section 5.4.1, the events selected can be divided into four classes. The corresponding geometric acceptances for the signal determined from $\mathbb{OPIUM}$ are given in brackets:

- both photons detected in the identical VLQ module, called VV_i (1.7%).
- one photon in the upper, one in the lower module, called VV_d (0.5%).
- one photon in the VLQ and one in the Spacal, called VS (3.6%).

[1]Only the neutron from the outgoing hadronic system is detected, the remaining particles disappear through the beam pipe etc.

- both photons in the Spacal, called SS (11.2%).

In the remaining 83% of the cases at least one photon does not hit either of the two calorimeters.

The invariant mass of two photon candidates (section 5.4.1) for the different configurations is shown in figure 5.4 for OPIUM, DIFFVM and PYTHIA. The detection of one photon from the pion and the "single photon" in the omega sample ($\omega \to \pi^0\gamma$) leads to the so-called "reflection" of the ω – figure 5.4 (b) and (e) – where the reconstructed mass is always smaller than the ω mass. It is highly dependent on the opening angle, so that it emerges only if the Spacal is involved. However, little amount of background is seen in the pion mass range of figure 5.4 (e). Beside the π^0 also tails of the distribution to higher masses and the η are visible in figure 5.4 (c) and (f). Due to the higher mass of the η the opening angle of the two decay-photons is larger and thus it can only be detected if at least one photon hits the Spacal.

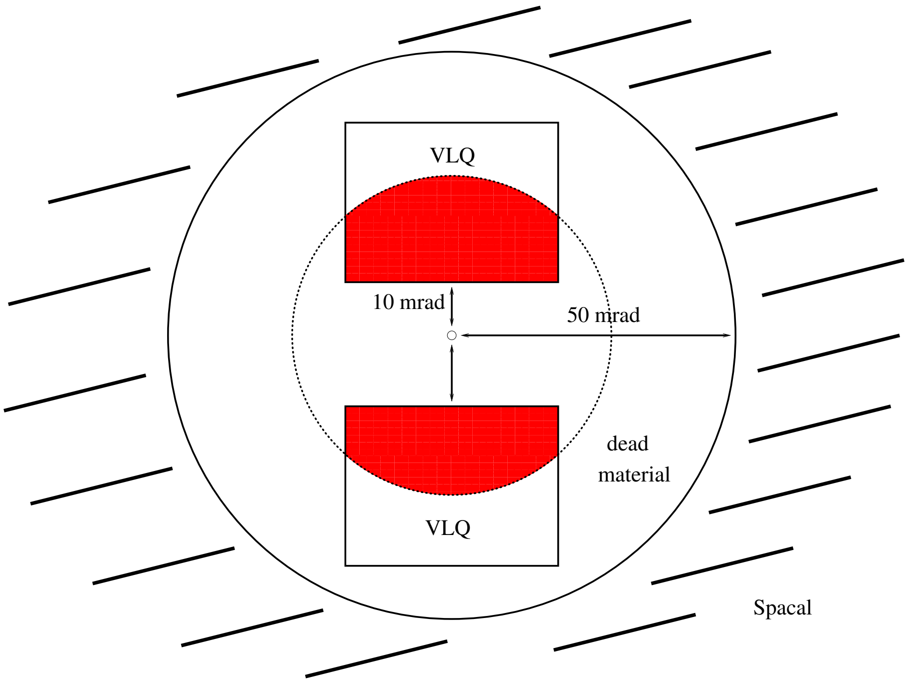

Figure 5.3: *Sketch of the VLQ and the Spacal, projected onto a plane perpendicular to the z-axis. The two rectangles represent the upper and lower modules of the VLQ calorimeter, the ring gives the region shaded by dead material (Spacal insert). The rest of the Spacal is represented by the dashed region outside the solid circle.*
Since the Spacal is in front of the VLQ, starting from the interaction point and proceeding outwards, only the grey part of the modules is available for the detection of particles, the rest is shaded by the Spacal. The asymmetry in the distance of the two VLQ modules from the beam pipe is taken into account, and two angles are given for convenience: The edge of the VLQ at 10 mrad and the edge of the active part of the Spacal at about 50 mrad.

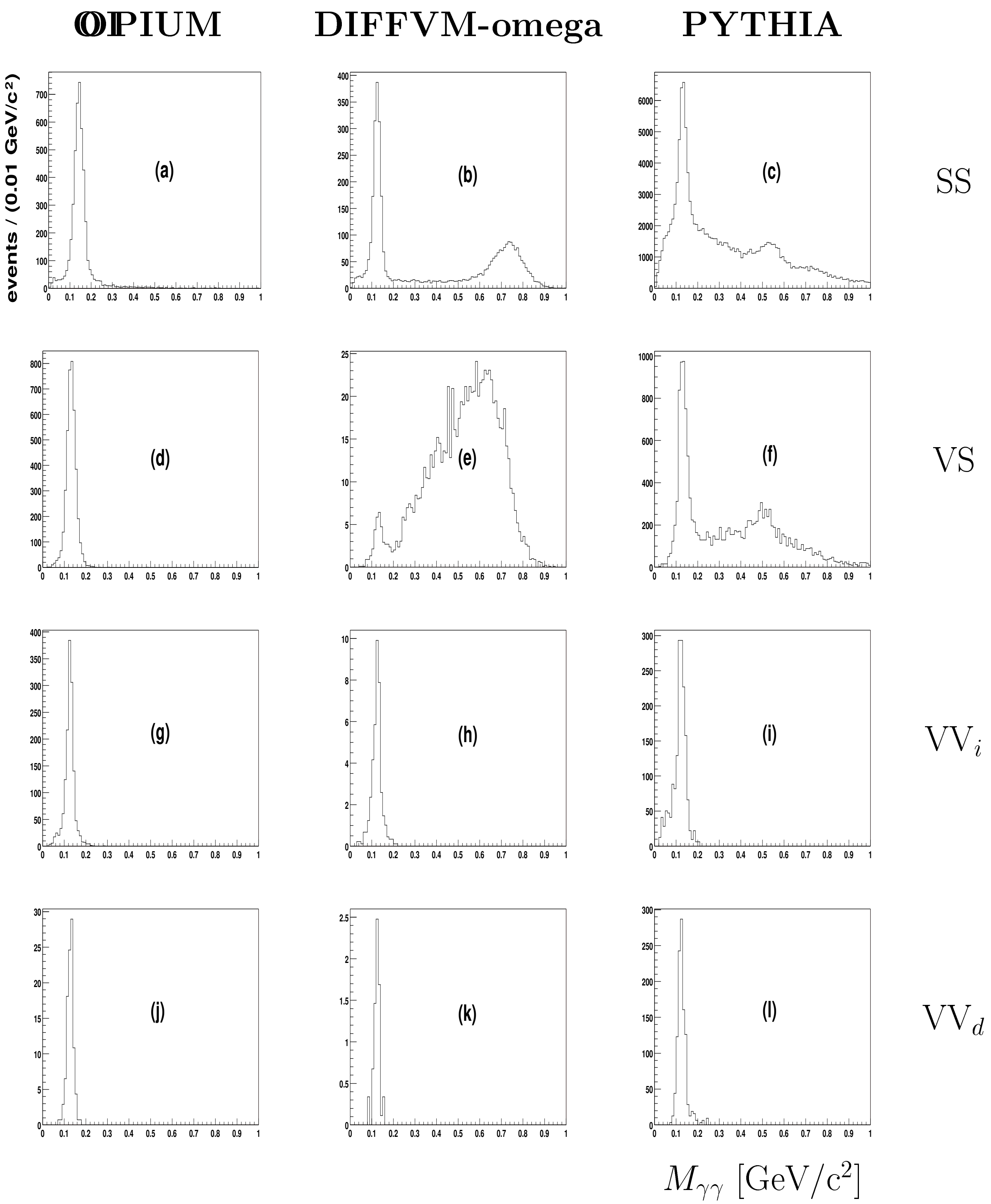

Figure 5.4: *Overview over the $M_{\gamma\gamma}$ spectra for all Monte Carlo generated events and all event classes discussed in figure 5.3. The spectra are normalized to luminosity but only the photon selection cuts from section 5.4.1 are applied. The first column shows the OPIUM spectra, the second column the DIFFVM-omega spectra and the third column the PYTHIA spectra. The four rows represent the four calorimeter configurations: SS, VS, VV_i, and VV_d from top to bottom.*

5.4 The Data Event Selection

The process to be investigated is the exclusive production of π^0 mesons, where the proton is excited (quasi-) diffractively to an N^*. The scattered electron and the neutron from the N^* decay are detected in the electron tagger and the forward neutron calorimeter, respectively. For the detection of the two pion-decay photons, the VLQ and the Spacal are provided.

Since the process has a clear signature, the background processes are rejected without big losses in efficiency. However, the losses due to the geometric acceptance are very large. The cut criteria slightly differ for the varying run periods, *99-1* and *99-2*, due to the different trigger settings. In a preselection, the data sample is reduced to a manageable subsample with the following conditions fulfilled:

- The actual subtrigger *S96* was set.
- In order to make quantitative predictions, the luminosity must be measured. Only runs of "good" or "medium" quality are considered.
- The status of the detector components used in this analysis had to be operational, i.e. the VLQ, the Spacal, the FNC, the Luminosity System, and the parts of the central tracking system: CJC1, CJC2, CIZ, and COZ.

5.4.1 Selection of VLQ and Spacal Photon Candidates

The first condition for the selection of photon candidates in the VLQ and in the Spacal is that the L4 physics finder (see section 2.9) for *99-1* (5.9) and *99-2* (5.10) is verified:

$$\boxed{\mathrm{L4}}\,. \tag{5.22}$$

This requirement is imposed because other L4 finders could also validate an event which does not fulfil (5.22), whereas for Monte Carlo events this is not possible.

As the decay mode $\pi^0 \to \gamma\gamma$ is investigated, the number of detected photons is required to be 2:

$$\boxed{N_\gamma = 2}\,. \tag{5.23}$$

According to section 5.3 there are four different classes into which the events can be subdivided; for illustration of the photons in the VLQ see figure 3.7:

Either both photons are detected in the same module of the VLQ, resulting in 4 clusters:

$$\boxed{N_{cl_{VLQ}} = 4}\,, \tag{5.24}$$

or one photon is in the upper module and one in the lower, resulting in 2 clusters:

$$\boxed{N_{cl_{VLQ}} = 2}\,, \tag{5.25}$$

or one photon is detected in either of the two VLQ modules and the other one in the Spacal:

$$\boxed{N_{cl_{VLQ}} = 1} \quad \text{and} \quad \boxed{N_{cl_{Spacal}} = 1}\,. \tag{5.26}$$

The fourth event class, where both photons are detected in the Spacal, is not accessible with the trigger setup used. Though level 1 allows for this configuration, the software cuts on trigger level 4 reject these events, because a cluster or energy is required in the VLQ (see equations (5.9) and (5.10)).

In the following the three remaining event classes are discussed and the definitions of a photon candidate in the VLQ and in Spacal are given.

Due to electronic noise and the minimum detectable energy of the calorimeters

$$\boxed{E_{\gamma_{VLQ}} > 2 \text{ GeV}} \tag{5.27}$$

and

$$\boxed{E_{\gamma_{Spacal}} > 0.09 \text{ GeV}} \tag{5.28}$$

is demanded for the reconstructed energies.

Both Photons in the same module of the VLQ: As shown in figure 3.7, two photons entering one module of the VLQ generate four clusters. In order to eliminate this ambiguity the reconstructed energies of the clusters are considered. It is assumed that the energy is equally shared under the two projection directions x and y. The argumentation can be understood by subdividing the events into two kinematical regions of the pion decay (see section 1.4):

$$E_{\gamma_1} > E_{\gamma_2} \qquad \text{and} \qquad E_{\gamma_1} \approx E_{\gamma_2} \tag{5.29}$$

The two cases are sketched in figure 5.5.

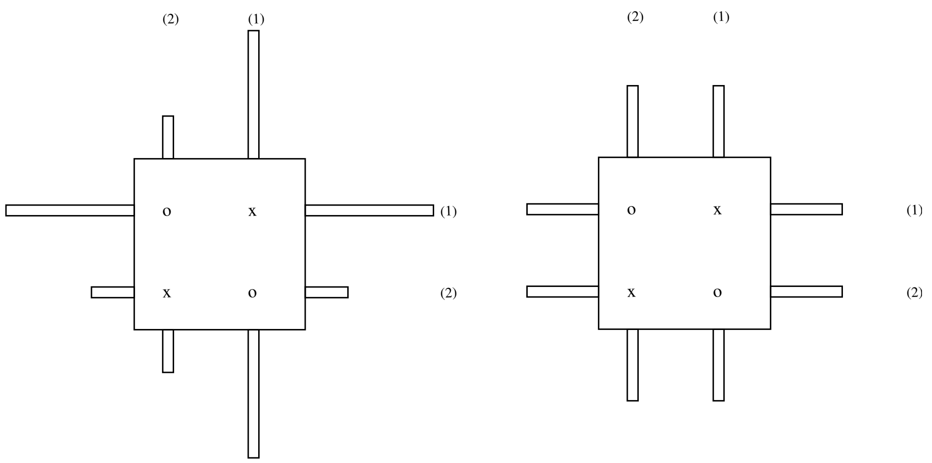

Figure 5.5: *Sketch of one VLQ module which is hit by two photons. The energy projections are indicated.* **x** *denotes the true and* **o** *the incorrectly reconstructed impact points. The numbers in brackets mark the horizontal and vertical energy projections belonging to photon (1) and (2), respectively.*

In the first case (left plot of figure 5.5), where one photon has a larger energy than the other one, the magnitude of the reconstructed energies allows one to identify the true clusters denoted by an **x**: The sum of the energy projections is greatest (respectively, smallest) for the true clusters **x**. The incorrectly reconstructed clusters **o** have energies in between.

When the energies of the two photons are of comparable size, as depicted on the right hand side of figure 5.5, the described method cannot be used anymore due to resolution effects. Yet the determination of the true clusters is not necessary. Only the four-momentum of the alleged pion, from which the photons originate, is of interest. Because of the symmetry of the azimuthal decay angle, the reconstructed pion is the same for the incorrect **o** or the true **x** clusters.

These requirements are met by selecting the most energetic cluster and the one with the largest spatial distance:

$$\boxed{\text{Cluster selection}}\,. \tag{5.30}$$

A further cut is made, which takes advantage of a particular kinematical condition: Due to the electron, which is detected in the electron tagger, the energy of the emitted virtual photon and thus the energy of the pion is restricted to the range 8 GeV $\lesssim E_{\pi^0} \lesssim$ 20 GeV – see figure 4.1 (c). This directly affects the opening angle of the two photons $\Phi_{\gamma\gamma}$ (shown in figure 1.20) and therefore, the distance of the two clusters $D_{\gamma\gamma}$. This is due to the limited accessible angular range in the VLQ, so that

$$\Phi_{\gamma\gamma} \approx \tan \Phi_{\gamma\gamma} \propto D_{\gamma\gamma}. \tag{5.31}$$

The minimum opening angle is obtained for the maximum pion energy and equal photon energies (see top of figure 1.21) and corresponds to a minimum distance of the two clusters in the VLQ of about 4 cm. Considering resolution effects, the cut is softened in order to maintain efficiency:

$$\boxed{D_{\gamma\gamma} > 3 \text{ cm}}\,. \tag{5.32}$$

This cut suppresses background, such as the coincidence of two particles which hit the VLQ and do not originate from the considered pion decay. Another source of background eliminated by this cut is a malfunction of the cluster reconstruction, the splitting of clusters. With a certain probability the routine reconstructs two clusters with a very small distance instead of one. The effect is illustrated in figure 5.6.

One Photon in the Upper Module and one in the Lower Module of the VLQ: No additional cuts have to be applied for this case.

One Photon in the VLQ and one in the Spacal: The photon candidate is required to be contained in the fiducial volume of the Spacal. The Spacal covers the polar angular

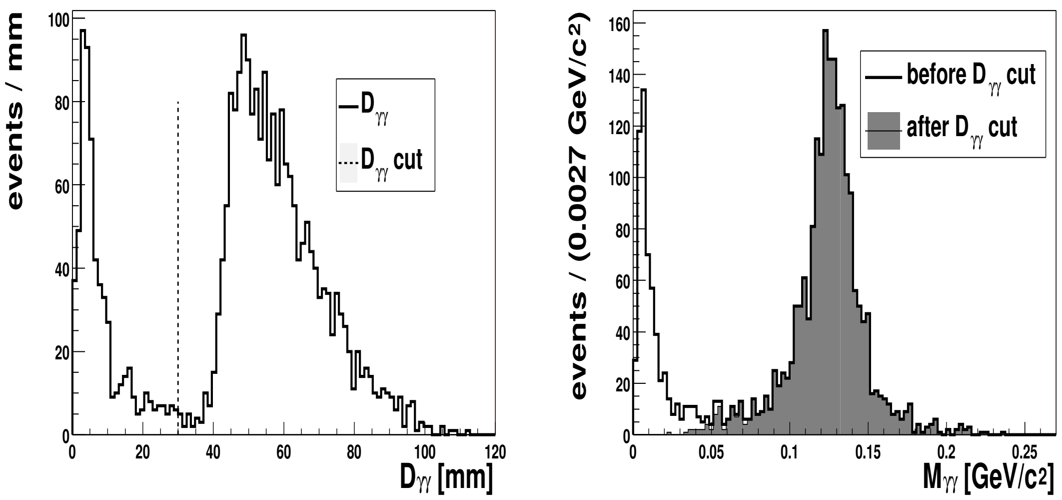

Figure 5.6: *The left plot shows the distribution of the distance of the two clusters reconstructed in the identical VLQ-module for $\mathbb{OP}$IUM events. From figure 1.20, it follows that the minimum possible opening angle of the two photons corresponds to a distance of the photons in the VLQ plane of 40 mm. Taking resolution effects into account, a cut at 30 mm is made (dashed line in the left plot). In the plot on the right hand side, the invariant mass of the two photons is shown before and after the cut.*

range of $153° \leq \theta \leq 178°$, and corresponds to a distance from the beam pipe of 6.7 cm $\leq d \leq$ 81.8 cm. An event is accepted if

$$\boxed{8 \text{ cm} \leq d_\gamma \leq 75 \text{ cm}} \tag{5.33}$$

is fulfilled. This ensures that the energy is fully deposited in the cells of the Spacal and no shower leakage occurs.

Aside from cut (5.28), a set of cuts is used for the selection of exactly one cluster in the Spacal. In order to motivate the procedure, some problems of the cluster reconstruction in the Spacal have to be pointed out which are known as *splitting and merging* [SWA00].

- *Merging*: A cluster radius is assigned to every cluster according to the lateral dimension of a particle shower in the Spacal. In case two clusters overlap, and assuming that the cluster reconstruction routines tend to attribute cell energy between two clusters to the cluster with less energy, the energy of noise clusters can increase considerably. In the worst case it is no longer possible to separate the two clusters.
- *Splitting*: The splitting of two clusters is the inverse process. The energy of a particle shower in the Spacal is distributed in such a way that the cluster reconstruction makes several clusters out of one.

The following cuts take these two effects into account:

A cluster with more than 300 MeV is considered a "real" cluster, caused by the impact of a particle on the Spacal (compared to an "inflated" noise cluster). Thus, at most one cluster with an energy larger than 300 MeV is allowed:

$$\boxed{N_{cl}|_{E_{cl}>300\ \mathrm{MeV}} \leq 1}\ . \tag{5.34}$$

Clusters with an energy smaller than 300 MeV cannot unambiguously be assigned to "real" clusters as they may also result from noise or be off-split parts of regular clusters (see above). To increase the acceptance, it is desirable to also select particles with smaller energies. A compromise between these two requirements is reflected by the additional cut:

$$\boxed{E_{\gamma_{Spacal}}/E_{SUM_{Spacal}} > 0.667}\ , \tag{5.35}$$

which denotes that at least 2/3 of the energy sum of all clusters in the Spacal accounts for the photon candidate. Events with many high-energetic (high-energetic compared to the photon candidate) clusters are rejected by this cut; on the other hand, a cluster with a low energy may survive.

In order to reduce the loss of efficiency, no further cuts on the hadronic energy fraction, the cluster radius, and the number of cells assigned to a cluster are applied.

5.4.2 Selection of the Scattered Electron in the eTAG$_{33}$

For the detection of the scattered electron the eTAG$_{33}$ is used only. The kinematics of the reaction is determined by the scattered electron. The events fulfil:

$$\boxed{y \in (0.3, 0.7)} \tag{5.36}$$

$$\boxed{Q^2 < 0.01\ \mathrm{GeV}^2}\ . \tag{5.37}$$

These constraints are derived from the acceptance region of the electron tagger. Furthermore, the electrons have to be well contained inside the fiducial volume of the eTAG$_{33}$ which is guaranteed by:

$$\boxed{|x_{eTAG_{33}}| < 6\ \mathrm{cm}}\ . \tag{5.38}$$

In order to suppress Bethe-Heitler processes (see section 5.1.1), the energy of the photon detector is required not to exceed a given limit:

$$\boxed{E_{PD} < 2\ \mathrm{GeV}}\ . \tag{5.39}$$

5.4.3 Selection of the Leading Neutrons in the FNC

The leading neutron n from equation (5.2) is detected in the FNC (section 2.5). The neutron is accepted, if the following conditions are fulfilled.

- There is only one cluster reconstructed in the FNC:

$$\boxed{N_n = 1}\,. \tag{5.40}$$

- The total charge which is contained in the considered cluster is 0:

$$\boxed{q = 0}\,. \tag{5.41}$$

- The timing of the cluster signal has to be in coincidence with the time of the bunch crossing in which the event happened. This cut ensures that the cluster does not originate from another bunch crossing:

$$\boxed{\text{correct timing}}\,. \tag{5.42}$$

- The energy of the neutron candidate is required to be larger than 400 GeV for *99-1* and larger than 100 GeV for *99-2* due to the different trigger thresholds:

$$\boxed{E_n > 400\ \text{GeV}}\ \text{for}\ \textit{99-1} \qquad \text{and} \qquad \boxed{E_n > 100\ \text{GeV}}\ \text{for}\ \textit{99-2}\,. \tag{5.43}$$

- The reconstructed impact point of the cluster has to lie inside the acceptance region shown in figure 5.7 (d) and section 5.5.1. This cut provides, in particular, the rejection of protons which are deflected upwards by the dipole magnets of the proton beam line and which hit the top part of the calorimeter:

$$\boxed{\text{Impact point inside acceptance region}}\,. \tag{5.44}$$

Figure 5.7 shows the xy-distributions of the clusters in the FNC after the respective cuts.

5.4.4 Selection of Exclusive Events

The π^0 in the final state is guaranteed to be exclusive by two decisive cuts detailed in the following.

The first requirement is based on the central tracking system (see section 2.6). Since there are only neutral particles produced in the final state (5.1) no tracks in the central region of the H1 detector are possible. Therefore, an event with a vertex reconstructed from tracks is rejected:

$$\boxed{\text{No vertex reconstructed}}\,. \tag{5.45}$$

This cut rejects the background which is well contained in the central region of the H1 detector. However, particles produced under small angles with respect to the beam pipe are not rejected by this cut, since no tracking devices exist in this kinematical region. Therefore

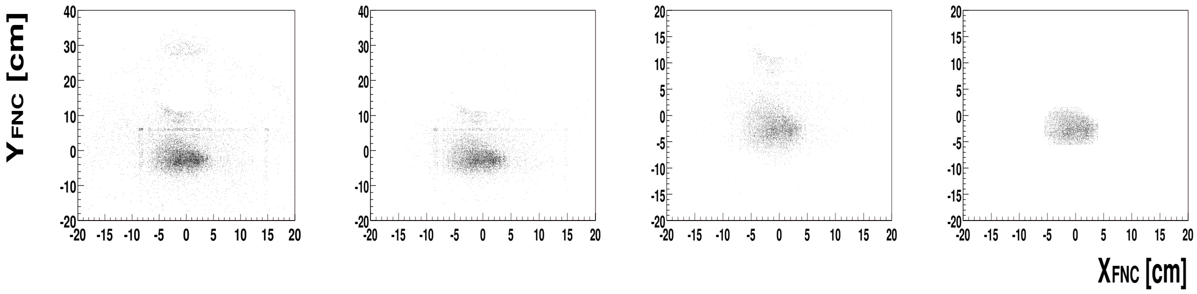

(a) (b) (c) (d)

Figure 5.7: *The hit map of the reconstructed clusters in the FNC after the respective cuts: (a) All reconstructed clusters, (b) only one reconstructed neutral cluster ((5.40) and (5.41)), (c) correct timing and energy ((5.42) and (5.43)), (d) only clusters inside the acceptance region (5.44). In plot (a) the recess of the beam pipe can be seen. The last cut prevents deflected protons which reside below the beam pipe from entering the analysis.*

a new variable is defined in order to reject those events. Energy and momentum conservation implies conservation of this variable $\sum_i (E - P_z)_i$, where i runs over all particles in the initial or final state, respectively. This variable is constructed in such a way that the incoming proton does not contribute ($(E - P_z)_p = 0$ GeV, neglecting the proton mass). Thus, only the incoming electron contributes and the variable can be determined to be $(E - P_z) = (E - P_z)_e = 55.12$ GeV.

Due to the small scattering angle, $(E - P_z)$ of the outgoing nucleonic state can be safely set to zero. The remaining particles in the final state are the scattered electron and the two photons from the pion decay: $(E - P_z)_{e'\gamma\gamma} := \sum_{i=e',\gamma,\gamma}(E - P_z)_i$. Exclusiveness of an event is ensured by the requirement:

$$\boxed{49 \text{ GeV} < (E - P_z)_{e'\gamma\gamma} < 60 \text{ GeV}}\,. \tag{5.46}$$

In figure 5.8 one can see that two kinds of background are rejected due to this cut:

- Events where undetected particles leave the H1 detector in the backward direction (less than 49 GeV).
- If two events overlap[2] and both scattered electrons are detected (more than 60 GeV).

Due to the preselection for PYTHIA (see table 4.4), the cut (5.46) cannot be softened towards smaller values of $(E - P_z)$. (5.46).

The Mass Window Cut

The final cut defines the pion mass window which is determined with the $\mathbb{OPIUM}$ sample. The mass distribution is fitted with a Gaussian in order to take resolution effects into account.

[2]Overlap events denote that more than one electron and one proton interact in a bunch crossing.

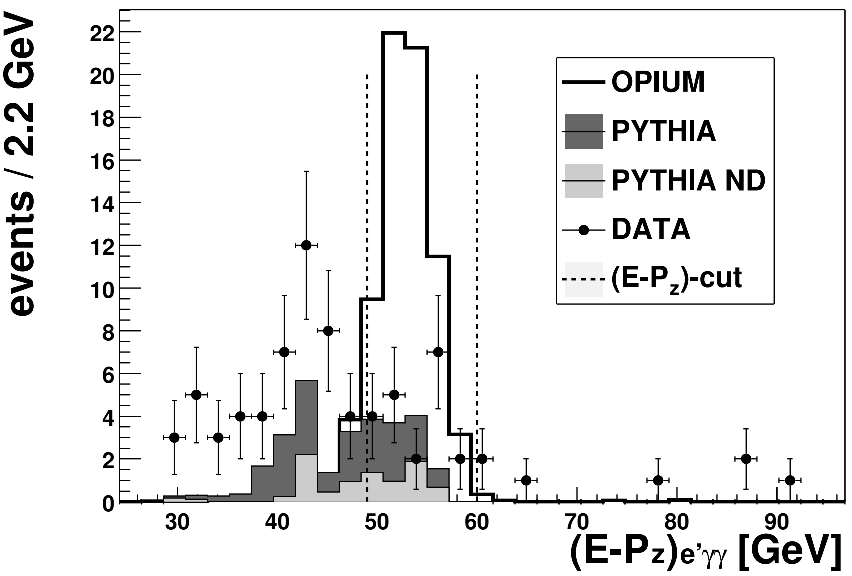

Figure 5.8: *The $(E-P_z)_{e'\gamma\gamma}$ distribution for the case in which one photon is detected in the VLQ and the other photon in the Spacal. Due to the $(E-P_z)$-PYTHIA preselection cuts in table 4.4 data and PYTHIA can only be compared for $(E-P_z)_{e'\gamma\gamma} \gtrsim 49$ GeV. On the other hand PYTHIA does not describe overlap events with $(E-P_z)_{e'\gamma\gamma} \gtrsim 70$ GeV. In the comparable range the data is compatible with both PYTHIA and PYTHIA ND.*

The $\gamma\gamma$-combination is required to lie within 4 standard deviations $\sigma_{\mathbb{O}I\!\!PIUM}$ of the Gaussian distribution:

$$\boxed{|M_{\gamma\gamma} - M_{\pi^0}| < 4\sigma_{\mathbb{O}I\!\!PIUM}} \tag{5.47}$$

with

$$M_{\pi^0} = 135 \text{ MeV} \tag{5.48}$$

and

$$\sigma_{VS} = 18 \text{ MeV} \qquad , \qquad \sigma_{VV_i} = 12 \text{ MeV} \qquad , \qquad \sigma_{VV_d} = 18 \text{ MeV} \ . \tag{5.49}$$

The different standard deviations in (5.49) are due to the different resolutions in the calorimeters. Especially the last case in (5.49) is limited by statistics (see figure 5.16 and 5.17). Figure 5.9 shows the invariant mass spectra of the two photon candidates for data after the respective cuts for the three different event signature classes.

5.5 Simulation of the Forward Beam Line and the FNC

The data event selection cuts for the leading neutron are given in section 5.4.3. In order to have comparable data and Monte Carlo samples, the same cuts have to be applied to the

DATA

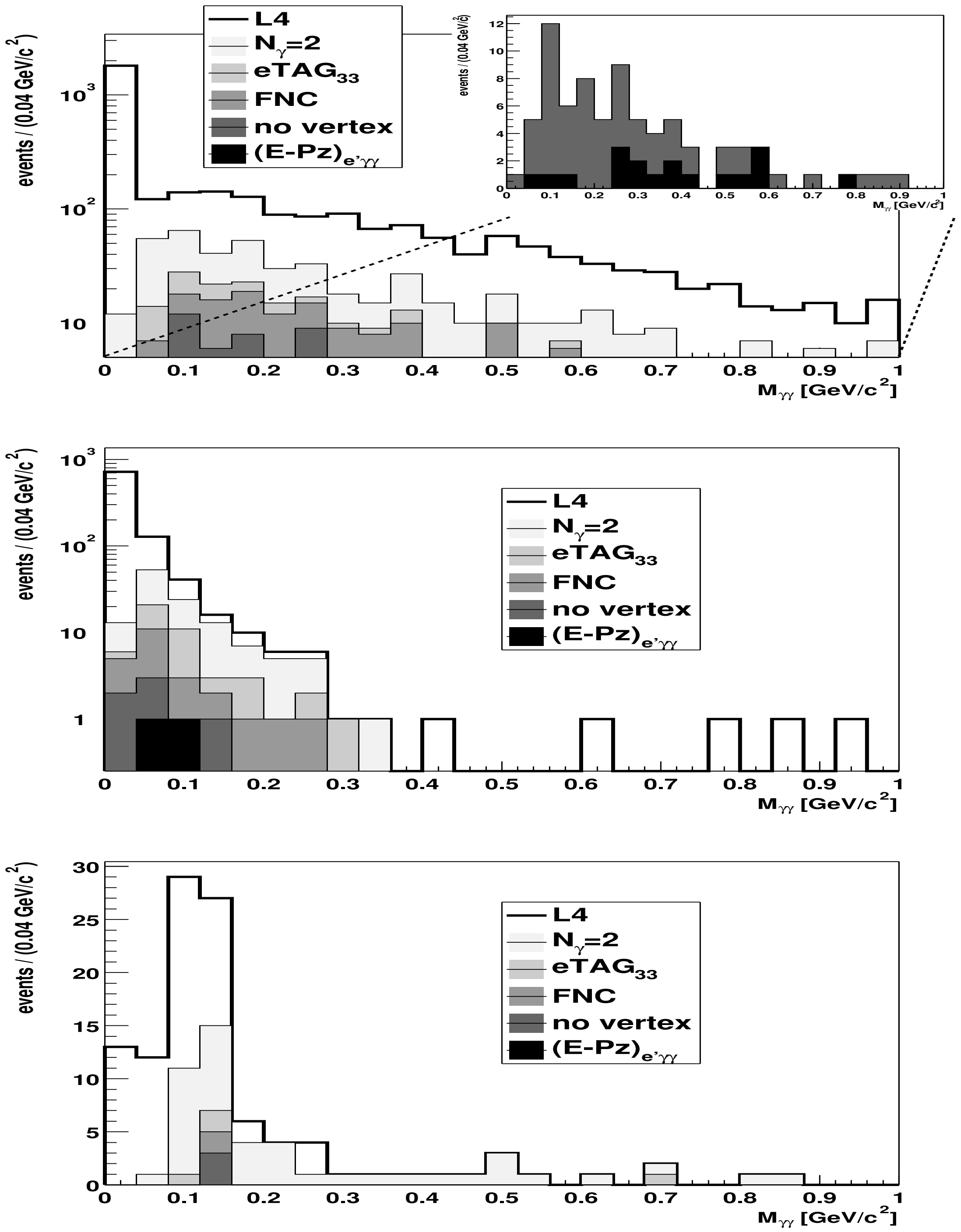

VS

VV_i

VV_d

Figure 5.9: *The $M_{\gamma\gamma}$ spectra for the three event classes: One photon in the VLQ and one in the Spacal (VS, top plot), both photons in the identical VLQ-module (VV_i, centre plot), one photon in the top and one in the bottom VLQ-module (VV_d, bottom plot). The expressions in the legends can be assigned to the cuts explained in the text: L4 (5.22), $N_\gamma = 2$ (respective cuts in section 5.4.1), $eTAG_{33}$ (cuts in section 5.4.2), FNC (cuts in section 5.4.3), no vertex (5.45), $(E - Pz)_{e'\gamma\gamma}$ (5.46).*

simulated events. It is crucial to know the selection efficiencies, especially for the determination of the cross section (equation (5.54)). However, the Monte Carlo samples demand a special treatment which originates from two facts: The official H1 simulation tool provides neither the simulation of the FNC, nor the simulation of the beam line.

The determination of the number of Monte Carlo generated neutrons in the FNC is performed in such a way that the cuts from section 5.4.3 are applied on generator level[3] and the respective efficiencies are taken into account in terms of an event weight.

5.5.1 The Geometric Acceptance of the FNC

The neutrons originating from the nominal interaction point have to move along the beam pipe to reach the FNC (see section 2.5). Therefore the acceptance region of this calorimeter for the detection of neutrons is mainly restricted by the apertures of the proton beam line elements between the interaction point and the FNC. Figures 5.7 (a)-(c) show the spatial distribution of the reconstructed impact points in the FNC-plane after the respective neutron cuts from section 5.4.3, but before the cut on the acceptance region. Apart from a slight bump in the upper part of the figure, originating from deflected protons, a sharply cut off region can be identified. At the edge of this region, the neutron's trajectory crosses a (bending or focusing) magnet so that the neutron is absorbed, and the acceptance vanishes. In [NUN99] the acceptance has been evaluated in Monte Carlo studies using the LEPTO [ING97] event generator and a GEANT [GEA93] simulation of the proton beam line [LIS97]. Figure 5.10 shows the acceptance as a function of the position of the impact point; the superimposed curve describes the region in which the acceptance is nearly uniform and amounts to approximately 90%.

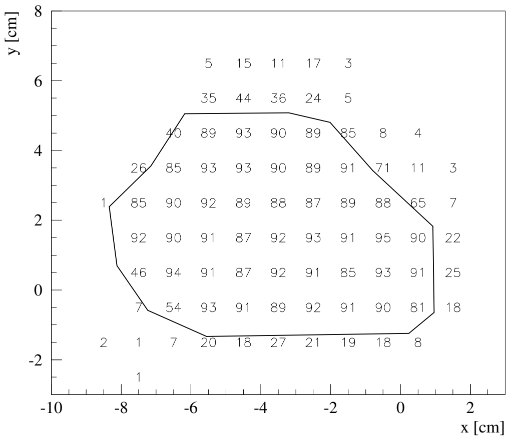

Figure 5.10: *Acceptance of the FNC as a function of the impact point position evaluated with a LEPTO Monte Carlo. The numbers in the figure denote the acceptance in a x-y-bin in percent. The superimposed curve indicates the edge of the acceptance region [NUN99].*

Comparing figure 5.10 with figure 5.7 (c) shows that the shape of the acceptance region is quite well described. However, the two shapes are shifted with respect to each other.

[3]The term "generator level" denotes the four-momenta of the particles before the detector simulation.

A parametrisation of the acceptance shape in figure 5.10 is adjusted to the data under consideration in figure 5.7 (c). In figure 5.7 (d) the impact points are required to lie within this area.

5.5.2 The Determination of the Origin in the FNC

The determination of the shape of the geometric acceptance region of the FNC can be taken from the beam line simulation in [NUN99], because the geometric acceptance depends only on the condition of the beam pipe which has not changed considerably between the study in [NUN99] and the data taking period considered in this analysis. In contrast, the origin, which is the point where the z-axis of the H1 coordinate system meets the FNC, must be determined according to the actual data. The above mentioned shift of the acceptance region indicates differences in the FNC positioning with respect to the H1 coordinate system. This effect could be due to a shift of the calorimeter. This would suggest the use of the origin determined in [NUN99] and to re-position it according to the shift of the acceptance region. However, there can be additional reasons for a shift of the origin, for example a proton beam tilt by a fraction of 1 mrad, or another reconstruction routine. Further, since the beginning of 1999 a new preshower detector has been in use.

The cross section for the production of leading neutrons decreases with increasing scattering angle, therefore there should be a maximum density of impact points where the H1 z-axis meets the FNC. Consequently the spatial point with the maximum observed rate could be most easily used to redefine the direction of $\theta = 0°$ in the data. However, as can be seen in figure 5.11 two maxima are observable (which are not correlated with time). This two-peak structure can be explained by a miscalibration [BUN00] of the FNC's Spacal part. Neutrons pass through the preshower detector without interaction, and start showers in the Spacal part. As a result, the structure of the detector modules is visible in the xy hit distribution of the FNC. The effect is caused by the fact that the lateral shower dimensions are small compared to the granularity. The work on the calibration is still in progress and is not yet finished for use in this analysis. In [ACO91a], the effect of the displacement is illustrated and is of the same order of magnitude as in figure 5.11. The left and right peak are determined to have the coordinates:

$$(x_1^{FNC}, y_1^{FNC}) = (-1.2, -2.8) \qquad \text{and} \qquad (x_2^{FNC}, y_2^{FNC}) = (1.9, -2.8), \tag{5.50}$$

from which the averaged origin is chosen to be the geometric centre:

$$(x_{FNC}, y_{FNC}) = (0.4, -2.8). \tag{5.51}$$

In the Monte Carlo event samples the spatial distribution of impact points is shifted by the vector of equation (5.51) so that the 0°-points coincide.

5.5.3 Treatment of the Monte Carlo Neutron in the FNC

The neutron flies along the beam line, leaves the beam pipe at 93 m and hits the FNC at 107 m. Only neutrons reaching the FNC in the acceptance region, i.e. neutrons passing the elements of the beam pipe, are accepted. The impact point is smeared with a Gaussian

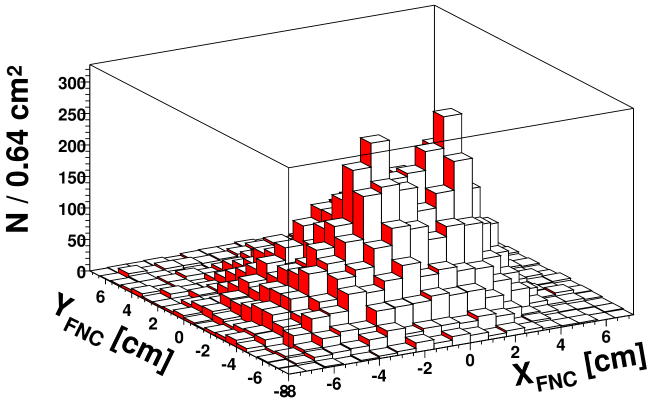

Figure 5.11: *A lego plot of the reconstructed clusters in the xy-plane in the FNC. The two-peak structure according to the miscalibration of the FNC (see text) can be seen clearly.*

distribution according to the spatial resolution of the FNC (see equation (2.4)), and neutrons migrated out of the acceptance region are rejected. The energy resolution is taken into consideration by smearing the energy according to a Gaussian distribution (equation (2.3)), after which the energy cut (5.43) is applied. Figure 5.12 shows the xy-distribution of the impact points of the $\mathbb{O}\mathbb{P}$IUM-neutrons in the FNC after the relevant cuts.

5.5.4 Efficiencies and Background for the Detection of Leading Neutrons

Within the region cut out by the beam line apertures the acceptance is 90% [NUN99] (see figure 5.10).

In order to veto charged particles, two segmented planes of hodoscopes situated in front of the FNC (see section 2.5) are used. In the course of the neutron's hadronic shower development, charged particles can be produced, which scatter back and coincide in the veto hodoscopes. This results in a neutron detection efficiency of the FNC of (93±5.4)% [H1D99].

On the other hand charged particles can survive the veto of the two hodoscopes. In [MET98], the response of a hodoscope plane was determined using the other plane to trigger on charged particles. The combined efficiency of the two hodoscopes amounts to over 99.5% [NUN99]. As discussed in [NUN99], the fraction of charged particles over the total rate of particles hitting the acceptance region of the FNC contributes to approximately 5% in DIS reactions. Due to the proton breakup in DIS a larger hadronic activity is expected than in the regarded N^* production. Therefore the 5% can be considered as a conservative estimate. This amounts to a contamination of the data with charged particles of 0.025%.

An additional source of background originates from other neutral particles (mainly photons and K_L^0). This contribution heavily depends on the compensation of the calorimeter, which is defined as the ratio of the calorimeter's response to the electromagnetic part of the shower over the response to the hadronic part (e/h). It is preferable to have a compensation ratio close to one which has the advantage that the energy calibration is independent of the

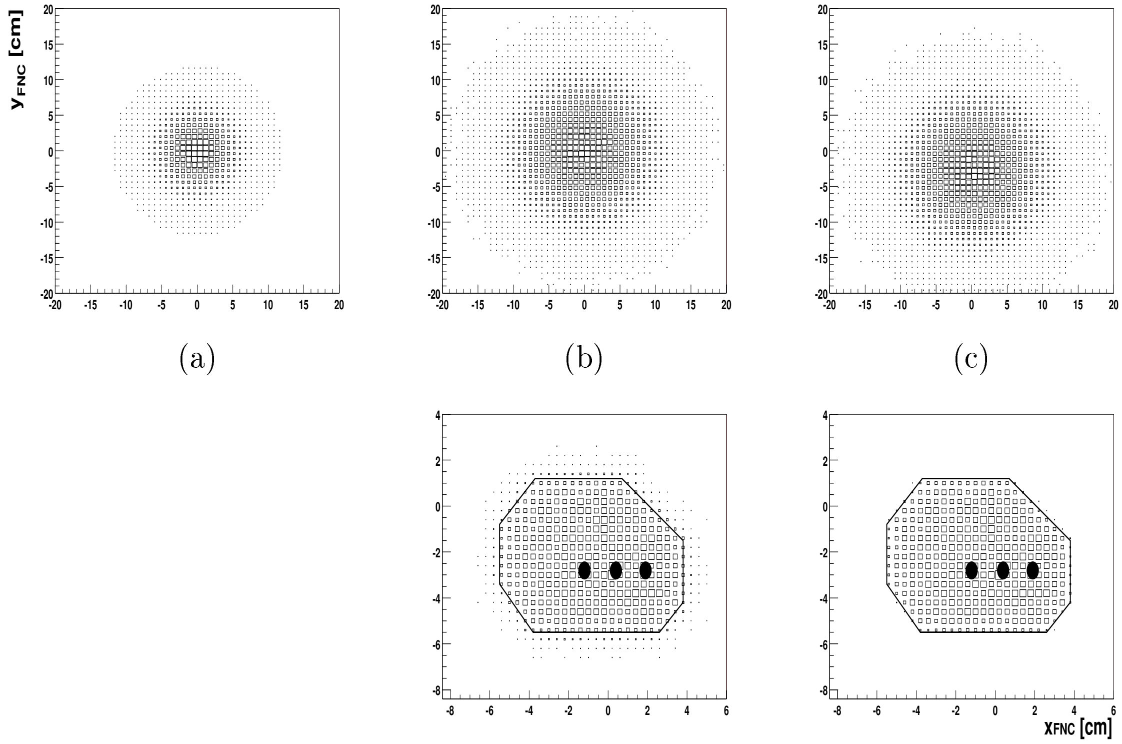

(a) (b) (c)

(d) (e)

Figure 5.12: *In comparison to figure 5.7 and figure 5.11, the hits of the OPIUM-neutrons, generated as discussed in section 4.2.1, are shown in a plane through the FNC perpendicular to the beam axis. Part (a) shows the impact points of the N^*, (b) the neutrons from the N^* decay and (c) the shift to the new origin (5.51). In (d) the acceptance region is cut out and subsequently the impact points are smeared with a Gaussian according to the spatial resolution in the FNC given in (2.4). Plot e) shows the remaining events after rejecting the migrated neutrons. The centred black dot in the plots (d) and (e) represents the data-corrected origin (5.51), the two dots aside mark the two peaks in figure 5.11 and equation (5.50), respectively.*

regarded particle. For the FNC $e/h = 1.15 \pm 0.02$ [ACO91]. Since the energies of the photons are smaller than the nucleons' energies, the background depends on the variable $\mathcal{Z} = E'_n/E_p$. In [NUN99], an estimate of 6% for DIS reactions is given for events with $\mathcal{Z} > 0.2$, 3% for $\mathcal{Z} > 0.4$, and 2% for $\mathcal{Z} > 0.6$.

5.6 Acceptance of the Signal

Neutron Acceptance in the FNC

Both the trigger efficiency of the FNC trigger element and the acceptance of the neutron in the FNC are already discussed in section 5.1.1 and section 5.5, respectively.

Electron Acceptance in the eTAG$_{33}$

The acceptance and efficiency of the scattered electron in the eTAG$_{33}$ are shown in figure 5.1. Only events within the acceptance region of the electron detector were generated and thus, taken into account. To estimate the migration at the edges of the y-acceptance region according to the energy resolution, events were generated in a y-range at the lower and the upper edge of the acceptance region: $0.19 < y < 0.3$ and $0.7 < y < 0.76$ – see figure 5.13 (a). The ranges correspond to three standard deviations of the eTAG$_{33}$ energy resolution. Plots (b) and (c) in figure 5.13 show the y-distributions after the respective photon selection cuts from section 5.4.1 and after weighting with the y-efficiency from figure 5.1. This results in an effective migration into the acceptance region of +3.5% for the case VS, and +0.2% for the case VV$_i$.

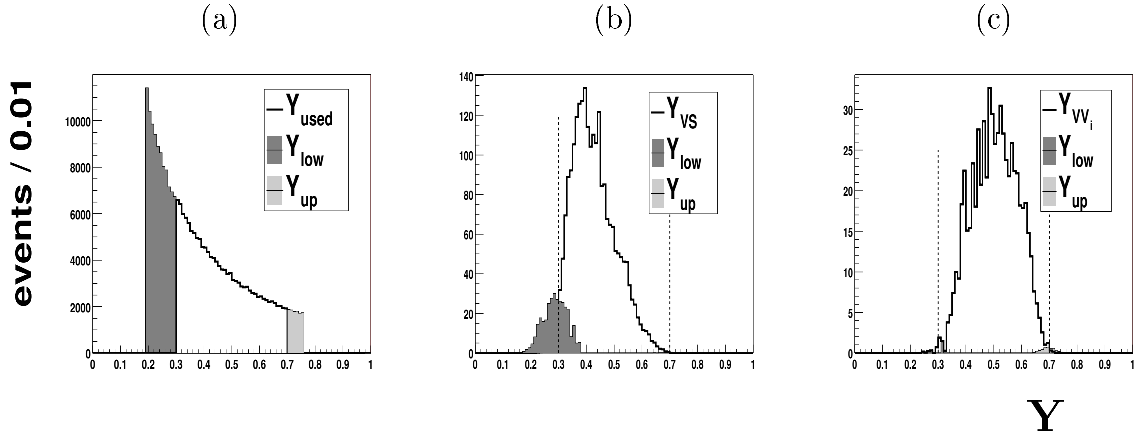

Figure 5.13: *Plot (a) shows the generated y-distribution from 0.19 to 0.76. The shaded areas are normalised to the y-region from 0.3 to 0.7. Applying the y-efficiency weighting and the corresponding photon selection cuts leads to the distributions depicted in plot (b) and (c). The index in the legends denotes the respective event class: VS for "VLQ-Spacal" and VV_i for "VLQ identical module". The VV_d class is not considered due to the small acceptance.*

Pion Acceptance for the Different Event Classes

In this section the acceptance for pions for the three different calorimeter configurations of the Spacal and the VLQ are determined.

Figure 5.14 shows the pion acceptance

$$\frac{N^{rec}_{\pi^0}(\Delta E)}{N^{gen}_{\pi^0}(\Delta E)} \tag{5.52}$$

as a function of the pion energy E_{π^0} for the different event classes. $N^{gen}_{\pi^0}(\Delta E)$ is the number of π^0s generated in the interval $(E_{\pi^0}, E_{\pi^0} + \Delta E)$ and $N^{rec}_{\pi^0}(\Delta E)$ marks the number of π^0s identified after applying the event selection cuts from section 5.4.1 in the same energy range $(E_{\pi^0}, E_{\pi^0} + \Delta E)$ in which the π^0s were generated. The dead material between the Spacal and the VLQ (see figure 5.3) requires an opening angle of the two photons larger than roughly

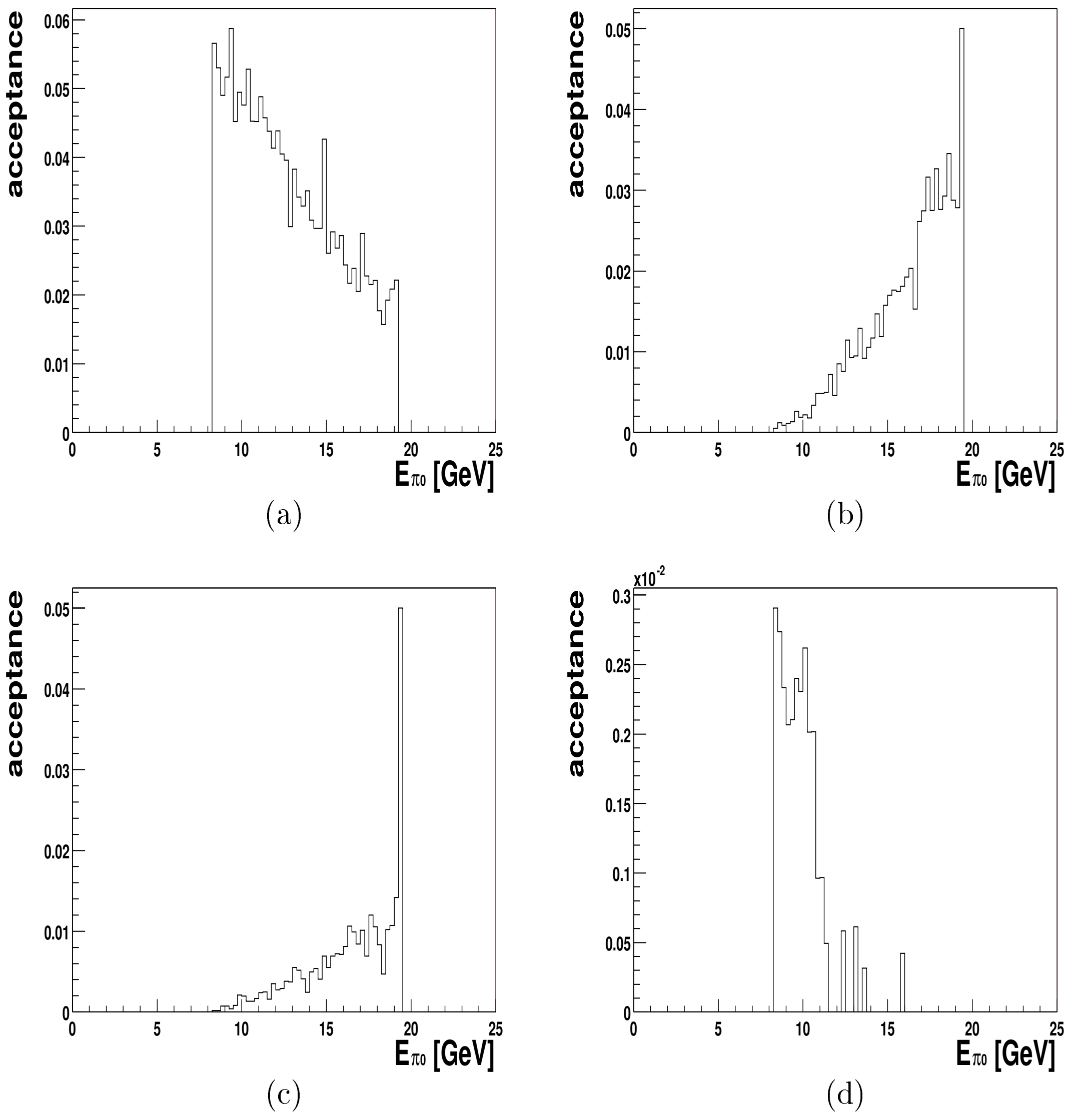

Figure 5.14: *The pion acceptance depending on the pion energy is shown for four signatures: (a) one photon in the VLQ, one in the Spacal, (b) both photons in the VLQ top module, (c) both photons in the bottom module, (d) one photon in the top and one in the bottom module.*

22 mrad, whereas there is virtually no limit for large opening angles (figure 1.20). This favours small pion energies as seen in figure 5.14 (a). The reverse is true for the case of two photons in the same module – 5.14 (b),(c) – where the opening angle is limited by the size of a module so that large pion energies are preferentially selected. The different acceptance for the top and the bottom module is due to the P_t-distribution of the pions – figure 4.1 (d) – and the different distance of the two modules from the beam pipe. For pion energies of about 12 GeV, the minimum distance of the two photons in a plane through the VLQ perpendicular to the beam axis becomes larger than the distance of the two VLQ-modules. As a consequence, the acceptance in plot 5.14 (d) rises sharply.

An overview over all acceptances is given in table 5.2. Beside the described cuts, each event accepted by the selection criteria has been weighted according to the trigger and reconstruction efficiencies of the FNC and the electron tagger, the subdetectors not simulated by the official H1 simulation. Table 5.1 summarizes these efficiencies. In figure 5.15 the $M_{\gamma\gamma}$ spectrum is shown for the pions from $\mathbb{OP}$IUM after the respective cuts in section 5.4.

For the determination of an upper limit for the cross section, the case in which both photons hit different VLQ modules is excluded for acceptance reasons.

description		efficiency
eTAG$_{33}$ trigger efficiency	(5.4)	$\epsilon_{eTAG}(y)$
FNC trigger efficiency *99-1* *99-2*	 (5.7) (5.8)	 $\epsilon_{FNC_{99-1}}(E_{FNC})$ $\epsilon_{FNC_{99-2}}(E_{FNC})$
acceptance within the cut out region in the FNC	section 5.5.4	0.9
neutral particle detection efficiency in the FNC	section 5.5.4	0.93
migration at the edges of the y acceptance region	section 5.6	1.035 (VS) 1.002 (VV_i)

Table 5.1: *Summary of the efficiencies and correction values.*

5.7 Systematic Errors

Beside general systematic errors, the uncertainties can be divided into three different types:

1. errors which depend on the final state neutron
2. errors which are due to the scattered electron
3. systematic uncertainties concerning the detection of the two photons from the pion decay.

Due to the small number of observed events, the results and in particular the determination of an upper limit (as discussed in detail in section 5.9) on the Odderon exchange, will be dominated by the statistical error. Nevertheless, systematic uncertainties have to be considered.

cut		#	ϵ_i [%]	$\prod_i \epsilon_i$ [%]
reference: $\substack{y\in(0.3,0.7)\\ Q^2<0.01\,\mathrm{GeV}^2}$	(5.36),(5.37)	*104121		

VLQ Spacal				
L_4	(5.9),(5.10)	8411.0	8.08	8.08
$N_\gamma = 2$	(5.26)-(5.28), (5.33)-(5.35)	3765.0	44.76	3.62
eTAG$_{33}$ efficiency	figure 5.1	1613.0	42.83	1.54
FNC	trigger eff. fig. 5.2,(5.40)-(5.44), with n from section 4.2.1	77.2	4.79	$7.41\cdot10^{-2}$
49 GeV $< (E-P_z)_{e'\gamma\gamma} <$ 60 GeV	(5.46)	67.5	87.39	$6.48\cdot10^{-2}$
$M_{\gamma\gamma}$ window	(5.47)	67.2	99.63	$6.46\cdot10^{-2}$

VLQ VLQ Identical module				
L_4	(5.9),(5.10)	2028.0	1.95	1.95
$N_\gamma = 2$	(5.24),(5.27), (5.30),(5.32)	1461.0	72.04	1.40
eTAG$_{33}$ efficiency	figure 5.1	481.1	32.93	$4.62\cdot10^{-1}$
FNC	trigger eff. fig. 5.2,(5.40)-(5.44), with n from section 4.2.1	23.7	4.92	$2.27\cdot10^{-2}$
49 GeV $< (E-P_z)_{e'\gamma\gamma} <$ 60 GeV	(5.46)	20.0	84.69	$1.92\cdot10^{-2}$
$M_{\gamma\gamma}$ window	(5.47)	19.9	99.35	$1.91\cdot10^{-2}$

VLQ VLQ Different modules				
L_4	(5.9),(5.10)	160.2	$1.54\cdot10^{-1}$	$1.54\cdot10^{-1}$
$N_\gamma = 2$	(5.25),(5.27)	98.7	61.60	$9.48\cdot10^{-2}$
eTAG$_{33}$ efficiency	figure 5.1	35.8	36.28	$3.44\cdot10^{-2}$
FNC	trigger eff. fig. 5.2,(5.40)-(5.44), with n from section 4.2.1	1.6	4.51	$1.55\cdot10^{-3}$
49 GeV $< (E-P_z)_{e'\gamma\gamma} <$ 60 GeV	(5.46)	1.4	87.99	$1.36\cdot10^{-3}$
$M_{\gamma\gamma}$ window	(5.47)	1.4	100.00	$1.36\cdot10^{-3}$

Sum of the VS and VV_i event classes		
all cuts	87	$8.40 \pm 0.10(\mathrm{stat}) \cdot 10^{-2}$

Table 5.2: *The table summarizes the cuts applied to the event sample generated with $\mathbb{O}$I PIUM. For reasons of better readability, the events are logically grouped. For each event class, the number of events after each cut, the cut efficiency and the overall efficiency is given.*
* *The event numbers are gained from a total of 143909 generated events. Normalisation to integrated luminosity is applied.*

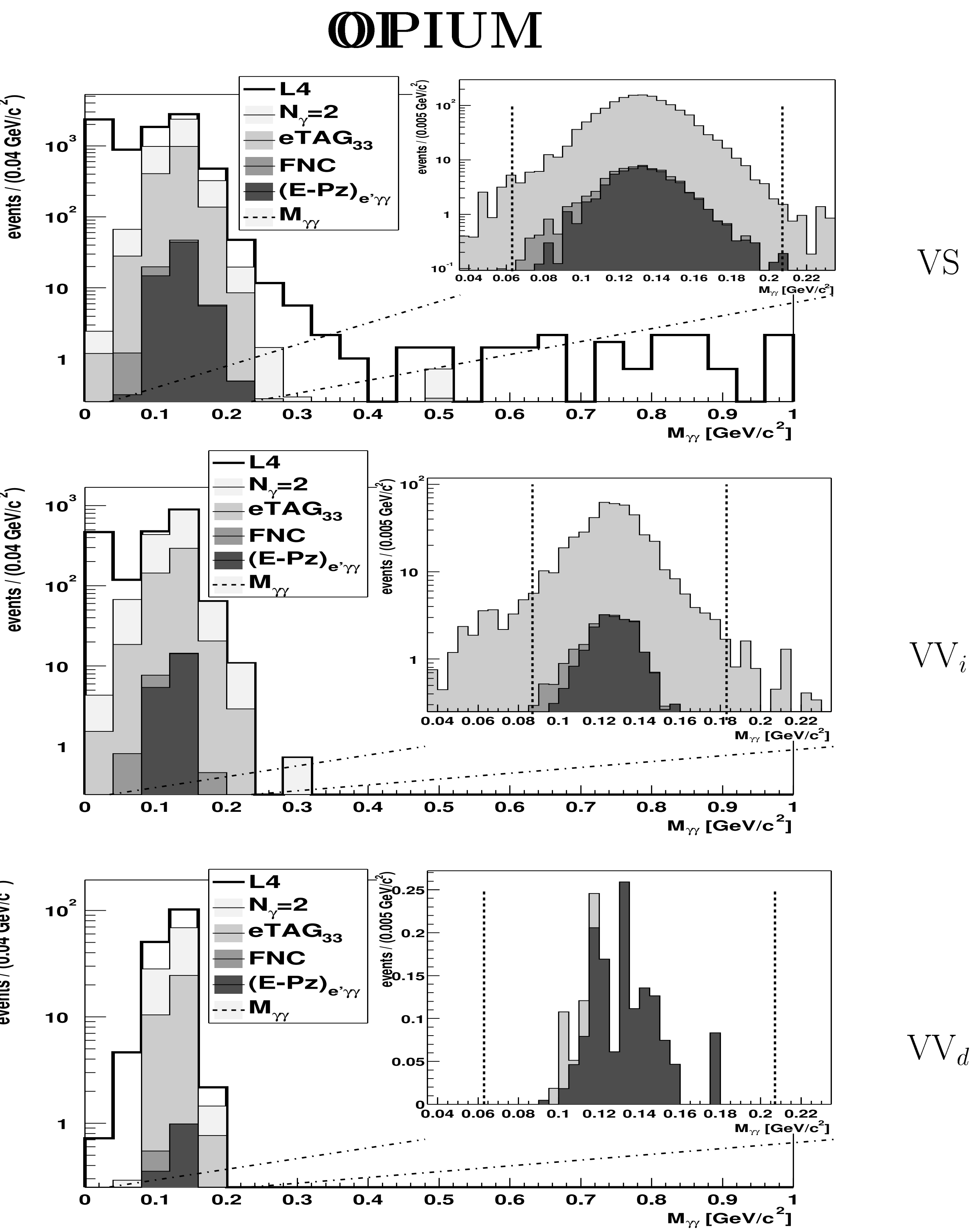

Figure 5.15: *The $M_{\gamma\gamma}$ spectra are shown for the pions from* $\mathbb{O}\mathbb{P}$*IUM for the three event classes (top down:VS, VV_i, VV_d) and can directly be compared to figure 5.9. The cuts are explained in section 5.4 and the corresponding cut efficiencies are specified in table 5.1 and table 5.2.*

Systematic Errors of the Final State Neutron

- **Systematic error on the neutron detection efficiency: 5.4%**, see section 5.5.4.
- In section 5.5.4 the **contamination of the data with charged particles** was determined to be **0.025%**.
- The **contamination of the data with neutral particles other than neutrons** was determined by weighting the neutron energy distributions for *99-1* and *99-2* with the $\mathcal{Z}$-values from section 5.5.4. The mean of the two systematic errors, weighted with the integrated luminosities for *99-1* and *99-2*, results in **2.5%**. The $\mathcal{Z}$-values hold for DIS where the number of particles is large due to hadronisation so that the error is assumed to be overestimated for the reactions under investigation in this analysis.
- **Uncertainty of the origin in the FNC:** The origin was shifted to the two peaks in (5.50) and the acceptance was determined. This corresponds to an increase of 9% and a decrease of 12%, respectively. The final error is averaged by $\Delta = \frac{|\Delta^+ - \Delta^-|}{2}$, which yields **10.5%**.
- In section 5.5.4, the acceptance within the cut out region was stated to be 90%. The **uncertainty of the averaged acceptance on the perceivable "plateau"** is estimated by taking the variance of the mean of all bins in the acceptance region in figure 5.10 (not taking into account the two values smaller than 60%). This yields an error of **2%**.
- In section 5.5.1, it was shown that the acceptance region of the FNC had to be shifted for the considered data compared to figure 5.10. The systematic error due to the **uncertainty of the correct position of the acceptance region** was estimated by shifting the plateau in figure 5.10 by one bin (equivalent to 1 cm) in the x and y-direction. This results in a mean error of **9.5%**.

Systematic Errors of the Scattered Electron

- **Energy scale uncertainty of the electron tagger:** As mentioned in 5.1.1 the efficiency of the eTAG$_{33}$ is taken into account for each event individually. A systematic error of the efficiency arises due to the uncertainty of the absolute energy scale of the electron tagger. Varying the electron energy by 1.5% results in a variation of **4%** for data collected in 1996 [SWA00]. Since the final numbers for the efficiency for the data taking period 1999 have not yet been supplied, the value from [SWA00] can be taken as the best available estimate [LEV00].

Systematic Errors of the Photon Detection

- The two modules of the VLQ are not always placed at the same distance away from the beam pipe. **The displacement of the VLQ in x and y** is shown to reach values up to 1 mm [KLU00]. Due to the steep t-distribution, this strongly affects the acceptance of the $\mathbb{O}\mathbb{P}$IUM signal. As an estimate, the geometry of the VLQ was simulated on software level and shifted by one millimeter in the x- and y-direction. The systematic uncertainty was defined as the difference in the number of hits on generator level in the shifted acceptance regions for the respective event classes. The VS class is much less dependent on the position of the VLQ than the VV classes and is reflected in the errors: 2% for VS, 10.8% for VV_i (11.5% for VV_d). Weighting with the corresponding acceptances from table 5.2 yields a systematic error of **4.2%**.

- The **uncertainty of the energy scale** of the Spacal in the considered energy range is determined to be around 4% [SWA00]. Calibration of the VLQ with 12 GeV kinematic peak electrons gives reason to assume the uncertainty of the energy scale of the VLQ to also be of the order of 4%. By varying the reconstructed cluster energies by 4% and applying the cut criteria from section 5.4 **one event is lost in the VS class**.

General Systematic Errors

- The **luminosity** for the considered data is determined to a precision of **1.5%** according to the official H1 summary table.

- **Radiative corrections** are not taken into account. They are expected to have a marginal effect on the energy spectrum of the pions and of the detected electrons.

- **Contributions of π^0s due to beam-gas events** are determined via the expression [SWA00]:

$$\Delta_{BG} = \frac{I_{ebeam} + I_{pilot}}{I_{pilot}} \cdot \frac{N_{pilot}}{N_{ebeam} + N_{pilot}}, \tag{5.53}$$

where I_{ebeam} and I_{pilot} denote the currents of the electron beam and the pilot bunches, respectively, and N the number of events. The systematic uncertainty Δ_{BG} results in **9%**.

5.8 The Final $M_{\gamma\gamma}$ Spectra

Figures 5.16 and 5.17 show the spectrum of the invariant mass of the two photons for each event class and for the sum of all event classes after all cuts. Apart from the case VV_d where no statement can be made due to the low statistics, a signal of approximately 87 events is expected for the given luminosity from ℗PIUM. Yet, only four events in the data survive the applied cuts and are compatible with background expectations, both with the default *PYTHIA* sample and with the *PYTHIA ND* sample where the "diffractive states" are excluded.

Figure 5.18 shows the energy, transverse momentum and t distributions of the remaining pions and compares them with the ℗PIUM and PYTHIA predictions.

5.8.1 Background

The remaining event samples in figures 5.16 and 5.17 are almost free from background, and therefore the possible background sources are only enumerated:

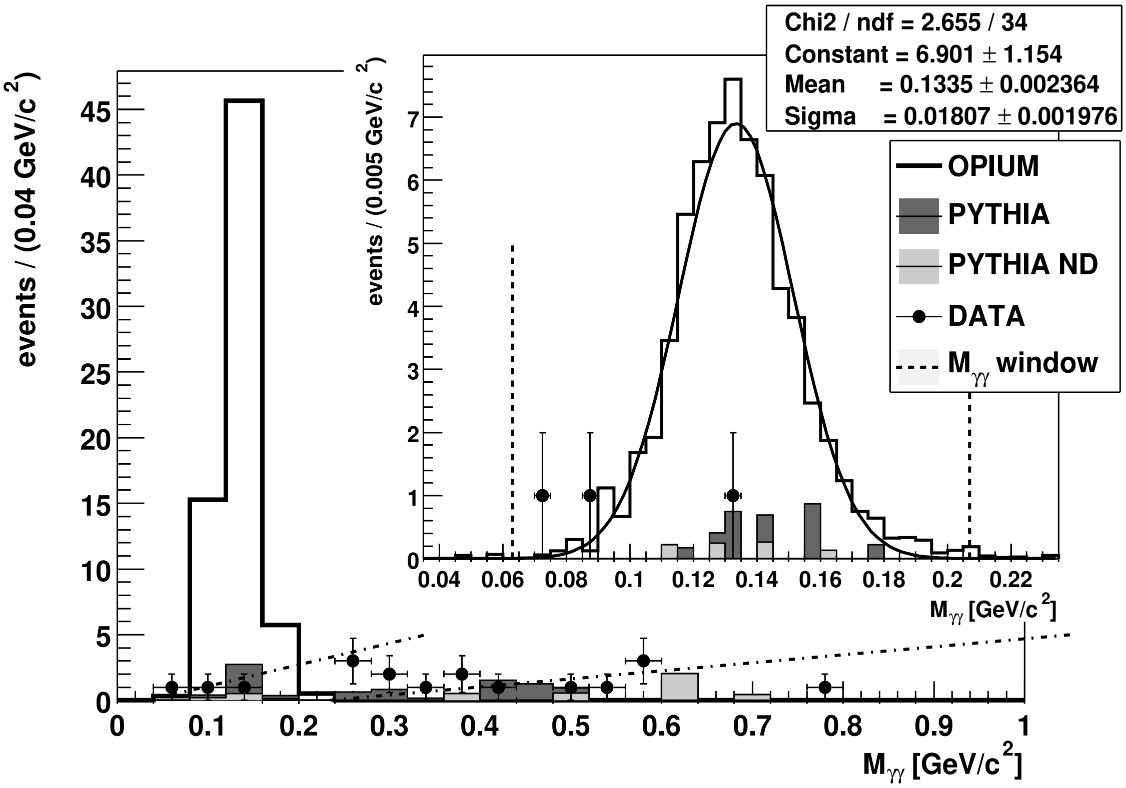

VS

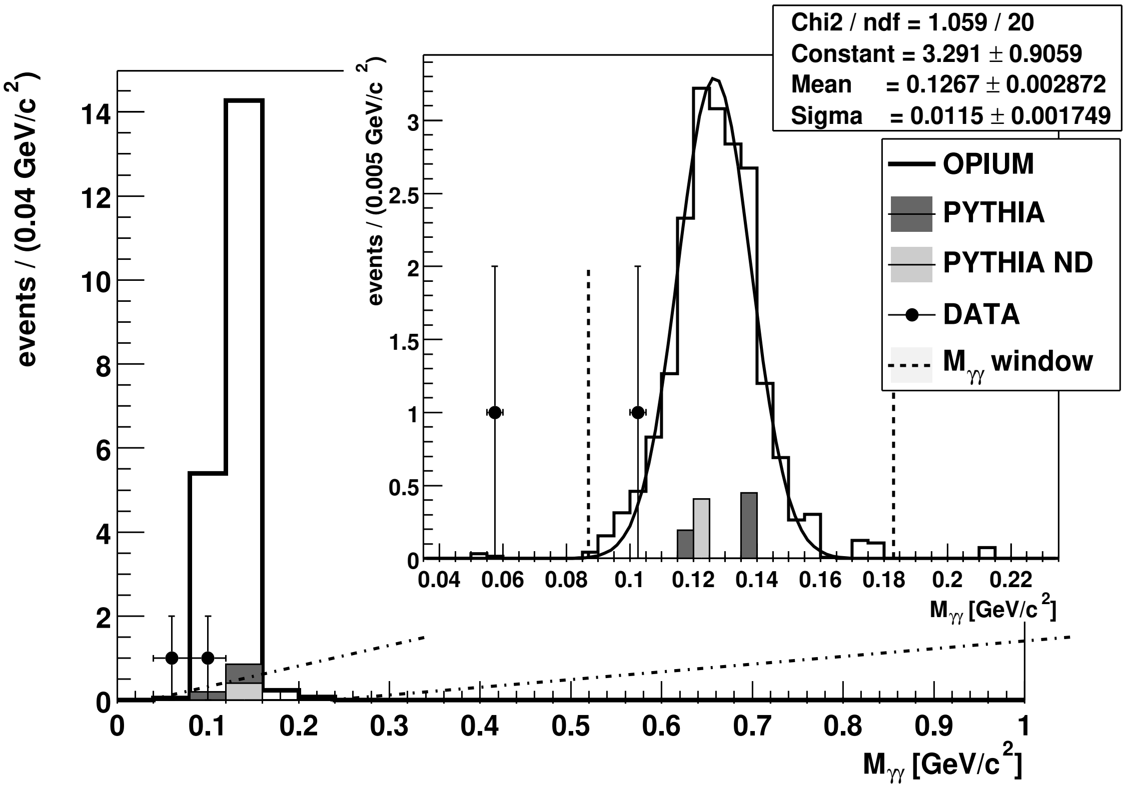

VV_i

Figure 5.16: *The $M_{\gamma\gamma}$ spectrum after all cuts for the VS (top) and the VV_i (bottom) case for data, 𝕆ℙIUM and PYTHIA.*

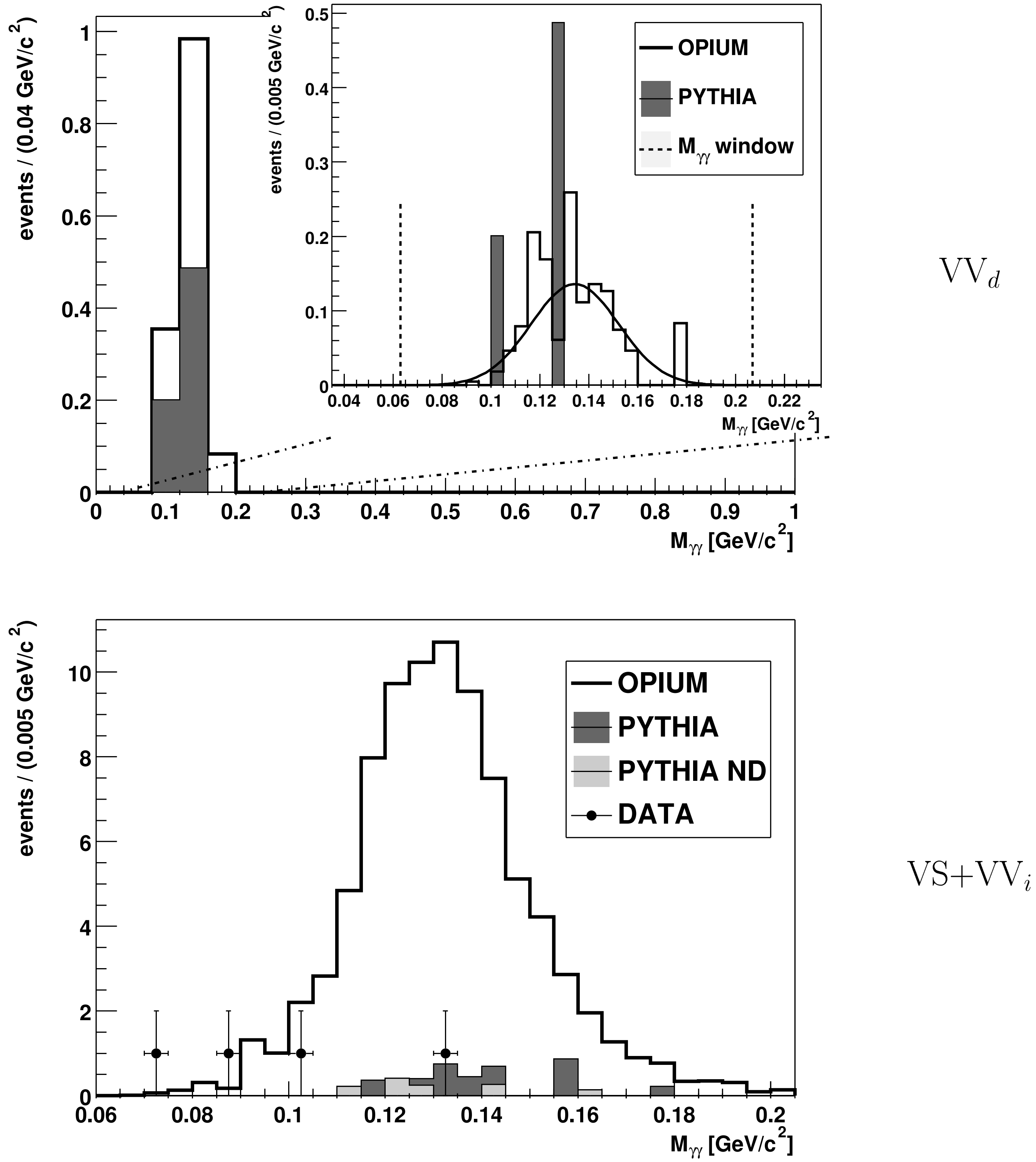

Figure 5.17: *The $M_{\gamma\gamma}$ spectrum after all cuts for the VV_d case and the sum of VS and VV_i for data, 𝕆PIUM and PYTHIA. The determination of the upper limit for the cross section is based on the bottom plot.*

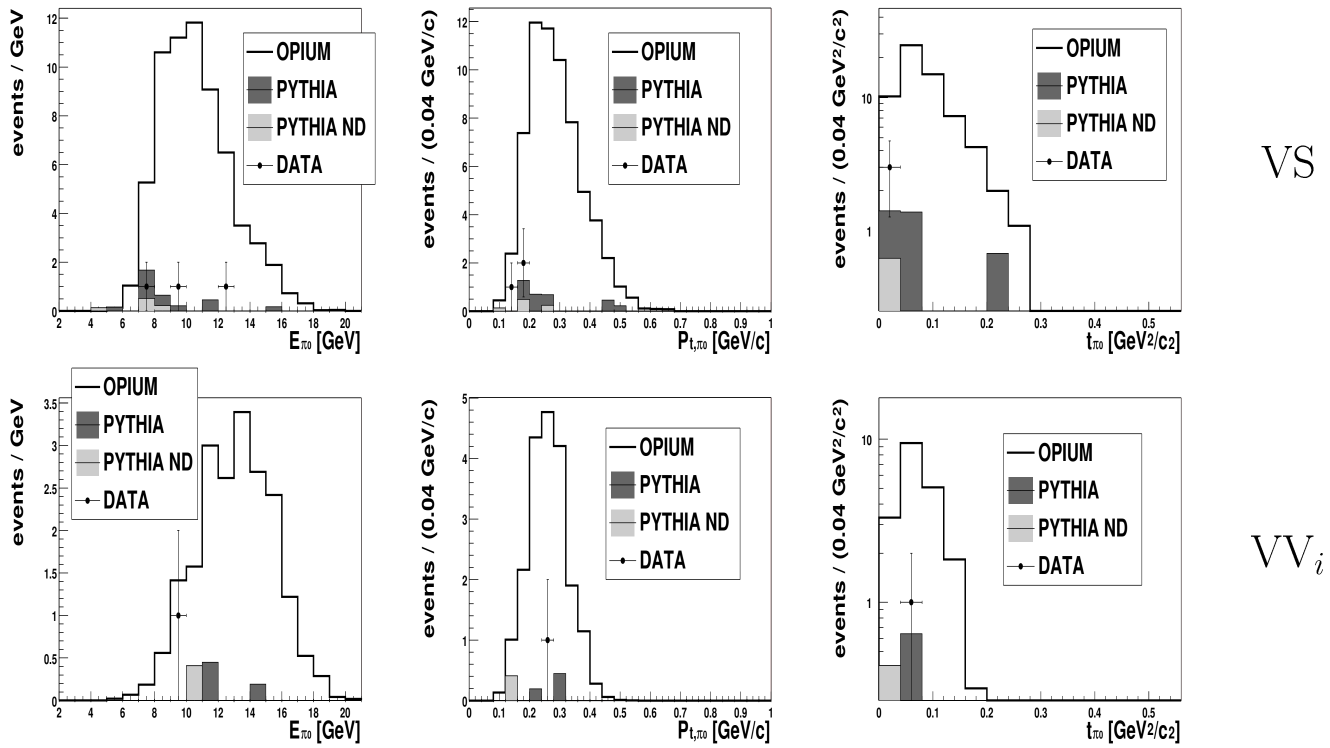

Figure 5.18: *The energy, transverse momentum and t spectra for the pions. The top plots depict the VS case, while the lower show the VV_i case.*

- As can be seen from figure 5.4 (e), most of the ω's and ρ^0's do not contribute to the pion mass range of the dominating VS class. The best part of the $\gamma\gamma$-combinations contains the "lonely photon" not originating from the pion decay and thus, the reconstructed mass is larger than the pion mass.

- Contributions from the Primakov effect, the photon-photon-fusion, are negligible. Assuming an acceptance of the same order of magnitude as the Odderon-photon-fusion, 0.04 events are expected from the cross section in table 1.1. This is already conservative since the transverse momenta of the produced pions peak at 0 GeV/c (right plot in figure 1.19). Further, the acceptance disappears for $P_{t,\pi^0} \to 0$ (centre plots in figure 5.18) as the pions escape through the beam pipe.

- The greatest part of the background comes from high-energetic inclusive pions [SWA00] which survive the exclusive cuts in 5.4.4. This can be traced to the fact that the H1 tracking system (section 2.6) does not cover the whole solid angle and that particles with an energy below a certain threshold cannot be detected. Due to resolution effects, the $(E - P_z)$ cut cannot be tightened in order to reject these events.

5.9 Determination of the Cross Section $\gamma p \xrightarrow{\mathbb{O}} \pi^0 N^*$

The cross section for the reaction $ep \to e\pi^0 N^*$ in the photoproduction regime is given by:

$$\sigma(ep \to e\pi^0 N^*) = \frac{1}{\epsilon_{trigger} \cdot \epsilon_{selection} \cdot BR_{\pi^0 \to \gamma\gamma} \cdot BR_{N^* \to nX}} \cdot \frac{N_{observed}}{\int \mathcal{L}\,\mathrm{d}t}\,, \qquad (5.54)$$

where the π^0 is detected by its two decay photons, one in the VLQ and one in the Spacal or both in one VLQ module. Here $N_{observed}$ denotes the number of events measured after all selection cuts. The integrated luminosity is given by $\int \mathcal{L}\,\mathrm{d}t$ and BR_{π^0} and BR_{N^*} are the branching ratios for the decay of the pion in two photons and the decay of the excited proton in a neutron and a hadronic part, respectively. $\epsilon_{trigger}$ denotes the efficiency of the trigger used (*S96*), and all further efficiencies are summarized in $\epsilon_{selection}$, including the geometric acceptance and the reconstruction efficiencies of the subdetectors as well as the efficiencies of all applied cuts. In table 5.3 all numbers necessary for the determination of the cross section are summarized. The number of events $N_{observed}$ is shown in the bottom plot in figure 5.17.

<table>
<tr><td>$N_{observed}$</td><td colspan="2">4</td></tr>
<tr><td>N_{PYTHIA}</td><td colspan="2">4.52</td></tr>
<tr><td>$N_{PYTHIA\ ND}$</td><td colspan="2">1.28</td></tr>
<tr><td>$BR_{\pi^0 \to \gamma\gamma}$</td><td colspan="2">0.99</td></tr>
<tr><td>$BR_{N^* \to nX}$</td><td>0.42</td><td rowspan="3">$8.40 \cdot 10^{-4}$</td></tr>
<tr><td>$\epsilon_{trigger}$</td><td>$4.1 \cdot 10^{-2}$</td></tr>
<tr><td>$\epsilon_{selection}$</td><td>$4.9 \cdot 10^{-2}$</td></tr>
<tr><td>$\int \mathcal{L}\,\mathrm{d}t$</td><td colspan="2">11.06 pb^{-1}</td></tr>
<tr><td>σ_{sys}</td><td colspan="2">0.19</td></tr>
</table>

Table 5.3: *Factors in the π^0-cross-section.*

The branching ratio $BR_{\pi^0 \to \gamma\gamma}$ is taken from [PDG00] and the efficiencies can be derived from table 5.2. Inserting all numbers in (5.54) and dividing this cross section by the photon flux factor c_{EPA} (see table 1.1) yields the γp cross section ($\sigma_{\gamma p} = \frac{\sigma_{ep}}{c_{EPA}}$):

$$\sigma_{\gamma p \to \pi^0 N^*} = 32.0 \pm 16.0\ (\mathrm{stat}) \pm 6.1\ (\mathrm{syst})\ \mathrm{nb}. \qquad (5.55)$$

In table 5.3 also the expected number of events from photoproduction N_{PYTHIA} and $N_{PYTHIA\ ND}$ are given (shown in the bottom plot in figure 5.17). As one can see, the measured number of events and thus the measured cross section (5.55) are compatible with the photoproduction prediction.

But the bottom plot in figure 5.17 also reveals that Odderon induced processes cannot be resolved. The number of events which may originate from Odderon induced processes results in the number of observed events minus the number of events which do not stem from Odderon induced processes but from other photoproduction processes, called $N_{background}$, which are given by PYTHIA. With the number of background events ($N_{background} = N_{PYTHIA},\ N_{PYTHIA\ ND}$)

the measured cross section for the reaction $ep \xrightarrow{\mathbb{O}} e\pi^0 N^*$ via Odderon-photon fusion is given by:

$$\sigma(ep \xrightarrow{\mathbb{O}} e\pi^0 N^*) = \frac{1}{\epsilon_{trigger} \cdot \epsilon_{selection} \cdot BR_{\pi^0 \to \gamma\gamma} \cdot BR_{N^* \to nX}} \cdot \frac{N_{observed} - N_{background}}{\int \mathcal{L}\, \mathrm{d}t} \;. \quad (5.56)$$

In order to verify the exclusion of the MSV and its predictions for the production of exclusive pions in Odderon-photon fusion, an upper limit on the cross section (5.56) is provided. In appendix A.3 a method is described that determines an upper limit for the number of events by an ordering principle based on likelihood ratios. The systematic uncertainty is taken into account by equation (A.8). The systematic errors are expected to be uncorrelated and thus, they can be determined by quadratic addition. The effect of incorporating the systematic

	95% confidence	99% confidence
μ_2(PYTHIA)	5.3	7.8
μ_2(PYTHIA ND)	8.5	11.0
μ_{2sys}(PYTHIA)	5.6	8.5
μ_{2sys}(PYTHIA ND)	9.3	12.5

Table 5.4: *Summary of the upper limits for the events observed before and after considering the systematic uncertainty (first two lines and last two lines, respectively). The values μ_2 are calculated by taking the two upper limits from the table in [COU98] that are closest to the pair $N_{observed}$ and N_{PYTHIA} (respectively, $N_{PYTHIA\,ND}$), linearly interpolating between these two values. μ_{2sys} is gained by feeding μ_2 to formula (A.8).*

error is seen in table 5.4. It is of the order of 10%. Together with the upper limit for the number of events of the signal μ_{2sys}, taken from table 5.4, the upper limit for the considered cross section can be calculated as:

$$\sigma_{ep \xrightarrow{\mathbb{O}} e\pi^0 N^*} < \sigma^{upper\ limit}_{ep \xrightarrow{\mathbb{O}} e\pi^0 N^*} = \frac{1}{\epsilon_{trigger} \cdot \epsilon_{selection} \cdot BR_{\pi^0 \to \gamma\gamma} \cdot BR_{N^* \to nX}} \cdot \frac{\mu_{2sys}}{\int \mathcal{L}\, \mathrm{d}t} \;. \quad (5.57)$$

Conservatively, the background sample yielding the higher limit (i.e. *PYTHIA ND*) is chosen for the final result and leads to

$$\begin{aligned} \sigma_{ep \xrightarrow{\mathbb{O}} e\pi^0 N^*} &< 1.01 \text{ nb} \qquad (95\% \text{ CL}) \\ \sigma_{ep \xrightarrow{\mathbb{O}} e\pi^0 N^*} &< 1.36 \text{ nb} \qquad (99\% \text{ CL}) \;. \end{aligned}$$

Dividing these cross sections by the photon flux factor c_{EPA} yields:

$$\begin{aligned} \sigma_{\gamma p \xrightarrow{\mathbb{O}} \pi^0 N^*} &< 74.3 \text{ nb} \qquad (95\% \text{ CL}) \\ \sigma_{\gamma p \xrightarrow{\mathbb{O}} \pi^0 N^*} &< 100.0 \text{ nb} \qquad (99\% \text{ CL}) \;. \end{aligned}$$

5.10 Outlook

5.10.1 Incorporating Data from the 2000 Campaign

The upper limit given in section 5.9 is mainly dominated statistically. The limit can be improved by increasing the luminosity and thus the number of expected events. Due to problems with the FNC preshower detector, the Odderon triggers *S96* and *S97* were implemented in H1 only until the beginning of May 2000. This corresponds to approximately an additional 7 pb^{-1} of integrated luminosity for 2000. In [NIX01], this data will be included in the analysis. Assuming the same conditions, it is possible to make a forecast on the number of events and thus, an extrapolation to the upper limit obtained by the sum of all 1999 and 2000 data:

$$\sigma_{\gamma p \to \pi^0 N^*}^{1999+2000\ data} < 74 \text{ nb}, \tag{5.58}$$

with a confidence of 99%.

5.10.2 New Efficiency of the Electron Tagger

As pointed out in section 5.7, the final numbers for the electron tagger efficiency have not yet been provided [LEV00]. From a second order Taylor series expansion a formula is given that yields a corrected upper limit for the new efficiency of the electron tagger:

$$\sigma_{upper\ limit}^{eTAGcor} = \sigma_{upper\ limit} \cdot (1 - \Delta\epsilon + 2(\Delta\epsilon)^2), \tag{5.59}$$

where $\sigma_{upper\ limit}$ is the upper limit from section 5.9, $\Delta\epsilon$ is the relative variation of the eTAG_{33} efficiency and $\sigma_{upper\ limit}^{eTAGcor}$ is the new corrected value of the upper limit.

5.10.3 Estimate of the η Cross Section

Beside π^0s, η mesons are expected to be produced in the same fashion in the reaction:

$$\gamma p \xrightarrow{\mathbb{O}} N^* \eta, \tag{5.60}$$

with the subsequent decay:

$$\eta \to \gamma\gamma. \tag{5.61}$$

In contrast, the branching ratio of this decay amounts to only 39.3% [PDG00]. Unfortunately, the t-distribution of the exclusive η production in Odderon-photon-fusion has not yet been calculated in the MSV. However, an estimate can be given: Assuming the same distribution for the transverse momentum of the η as for pions (shown for the photon-photon-fusion in [BER99a]), the only difference between the η and the π^0 is the higher mass of the η (m_η = 547.3 MeV [PDG00]).This has an impact on the acceptance of the two photons. Figure 5.19 (a) demonstrates that the acceptance for the detection of both photons in the VLQ vanishes. On the other hand, the acceptance that one photon is detected in the VLQ and the other one in the Spacal rises, an estimate of the acceptance for η mesons is shown in

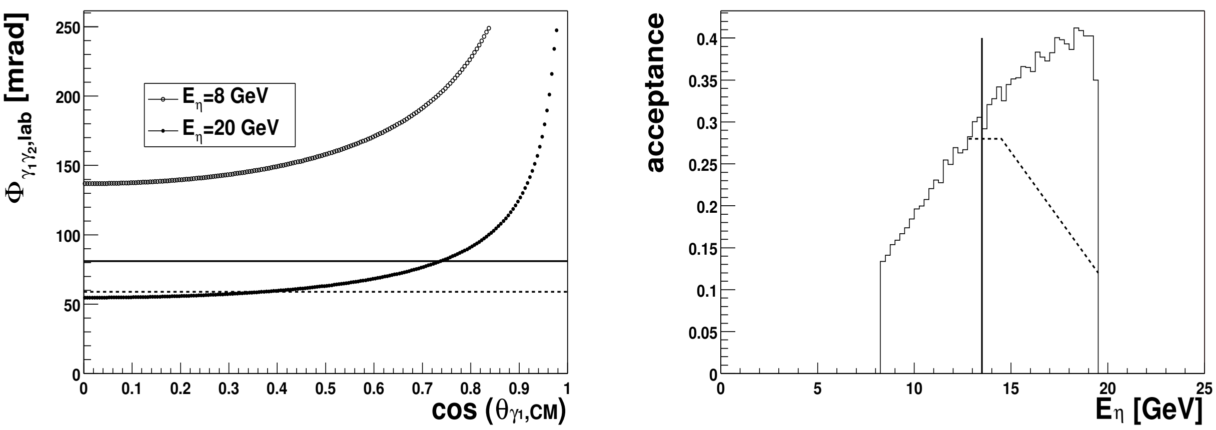

(a) (b)

Figure 5.19: *Plot (a) shows the opening angle $\Phi_{\gamma_1\gamma_2,lab}$ of the two photons from the η decay as a function of the decay angle of the most energetic photon. The acceptance region of the VLQ is defined by the dashed line and $\Phi_{\gamma_1\gamma_2,lab} = 0$ (compare figure 1.20 for pions). The solid line defines the minimum angle for which one photon still hits the Spacal when the other photon hits the VLQ. Plot (b) shows the acceptance – compare figure 5.14 and (5.52) – of $\mathbb{OP}$IUM for the case that at least one cluster is reconstructed. The solid line is related to the energy of pions having a minimum opening angle which is given by the solid line in (a). The region defined by the left part of the curve and the dashed line represents the estimate of the acceptance for η mesons.*

figure 5.19 (b): For energies smaller than 13.5 GeV, one photon always hits the Spacal if the other photon hits the VLQ due to the restricted opening angle (less than 4% of the photons have a larger angle so they cannot be seen in the Spacal). Thus, the acceptance is given by the condition that at least one VLQ cluster with (5.27) is reconstructed and the other generated photon fulfils (5.28) (The reconstruction efficiency for one cluster in the Spacal is approximately 100%). The dashed line in figure 5.19 (b) represents an extrapolation of the acceptance in figure 5.14 (a): with decreasing pion energy, the minimum opening angle, and consequently the acceptance, rises due to the geometric configuration (figure 5.3). Furthermore, the same width (5.49) as for the pion is assumed which results in approximately the same background for *PYTHIA* and *PYTHIA ND*. According to the remaining 5 events in the top plot of figure 5.16 a rough estimate on the upper limit on the cross section can be performed:

$$\sigma_{ep \xrightarrow{\mathbb{O}} e\eta N^*} < 0.82 \text{ nb} \qquad \text{and} \qquad \sigma_{\gamma p \xrightarrow{\mathbb{O}} \eta N^*} < 60 \text{ nb} \qquad (99\% \text{ CL}) \,, \tag{5.62}$$

using the same method – appendix A.3 and A.4 – as for the π^0.

The same arguments as for the η hold also for another pseudoscalar, the η'. It has also a decay mode in two photons with a branching ratio of 2.12% [PDG00]. Yet the mass of that meson is still larger ($m_{\eta'} = 957.8$ MeV [PDG00]) and therefore the extrapolation of the acceptance is more unprecise. Furthermore the acceptance is reduced by roughly a factor of

20 compared to the η due to the different branching ratios. For these reasons no estimate on the upper limit is performed.

Chapter 6

Summary and Conclusion

An analysis of exclusive π^0 photoproduction with the H1 detector at HERA is presented. The goal is the cross section measurement of the process: $\gamma p \to \pi^0 N^*$ in ep scattering.

The kinematical region under investigation is limited to $Q^2 < 0.01$ GeV^2 and $0.3 < y < 0.7$ which implies an average photon-proton centre-of-mass energy of $\langle W \rangle \approx 211$ GeV. The subtrigger *S96* serves as a preselection for the events. This trigger requires the detection of the scattered electron in the electron detector and an energy deposition in the forward neutron calorimeter with a run-dependent trigger threshold. In addition, for the run periods *99-1* and *99-2* one cluster and an energy deposition of more than 5 GeV is required in the VLQ on trigger level 4, respectively. An integrated luminosity of 11.06 pb^{-1} is used for the investigated data of 1999.

The decay mode $\pi^0 \to \gamma\gamma$ was investigated so that the two modules of the VLQ and the Spacal were scanned for two-photon final states whereby the two most significant configurations are "*one photon in the VLQ and one photon in the Spacal*" and "*both photons in the identical VLQ module*". Beside the selection criteria on the fiducial volume and the detectable kinematical ranges of the used detector components, two further cuts on the exclusiveness of the pions are of importance: No detected vertex and a cut on $(E - P_z)_{e'\gamma\gamma}$.

The result can be summarized in three points:

1. Cross section measurement reveals agreement with photoproduction processes as modelled by PYTHIA. The photon-proton cross section in the kinematical domain is

$$\sigma_{\gamma p \to \pi^0 N^*} = 32.0 \pm 16.0 \text{ (stat)} \pm 6.1 \text{ (syst) nb.}$$

2. Odderon induced processes could not be resolved.

3. An upper limit on the MSV cross section was determined to be

$$\begin{aligned} \sigma_{ep \xrightarrow{\mathbb{O}} e\pi^0 N^*} &< 1.36 \text{ nb} \\ \sigma_{\gamma p \xrightarrow{\mathbb{O}} \pi^0 N^*} &< 100.0 \text{ nb} \end{aligned}$$

   on a confidence level of 99%.

In contrast, the predicted value from the MSV is stated to be $\sigma^{MSV}_{\gamma p \xrightarrow{\mathbb{O}} \pi^0 N^*}(W = 211 \text{ GeV}) = 692$ nb and 597 nb (see table 1.1) for the two approaches discussed in section 1.3.3, where the proton is represented either by a free quark-diquark pair or by a small number of resonances, respectively. Assuming no energy scaling – see equation (1.62) – the cross section of the MSV, where the parameters are fixed at an energy of $W = 20$ GeV, is given by $\sigma^{MSV}_{\gamma p \xrightarrow{\mathbb{O}} \pi^0 N^*}(W = 20 \text{ GeV}) = 341$ nb and 294 nb [BER99a], respectively. Even in this conservative case the predicted cross section can be rejected on a 99% confidence level. Thus, the interpretation of the result is that the MSV is not compatible with the presented measurement. It should be noted, however that the theoretical uncertainty of the cross section in the MSV is at least of a factor of 2 at $W = 20$ GeV [BER99a].

The absence of Odderon induced contributions agrees with results of another analysis [BER97]. In that work the processes

$$ep \to e\eta X \qquad \text{and} \qquad ep \to e\eta' X \tag{6.1}$$

in photoproduction are under study, where the pseudoscalars η and η' decay into two photons, respectively (see section 5.10). The used trigger demanded the scattered electron detected in the eTAG$_{33}$ and an energy deposition in the Spacal, yet no requirements were made on the proton final state X. Both decay photons from the respective meson were reconstructed in the Spacal. Neither process in (6.1) yielded a signal, and upper limits were derived:

$$\sigma_{ep \to e\eta N^*} < 171.3 \text{ pb} \qquad (90\% \text{ CL}), \tag{6.2}$$
$$\sigma_{ep \to e\eta' N^*} < 798 \text{ pb} \qquad (90\% \text{ CL}), \tag{6.3}$$

where (6.2) can be compared with (5.62), however the confidence level is different and the proton final state in (5.62) is restricted to excited protons.

Appendix A

Determination of a Confidence Limit

The two most frequently used interval constructions are presented, the classical confidence intervals by Neyman [NEY37] and the Bayesian (as in [HEL83]). The problems connected with these *ansätze* are pointed out and as a conclusion, a third classical model is introduced that avoids such problems. Finally it is shown how the systematic uncertainties are incorporated.

This discussion makes use of a Poisson distribution (Poissonian) of the detected and expected events, but it can also be applied to any other probability density function (pdf).

Let μ be the unknown number of events expected ($\mu = \sigma \cdot \int \mathcal{L}\ \mathrm{d}t \cdot BR \cdot \epsilon$) and b the known number of background events, then the Poissonian probability $P(N|\mu)$ to measure N events is given by:

$$P(N|\mu) = (\mu + b)^N \frac{\exp^{-(\mu+b)}}{N!}. \tag{A.1}$$

A.1 Bayesian intervals

Assuming that a single measurement of the number of events N yields the value N_0, by substitution of this value into expression (A.1) for $P(N|\mu)$, $P(N_0|\mu)$ is obtained which is known as the likelihood function in this case. Using this function, Bayes's theorem predicts the so called posterior pdf $P(\mu|N_0)$, which gives the probability that μ is the true value when N_0 is measured:

$$P(\mu|N_0) = P(N_0|\mu) \cdot \frac{P(\mu)}{P(N_0)}. \tag{A.2}$$

The denominator $P(N_0)$ is a normalisation constant. The numerator $P(\mu)$, the so-called "a priori" pdf, is not known. It could be determined from empirical studies based on specific models or has to be "guessed". Choosing or finding the best-suited pdf $P(\mu)$ is the major disadvantage of the Bayesian approach.

A Bayesian interval $[\mu_1, \mu_2]$ corresponding to a confidence level α $(0 \leq \alpha \leq 1)$[1] can be

[1] $\alpha = 0.6827$ corresponds to the 1σ limit, $\alpha = 0.95$ to the 2σ limit and $\alpha = 0.99$ to the 3σ limit of a Gaussian distribution

constructed from the posterior pdf by requiring:

$$\int_{\mu_1}^{\mu_2} P(\mu|N_0)\ \mathrm{d}\mu = \alpha, \tag{A.3}$$

with the freedom of choice of μ_1 depending on whether an upper limit, lower limit, central interval, etc. is desired.

Typically, a subjective a priori pdf is used covering the "best knowledge" according to previous experiments or theoretical approaches. On the other hand, an objective uniform a priori pdf can be defined, ignoring prior information but also losing the real power of Bayesian inference.

A.2 Classical Confidence Intervals

Neyman's confidence intervals completely avoid the concept of pdf's as functions of μ. Rather, a confidence interval $[\mu_1, \mu_2]$ is an element in a set, which has the property:

$$P(\mu \in [\mu_1, \mu_2]) = \alpha. \tag{A.4}$$

In particular, this means that the intervals contain the fixed unknown μ in a fraction α of a large number of virtually conducted experiments. The most common choice to specify the interval $[\mu_1, \mu_2]$ is by giving an *upper confidence limit*, defined by:

$$\mu_1 = 0 \ \text{ and } \ P(N < N_0|\mu_2) = 1 - \alpha, \tag{A.5}$$

and a *central confidence interval*:

$$P(N > N_0|\mu_1) = P(N < N_0|\mu_2) = \frac{1-\alpha}{2}. \tag{A.6}$$

However, in both cases unphysical empty confidence belts may occur.

A.3 New Intervals from an Ordering Principle based on Likelihood Ratios

A more sophisticated approach avoiding the eventuality of empty confidence belts is given in [COU98]. Here a ratio of likelihoods R:

$$R = \frac{P(N|\mu)}{P(N|\mu_{best})} \tag{A.7}$$

is used as an ordering principle by which those values of N are selected, which are placed in the acceptance interval; μ_{best} is that value of the mean signal μ which maximizes $P(N|\mu)$.

Values of N are added to the acceptance region for a given μ in decreasing order of R, and the corresponding probabilities $P(N|\mu)$ are added, until the sum of $P(N|\mu)$ meets or exceeds the desired confidence level. In [COU98], tables are provided that yield intervals for the number of events observed N_0, background b and the desired confidence level.

A.4 Incorporating the Systematic Uncertainties into the Upper Limit

In this section an outline is given describing how the systematic uncertainty σ_{sys} of the experimental sensitivity is incorporated into the upper limit. The Poissonian distribution does not allow for the quadratic addition of the statistical and the systematical error. In [COU92], an analytic approach is presented that incorporates the systematic uncertainty by an explicit integral over the respective Poissonian pdf weighted by the pdf of the systematic uncertainty, which usually can be considered Gaussian. If the background b that must be subtracted is known, it is more convenient to proceed by a Taylor expansion of the weighted Poissonian pdf around the point found to be the upper limit in the absence of systematic uncertainties. Considering only linear terms, one finds:

$$\mu_{2sys} = \mu_2 + \frac{\mu_2 + b - N_0}{\mu_2 + b} \cdot \mu_2^2 \sigma_{sys}^2 / 2, \tag{A.8}$$

where μ_{2sys} is the new upper limit for the expected number of events.

Bibliography

[ABA94] S. Abatzis et al., Phys. Lett. **B324** (1994) 509 (WA 91 Collaboration).

[ACO91] D. Acosta et al., Nucl. Instr. Meth. **A308** (1991) 481.

[ACO91a] D. Acosta et al., Nucl. Instr. Meth. **A314** (1991) 431.

[AHM93] H1 Collaboration, T. Ahmed et al., Phys. Lett. **B299** (1993) 374.

[AHM95] H1 Collaboration, T. Ahmed et al., Nucl. Phys. **B439** (1995) 471.

[AID95] H1 Collaboration, S. Aid et al., Nucl. Phys. **B470** (1995) 471.

[APP96] R.D. Appuhn et al.,The H1 Spacal Group, Nucl. Instr. Meth. **A382** (1996) 395.

[APP97] R.D. Appuhn et al.,The H1 Spacal Group, Nucl. Instr. Meth. **A386** (1996) 397.

[BAU78] T. H. Bauer et al., Rev. Mod. Phys. **50** (1978) 261.

[BEN91] S. Bentvelsen, J. Engelen, P. Kooijman, Reconstruction of (x, Q^2) and extraction of structure functions in neutral current scattering at HERA, Proceedings of the workshop: Physics at HERA (1991) Vol.1, 23.

[BER97] T. Berndt, "Exklusive Produktion der Mesonen η, η' und ω in Multi-Photon-Endzuständen bei HERA", Diploma Thesis, University of Heidelberg (1997).

[BER99] E. R. Berger, "Diffraktive Hochenergiereaktionen in nicht-störungstheoretischer QCD", Dissertation, University of Heidelberg (1999).

[BER99a] E. R. Berger et al., Eur.Phys.J. **C9** (1999) 491.

[BER99b] E. R. Berger, Nucl. Phys. Proc. Suppl. **74** (1999) 96.

[BER01] T. Berndt, Dissertation in preparation (prospective 2001).

[BET30] H. A. Bethe, Ann. Physik **5** (1930) 325.

[BLO33] F. Bloch, Ann. Physik **16** (1933) 285.

[BRE85] A. Breakstone et al., Phys. Rev. Lett. **54** (1985) 2180.

[BRU96] C. Brune, "Bestimmung der Protonstrukturfunktion $F_2(x_{bj}, Q^2)$", dissertation, University of Heidelberg, (1996).

[BUN00] A. Buniatian, Private communication (2000).

[COL77] P.D.P. Collins, "An Introduction to Regge Theory and High Energy Physics", Cambridge University Press, Cambridge (1977).

[COU92] R. D. Cousins and V. L. Highland, Nucl. Instr. Meth. **A320** (1992) 331.

[COU98] R. D. Cousins and G. J. Feldman, Phys. Rev. **D57** (1998) 3873.

[CUB01] C. Cube, Diploma Thesis in preparation (prospective 2001).

[CUD90] J. Cudell, Nucl.Phys. **B336** (1990) 1.

[DER92] ZEUS Collaboration, M. Derrick et al., Phys. Lett. **B293** (1992) 465.

[DON84] A. Donnachie and P.V. Landshoff, Nucl. Phys. **B231** (1984) 189.

[DON89] A. Donnachie and P.V. Landshoff, Nucl. Phys. **B311** (1989) 509.

[DON91] A. Donnachie and P.V. Landshoff, Nucl. Phys. **B348** (1991) 297.

[DON92] A. Donnachie and P.V. Landshoff, Phys. Lett. **B296** (1992) 227.

[DOS87] H. G. Dosch, Phys. Lett. **B190** (1987) 177. H. G. Dosch and Yu. A. Simonov, Phys Lett. **B205** (1988) 339. Yu. A. Simonov, Nucl. Phys. **B307** (1988) 512.

[DOS94] H. G. Dosch, E. Ferreira, A. Krämer, Phys. Rev. **D50** (1994) 1992.

[DOS00] H. G. Dosch, Private communication (2000).

[FRI93] S. Frixione, Phys. Lett. **B319** (1993) 339.

[FRI00] C. Friberg and T. Sjöstrand, preprint, hep-ph/0007314.

[GEA93] GEANT: Detector description and Simulation Tool, CERN Program Library Long Writeup W5013.

[GIN74] V. M. Budnev, I. F. Ginzburg, G. V. Meledin and V. G. Serbo, Phys. Rept. **15** (1974) 181.

[GRO97] J. Grosse-Knetter, "Measurement of Elastic ω Photoproduction at HERA", dissertation, University of Hamburg (1997), Internal Report F35D-97-02.

[H1D96] H1 Collaboration, "'The H1 Detector at HERA"', DESY internal report H1-96-01 (1996).

[H1D96] H1 Collaboration, "Technical Proposal to Build a Special Spectrometer Covering Very Small Momentum Transfers"' (1996).

[H1D97] H1 Collaboration, I. Abt et al., Nucl. Instr. Meth. **A386** (1997) 310 & 348.

[H1D99] H1 Collaboration, Eur.Phys.J. **C6** (1999) 587.

[H1I89] J. Meyer, "Guide to Simulation Program H1SIM", H1 internal note, H1 SW 03-11/89.

[HAL84] F. Halzen, A.D Martin, "Quarks & Leptons: An Introductory Course in Modern Particle Physics", Wiley-publishing, New York (1984).

[HAN63] L. N. Hand, Phys. Rev. **129** (1963) 1834.

[HEL83] O. Helene, Nucl. Instr. Meth. **212** (1983) 319.

[HER81] HERA, "'A Proposal for a large Electron-Proton Colliding Beam Facility at DESY"' (1981).

[ING97] G. Ingelman, A. Edin and J. Rathsman, Comp. Phys. Comm. **101** (1997) 108, for the program code and manual see
`http://www3.tsl.uu.se/thep/lepto/` .

[KIL97] W. Kilian, O. Nachtmann, Eur. Phys. J. **C5** (1997) 317.

[KLU00] T. Kluge, "Untersuchung des QED-Bremsstrahlungprozesses bei kleinen Impulsüberträgen mit dem H1-Detektor bei HERA", Diploma Thesis, University of Aachen (2000).

[KOR00] Simulation routine $\mathbb{O}I\!P$IUM written by W. Kornelis in Heidelberg (2000).

[LAN87] P. V. Landshoff, O. Nachtmann, Z. Phys. **C35** (1987) 405.

[LEV95] H1PHAN routine QPETAC written by S. Levonian (1995).

[LEV00] S. Levonian, Private communication (2000).

[LIS97] B. List, Ph.D. Thesis, University of Hamburg, (1997); B. List (for the H1 Collaboration), Proceedings of the 5th International Workshop on Deep Inelastic Scattering and QCD, Chicago 1997, (1997) 520.

[LIS99] B. List and A. Mastroberardino, Proc. on the Workshop on Monte Carlo Generators for HERA Physics, (1999).

[LUK73] L. Lukaszuk, B. Nicolescu, Lett. Nuov. Cim. **8** (1973) 405.

[MET98] F. Metlica, "Produktion von Neutronen in Vorwärtsrichtung durch e - p Kollision bei HERA",dissertation, University of Heidelberg (1998).

[MEY00] P. O. Meyer, "Messung der Strukturfunktion F_2 bei kleinen Bjorken-x und kleinen Impulsuebertraegen mit dem VLQ-Spektrometer des H1-Detektors", dissertation, University of Aachen (2000).

[NAC91] O. Nachtmann, Ann. Phys. **209** (1991) 436.

[NEY37] J. Neyman, Philos. Trans. R. Soc. London **A236** (1937) 333.

[NIC96] T. Nicholls et al.,The H1 Spacal Group, Nucl. Instr. Meth. **A374** (1996) 149.

[NIE00] O. Niedermaier, "Eine absolute Energieeichung für ein Elektronenspektrometer", Staatsexamensarbeit, University of Heidelberg (2000).

[NIX00] O. Nix, Private communication (2000).

[NIX01] O. Nix, Dissertation in preparation (prospective 2001).

[NUN96] T. Nunnemann, "Aufbau und Test eines Kleinwinkel-Neutronen-Kalorimeters für das Experiment H1",Diploma Thesis, University of Heidelberg (1996).

[NUN99] T. Nunnemann, "Measurement of Leading Neutron Production in Deep-Inelastic *ep* Scattering at HERA",dissertation, University of Heidelberg (1999).

[PDG00] The PDG, The European Physical Journal C, (2000) 54.

[POV97] B. Povh et al., "Teilchen und Kerne",Springer-Verlag,Berlin (1997).

[PRE92] W. Press, S. Teukolsky, W. Vetterling and B. Flannery, "Numerical Recipies", 2nd ed.,Cambridge Univ. Press, Cambridge, UK (1992).

[RUE98] M. Rueter, H. G. Dosch, O. Nachtmann, Phys. Rev. **D59** (1998).

[SCH93] G.A. Schuler, T. Sjöstrand, Nucl. Phys. **B407** (1993) 539.

[SCH93a] G.A. Schuler, T. Sjöstrand, Phys. Lett. **B300** (1993) 169.

[SED00] K. Sedlák, H1 internal note, H1-03/00-581.

[SJO94] T. Sjöstrand, Computer Physics Commun. **82** (1994) 74.

[SJO00] T. Sjöstrand, Private communication (2000).

[STE98] A. Stellberger, "Entwicklung und Bau eines kompakten elektromagnetischen Kalorimeters", dissertation, University of Heidelberg (1998).

[SWA00] M. Swart, "Mass Spectroscopy of Neutral Mesons in the Photon Hemisphere at HERA", dissertation, University of Heidelberg (2000).

[ZEU98] ZEUS Collaboration, Eur.Phys.J. **C2** (1998) 247.

Acknowledgements

This page is devoted to all who supported my research and who contributed to the writing of this Diploma thesis. Especially many thanks to Prof. Karlheinz Meier for giving me the opportunity to participate in his H1 working group and for his subtle advice whenever problems have arisen. I would also like to thank Prof. Hans-Günter Dosch for being so kind to take over the burden of correction. I am indebted to Dr. Jürgen Stiewe for steady proofreading and inspiring discussions about art, history, ... and of course physics. Tommy Berndt, master of the fancy tools, I owe "humble" thanks for the assistance in all open questions. A big thank-you to Dr. Rick Cavanaugh for the way *voir la vie en rose* and to Dr. Claus Beier, both of whom I owe a debt of gratitude for enduring the correction with so much patience and for the amusing discussions about the English orthography. Furthermore, I would like to express my appreciation to Oliver Nix for his challenging critical viewpoint (*der Geist, der stets verneint*). Many thanks to my two office-mates Kambiz Mahboubi for sharing with me some long evenings (and even longer) of writing this work and our Frenchman, Guillaume Leibenguth, for tickling my palate as often as possible and for *savoir vivre comme dieu en France...*

Sincere thanks are given to all who contributed to my pleasurable last year: Christoph von Cube, Henning Flächer, Wouter Kornelis, Oliver Niedermeier, Dr. Martin Swart, in particular Dr. Selvam Dhamotharan for delightful outdoor activities, outstanding group dynamics and remembering me of the meaning of *serious boozing*, not to mention the *Kaffeerunde*, who understood to create the friendly atmosphere.

I am deeply grateful to my aunt Elisabeth Schmid for the financial support during my study. I would like to acknowledge my parents for their belief in me during my entire life and for being there whenever it was necessary. I would also like to thank my brother, my sister and my great friends and to apologize to everyone whom I have neglected these past months.

Finally, once more thank you, Simone, for everything.